industriales
etsii

Escuela Técnica Superior de Ingeniería Industrial

TECHNICAL UNIVERSITY OF CARTAGENA

Faculty of Industrial Engineering

Correlation of Results Between Test Measurements, Analytical Calculations and Virtual Simulations of a PMSM

THESIS DEGREE

MECHANICAL ENGINEERING DEGREE

Author:	**José González Cabrero**
Director:	Andrés Cabrera Lozoya
Codirector:	Daniel Carreres Prieto
External Codirector:	Jintin Tran

Cartagena, 10 de mayo de 2021

Universidad Politécnica de Cartagena

Correlation of Results Between Test Measurements, Analytical Calculations and Virtual Simulations of a PMSM

Abstract

In the course of this thesis, simulations under utilization of the FEM software COMSOL, test measurements and analytical calculations with the use of the MATLAB software of a high pole Permanent Magnet Synchronous Motor (PMSM) for cryogenic applications were carried out. The objective is the correlation of results between the measurements of the motor test, the analytical calculations, and the virtual simulations. The development of every of these three works is carefully analyzed separately. On this basis, this thesis can be divided into the comparison of electromagnetic results, and the comparison of thermal results. Some research studies are also presented like the impact of the machine magnets materials as well as the operation temperature in the output torque and power, this is examined by comparison of two different types of magnets (NdFeB) and (Sm2Co17) for different ambient temperatures. As a result, the most suitable magnet material is obtained. Another research study carried out is the extensive compilation of motor thermal simulation data, for stationary and transitionary regimes, obtaining the temperature distribution of each of the motor components for different periods of time. The thesis concludes by presenting a final scheme of the results, iteratively correlated throughout the course of this thesis.

Table of contents

1 Introduction 1
1.1 MPE projects 1
1.2 Thesis background 2
1.3 Thesis structure 3
2 Motor characteristics 5
2.1 Motor design 5
2.2 Material properties 6
2.3 Motor dimensions 8
2.4 Magnet materials 10
3 Theoretical fundamentals 11
3.1 Synchronous motors 11
3.2 Difference between D.C excited sync. motor and PMSM. Back EMF 13
3.3 Difference between IPM and SPM sync. motor 13
3.4 Effect of loads on a synchronous motor 14
3.4.1 Phasor diagram of a synchronous motor under loads 15
3.4.2 Phasor diagram of the prototype PMSM under loads 16
3.5 Parameters calculation of the motor under loads 17
3.5.1 Parameters calculation of a typical cylindrical synchronous motor 17
3.5.2 Parameters calculation of the prototype PMSM 20
3.5.3 Inconsistent results problem 22
4 Analytical calculations 23
4.1 Electromagnetic torque analytical calculation 23
4.1.1 Electromagnetic circuit and theoretical explanation 23
4.1.2 Electromagnetic torque results 26
4.1.3 Research study in permanent magnets and induced torque 26
4.1.4 Research study results 27
4.1.4.1 Study 1: Maximum torque depending on ambient temperature for NdFeB magnets 27
4.1.4.2 Study 2: Maximum torque depending on magnet material at normal temperature conditions (293.15 K) 30
4.2 Motor losses analytical calculation 31
4.2.1 Results motor losses 33
4.3 Thermal analytical calculation 34
4.3.1 Basic concepts of heat transfer-mechanisms 34
4.3.1.1 Conduction heat transfer. Cylinder 34
4.3.1.2 Convection heat transfer. Cylinder 36
4.3.1.3 Radiation heat transfer. Cylinder 36
4.3.2 Motor analysis at normal conditions 37
4.3.2.1 Assumptions 38
4.3.2.2 Heat transfer model 38
4.3.2.3 Stator analysis 40
4.3.2.3.1 Stator convection 40

4.3.2.3.2 Stator conduction 43
4.3.2.4 Winding analysis 43
4.3.2.5 Air gap heat transfer analysis 44
4.3.2.5.1 Air gap convection 44
4.3.2.5.2 Air gap conduction 45
4.3.2.6 Magnet analysis 46
4.3.2.7 Rotor shaft analysis 46
4.3.2.8 Analytical results. Temperature distribution at normal conditions 47
4.3.3 Motor analysis at cryogenic conditions 48
4.3.3.1 Analytical results. Temperature distribution at cryogenic conditions 49
4.4 Thermal contact resistance. Theory 50
5 COMSOL Multiphysics® software simulations 52
5.1 Electromagnetic simulations 52
5.1.1 Modelling PMSM dynamics in COMSOL Multiphysics 52
5.1.2 Electromagnetic results 53
5.2 Thermal simulations 58
5.2.1 Stationary thermal simulations 59
5.2.1.1 Temperature distribution at normal conditions 59
5.2.1.2 Temperature distribution at cryogenic conditions with air gap 60
5.2.1.3 Temperature distribution at cryogenic conditions with vacuum gap 61
5.2.2 Transitionary thermal simulations 63
5.2.2.1 Temperature distribution at normal conditions 63
5.2.2.1.1 Sector 63
5.2.2.1.2 Winding 65
5.2.2.1.3 Magnets 67
5.2.2.1.4 Rotor 68
5.2.2.2 Temperature distribution at cryogenic conditions with vacuum gap 70
5.2.2.2.1 Sector 70
5.2.2.2.2 Winding 72
5.2.2.2.3 Magnets 73
5.2.2.2.4 Rotor 75
5.2.3 Stationary thermal simulations. Whole model 77
5.3 Motor losses 78
6 Motor test 81
6.1 Motor test setup 81
6.2 Test measurement plan and results 84
7 Correlation of results 90
7.1 Electromagnetic results correlation 90
7.2 Thermal results correlation 91
7.2.1 Thermal results correlation at normal ambient conditions 91

7.2.2 Thermal results correlation at cryogenic ambient conditions 92
7.3 Motor losses results correlation 94
8 Conclusion and outlook 95
Bibliography i
List of figures iii
List of tables x
List of graphics xi
APPENDIX. Matlab codes. Calculations xii

1 Introduction

In recent decades, electric motors have increasingly become an everyday item for the entire population due to its reachable high efficiency and low work susceptibility. They come in a wide variety of applications moving from generally industry use, to finding them in homes, in addition to remote research applications on land, in air, in water, and also in space, each with its own specific features depending on the operation requirements. The motors are used in many areas such as mobile robotics, industrial robotic arms, elevators, drills, electric cars, drones or in other less demanding applications from the point of view of automatic control such as pumps, conveyor belts, among others. Worldwide, energy consumption in the industry due to the use of electrical machines is estimated to be within the range of 50 to 80% of the total. However, the operating conditions are increasingly demanding, therefore, it is necessary to develop new proposals for operation and control. (Tapia Olvera, s.f.)

Some rare application fields, such as the operation in a cryogenic environment are little researched (Karnehm, 2017) . This is due to the fact that there are barely any commercially available machines in this field.

1.1 MPE Projects

This undergraduate thesis has been completed at the Max-Planck Institute for Extraterrestrial Physics (MPE), Munich. This institute is part of the Max-Planck Society, which is one of the leading associations for basic research in Germany. This institution publishes around 15,000 publications every year in internationally renowned scientific journals and has held 18 Nobel prizes since it was founded in 1948. Currently, a total of 83 different departments that make up the Max Planck society work in research in the physical sciences, natural sciences, social sciences and humanities. In 1991 the Max Planck Institute for Physics and Astrophysics split up into three different departments, one of them was The MPE with the aim of researching in the areas of physics and chemistry of stars, interstellar matter, exotic objects such as neutron stars and holes blacks and near and far galaxies and cosmology. The MPE develops several projects, such as the Advanced Telescope for High-Energy Astrophysics (ATHENA) project, or the Enhanced Resolution Imager and Spectrograph (ERIS) project, a next-generation instrument for the Very Large Telescope (VLT) in Chile (Max-Planck-Gesellschaft, 2020). The background of this thesis will be briefly explained below, then the structure of this work is presented. This thesis is based on another project of the MPE, namely GRAVITY. According to (Max-Planck-Gesellschaft, 2020) “GRAVITY is the second-generation VLTI instrument for precision narrow-angle astrometry and interferometric imaging. It will bring the most advanced vision to the VLT: with its fiber-fed integrated optics, wave front sensors, fringe tracker, beam stabilization, and a novel metrology concept, GRAVITY will push the sensitivity and accuracy far beyond what is offered today. Providing precision astrometry of ten microseconds, and imaging with four milliarcsecond resolution, GRAVITY will revolutionize dynamical measurements of celestial objects: it will probe physics close to the event horizon of the Galactic Center black hole, unambiguously detect and measure the mass of black holes in massive star clusters throughout the Milky Way, uncover the details of mass –creation and jets in young stellar objects and active galactic nuclei, and probe the motion of binary stars, exoplanets and young stellar disks”. For this purpose, the telescope is cooled to the liquid nitrogen

temperature, which is 77 K, and Ultra High Vacuum (UHV) is aspirated, which is equivalent to an air pressure of 10^{-8} bar.

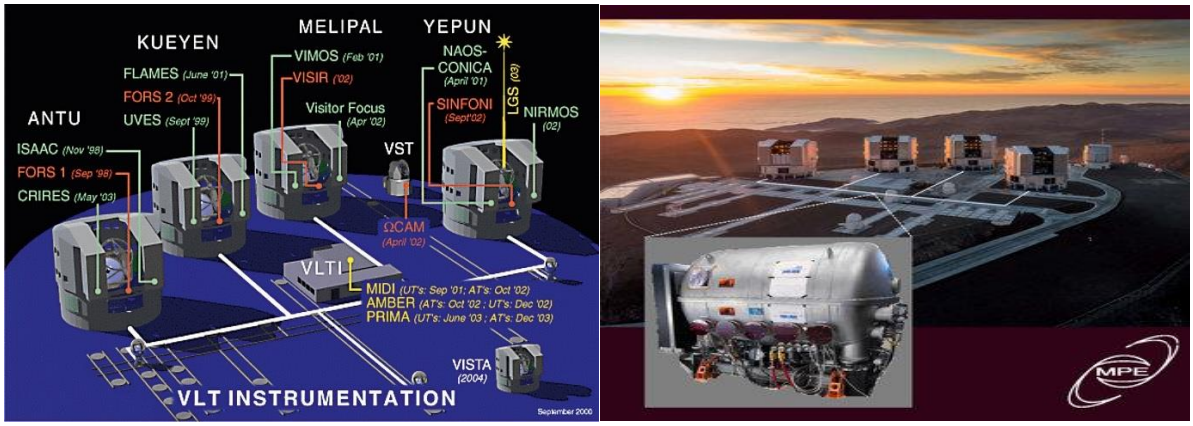

Figure 1. The VLT offers also the possibility of combining coherently the light from the four UTs to work as an interferometer, the Very Large Telescope Interferometer (VLTI)

1.2 Thesis Background

This thesis is based on the development of a permanent magnet synchronous electrical motor that could potentially operate in the GRAVITY instrument. A few students have participated a long its development process. The main special feature of the motor is the ability to operate in conditions of cryogenic temperature and Ultra High Vacuum (UHV) pressure. The motor was first pre-designed and calculated in the thesis (Karnehm, 2017), and was based on the following points:

1. A comparison between different types of electrical motors through a series of requirements that had to be solved in the best possible way, including their operation in extremely low temperature conditions, to finally opt for the development of a PMSM.
2. A study of the most suitable materials for their use in these cryogenic conditions.
3. The calculation and pre-designed of the motor was carried out, obtaining its dimensioning characteristics, as well as some parameters such as the nominal torque or the magnetic flux density in the air gap of the motor that could be produced.
4. A basic study of the motor control system.

The pre-design and first nominal parameters calculation were made in (Karnehm, 2017). The thesis (Grabichler, 2018) was focused on the development of the control of the motor. In the research internship report (Bratke, 2018), the first electromagnetic and thermal simulations of the initial motor model were carried out through the Multiphysics simulation software COMSOL, which will be briefly explained throughout the development of this thesis. In (Schoch, 2019), the mechanical design and construction of the first prototype was made, taking as a starting point the dimensions calculated in (Karnehm, 2017). The stator part, the rotor shaft, the permanent magnets were designed under SolidWorks CAD design software, as well as the choice, and calculation of bearings for this first prototype.

1.3 Thesis Structure

Almost every chapter of this thesis can be separated in the electromagnetic analysis, motor losses analysis and thermal analysis, therefore the thesis can be divided in three main parts.

Part one: It deals primarily with a triangular verification of the results of some electromagnetic parameters, by comparing the motor test results with the analytical calculations and with the electromagnetic simulations. On the one hand, the results of the motor test measurements in the test bench were obtained. For this purpose, a measurement plan was designed for an orderly data collection of the parameters. The analytical electromagnetic calculations were performed by implementing the equations that describe the motor behaviour in the MATLAB software. And finally, the electromagnetic simulations were computed through the COMSOL simulation software. The 3D motor and 2D motor simulations were converged, changing some of the motor parameters to redesign the old simplified model and reshape it to the last prototype.
Finally, a triangular verification of the results of the electromagnetic parameters obtained through these three methods was carried out. To make the comparison it was decided which parameters would be suitable to compare, and the electromagnetic torque was chosen, due to its crucial importance in the description of the motor behaviour. Besides, this first part consists on some studies carried out with the objective of achieving a better optimization of the motor such as the analytical comparison of the electromagnetic torque obtained for different operating temperatures, and for different permanent magnet materials.

Part two: In addition to the comparison of the torque taken by the three described methods; the eddy current losses, the hysteresis losses and the Copper losses of the motor were obtained and compared by simulation and by analytical results calculated through the implementation of the corresponding formulas in the MATLAB code, which will be attach in the Appendix 1 of this thesis.

Part three: It is based on the thermal analysis of the motor, for normal ambient conditions (293.15 K, 1 atm) and cryogenic conditions (77 K, vacuum pressure). For this, a theoretical analysis of the heat transfer as well as the analytical calculations of the temperature distribution on the motor surfaces due to the heat transfer at steady state was performed. The heat transfer equations have been implemented in the MATLAB code, as has also been done in the electromagnetic calculations. As it will be explained in the corresponding section, the motor losses calculated to be compared with those obtained by simulation, will be used as heat dissipated by a particular heat source of the motor (winding), in order to calculate the temperature distribution. In this section these temperatures were calculated under two different ambient conditions:

1. First, for normal conditions of pressure and temperature (293.15 K, 1 atm), where the heat transfer by convection is basically the only produced, neglecting the radiation heat transfer.
2. Second, under cryogenic temperature conditions with vacuum pressure (77 K, 10^{-8}atm), thus only the radiation heat transfer was calculated under these extreme conditions.

Besides, and as a verification method, thermal simulations have been carried out through COMSOL Multiphysics software. These simulations were realised on the basis of those already developed in the internship Christian's report, however the variation of some dimensions, materials, and thermal parameters such as convection coefficients were changed in order to adjust in the most

accurate way the simulation with the characteristics of the last prototype designed. As in the section of the thermal analytical analysis of the motor, simulations have been computed at normal temperature and pressure conditions as well as at cryogenic conditions, where only radiation heat transfer takes place. In addition, a new thermal simulation through the design of the complete motor using SolidWorks was done in order to verify the simulation results of the symmetric sector design.

Finally, as in the first part of this thesis, the results obtained by the analytical thermal analysis, and the results through thermal simulations, have been compared as a verification that the two methods have been developed properly, and to calculate the grade of correlation between them. All the steps carried out in the simulations; the description of the command tree, interfaces used, material selection, etc, will not be explained, it can be seen in (Bratke, 2018). The simulations developed in this thesis, both electromagnetic and thermal have been developed on the basis of the model in (Bratke, 2018).

2 Motor characteristics

2.1 Motor design

The following simplified model of the motor was designed by the author of this thesis using CAD SolidWorks software to perform the thermal simulations of the complete motor model as will be seen in the simulations section of this thesis, although it is not the real model designed by (Schoch, 2019) this model is sufficient to check through these images the different components that make up the motor.

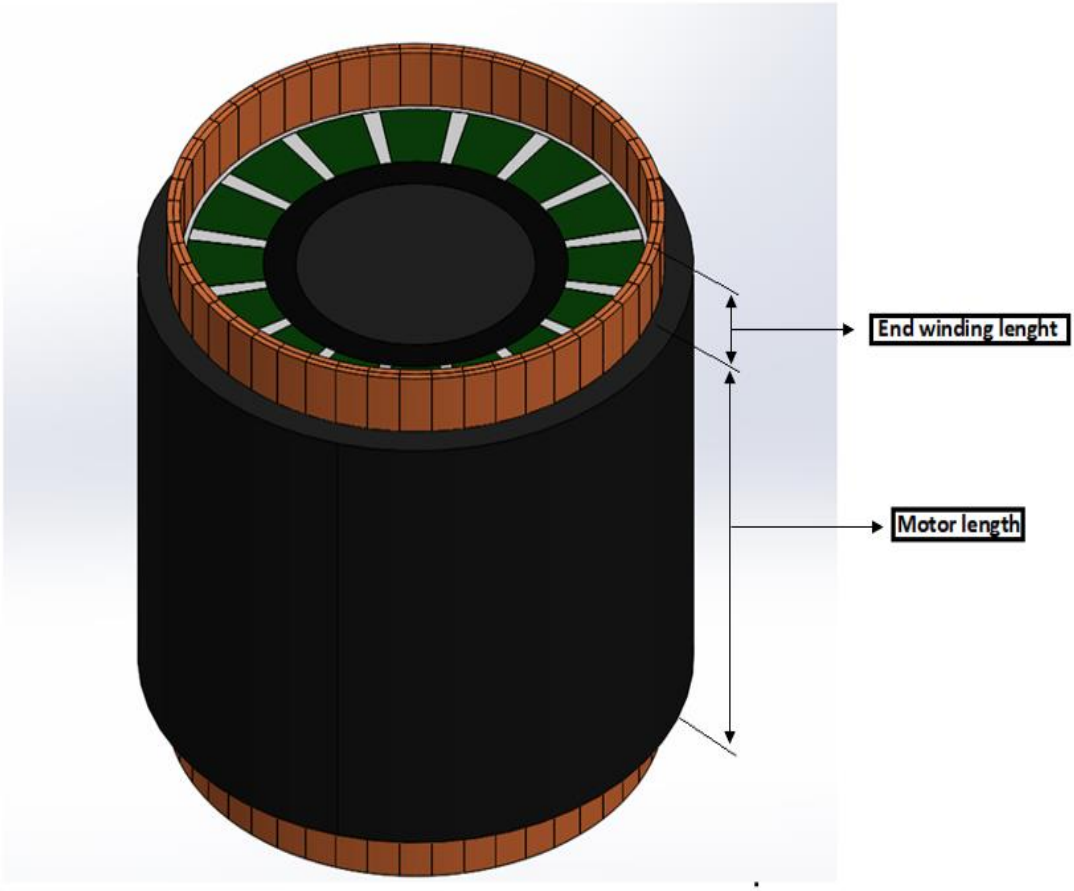

Figure 2. CAD model PMSM

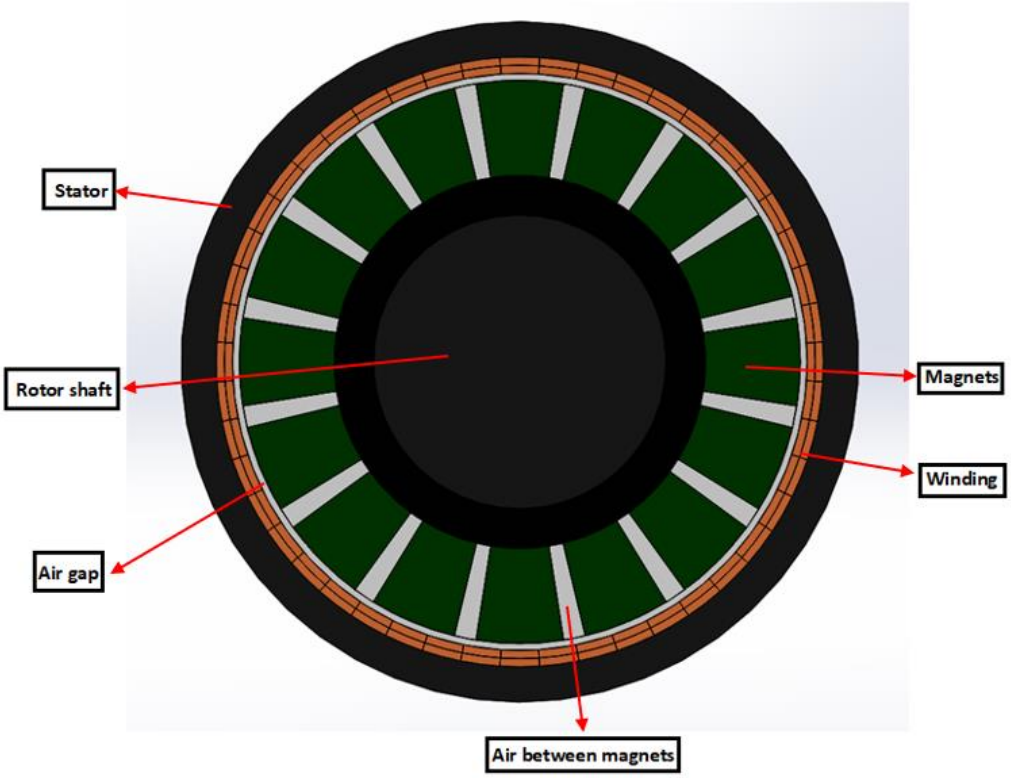

Figure 3. CAD model PMSM with components

2.2 Material Properties

Based on the characteristics of the materials in (Bratke, 2018) this table has been made, extending the number of parameters of the previous table as well as organising them according to the type of material characteristic. These parameters are necessary for the simulations and analytical calculations of the thesis. They have been obtained from (Sintered Neodymium-Iron-Boron Magnets), (Samarium Cobalt Magnets, SmCo Magnets Datasheet), (Magnetic properties YXG32), (Properties of air at 1 atm), (Vacuumschmelze. Cobalt Iron properties)

Table 2.1: Material properties

Material	Usage	Property		Value
Vacoflux 50	Stator and Rotor Shaft	Magnetic	Remnant flux density	B_r =1.6 T
			Saturation flux density	2.35 T
			Magnetic relative permeability	μ_{max}=8000
			Thermal conductivity(25ºC)	$K = 30\ \frac{W}{m\,k}$

		Thermal	**Density**	$\rho = 8.12 \frac{g}{cm^3}$
			Coefficient of linear expansion (20-200 ºC)	$\alpha = 9.4e^{-6} \frac{1}{K}$
NdFeB N45SH	**Magnets**	**Thermal**	**Thermal conductivity (20ºC)**	$K = 7.6 \frac{W}{m\,k}$
			Density	$\rho = 7.5 \frac{g}{cm^3}$
			Heat capacity(20º)	$C_p = 460 \frac{J}{kg\,K}$
			Coefficient of thermal expansion parallel to magnetization direction(20-100ºC)	$C = 7.5 \frac{10^{-6}}{K}$
			Coefficient of thermal expansion perpendicular to magnetization direction(20-100ºC)	$C = -0.1 \frac{10^{-6}}{K}$
		Magnetic and Electrical	**Magnetic relative permeability**	$\mu_{rm} = \frac{B_r}{\mu_0 H_{cB}}$
			Electrical resistivity	ρ = 180 μΩ cm
			Electrical conductivity	$\sigma = \frac{1}{\rho}$
			Remnant flux density (100ºC)	$B_r = 1.23$ T
			Coercivity (100ºC)	$H_{cB} = 850 \frac{KA}{m}$
			Remnant flux density (20ºC)	$B_r = 1.35$ T
			Coercivity (20ºC)	$H_{cB} = 1015 \frac{KA}{m}$
			Remnant flux density (-40ºC)	$B_r = 1.45$ T
			Coercivity (-40ºC)	$H_{cB} = 1115 \frac{KA}{m}$
			Remnant flux density (-196.15ºC)	$B_r = 1.58$ T
			Coercivity (-196.15ºC)	$H_{cB} = 1230 \frac{KA}{m}$

			Sm2Co17 Remnant flux density (20ºC)	B_r =1.1 T
			Sm2Co17 Coercivity (20ºC)	$H_{cB} = 812 \frac{KA}{m}$
Copper	**Winding**	**Thermal and Magnetic**	**Winding diameter**	D=0.5 mm
			Thermal conductivity(20ºC)	$K = 400 \frac{W}{m\,k}$
			Electrical conductivity(20ºC)	$\sigma = 5.96e^{7} \frac{S}{m}$
Air	**Air Gap and surrounding**	**Thermal and Fluid**	**Thermal conductivity(20ºC)**	$K = 0.02514 \frac{W}{m\,k}$
			Coefficient of thermal expansion(20ºC)	$\mathrm{B} = 3.43e^{-3} \frac{1}{K}$
			Kinematic viscosity(20ºC)	$\mathrm{v} = 1.516e^{-5} \frac{m^2}{s}$
			Prandtl number(20ºC)	Pr=0.7309
			Dynamic viscosity(20ºC)	$\mu = 1.825e^{-5} \frac{Kg}{m\,s}$

2.3 Dimensions of the motor

For the motor design, the dimensions were obtained from (Karnehm, 2017) and were barely modified in the thesis (Schoch, 2019) with its respective general tolerances according to DIN ISO 2768-mK. They are written down in Table 2.2 and illustrated in figure 4.

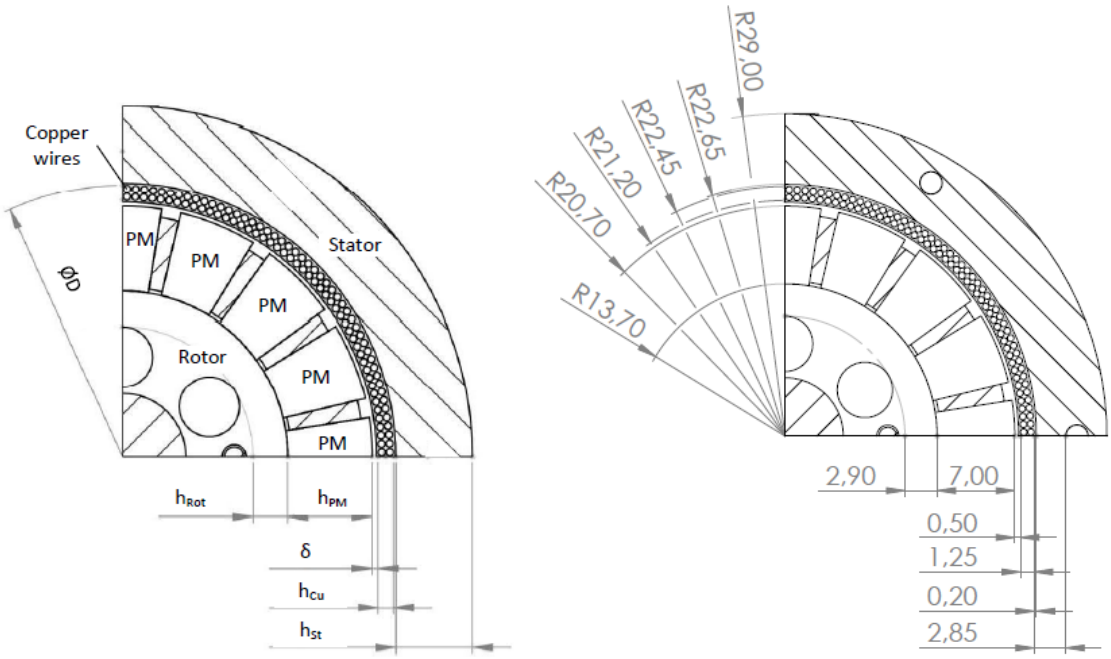

Figure 4. Dimension values of the motor components (Schoch, 2019)

Table 2.2: Dimension values of motor components

Dimension (mm)	Symbol	First model	Current prototype
Inner bore diameter of Stator	D	44.8	45.3±0.05
Min. height of the stator	h_{st}	2.6	6.35±0.1
Air gap	δ	0.5	0.283 ±0.83
Outer diameter of the rotor	D_{PM}	41.4	41.4±0.05
Length of magnets	l	37	37±0.2
Min. height of the rotor	h_{Rot}	2.9	2.9±0.1
Width of the copper wires	h_{Cu}	1.2	1.1±0.1

The dimensions of the motor for all the electromagnetic and thermal simulations as well as the for the calculations in MATLAB were modified from the first model to the current prototype designed in the thesis (Schoch, 2019).

2.4 Magnet materials

It is important to know which are the magnetic materials commonly used in applications of permanent magnet electric motors, it should be noted that the choice of the materials was already made by previous students throughout the development of their theses such as (Karnehm, 2017) or (Schoch, 2019), and the final option was the NdFeB magnet. However, in the chapter of electromagnetic analytical calculations a research study will be realized to verify that the chosen material was the most suitable. So, it is of interest to start describing what are their main characteristics, based on (KWON, 2013):

There are two types of permanent magnet materials of interest for rotating machines (Samarium-Cobalt Sm2Co17 and Neodymium-Iron NdFeB).

Samarium cobalt alloys (Sm2Co17) have a composition of 2 atoms of rare-earth samarium, and 17 atoms of transition metals (TM). The TM content is rich in cobalt, but contains other elements such as iron and copper. The use of large quantities of cobalt make these magnets very expensive. The major advantage of Sm2Co17 is its good temperature stability with maximum use temperatures between 250 and 550 °C. Remnant flux densities (Br) of 0.9-1.15 T can be achieved.

A neodymium magnet (NdFeB) is made from an alloy of neodymium, iron, and boron to form the $Nd_2Fe_{14}B$. There are two main neodymium magnet manufacturing processes, which lead to completely different magnetic properties: The sintered magnet and the bonded magnet process.

Sintered Neo magnets are prepared by pulverizing an ingot precursor, sintering the magnetically aligned powder into dense blocks which are then heat treated, cut to shape, and magnetized. Very high values of remnant flux density can be reached ranging from 1.0-1.4 Tesla. This type of magnet is the strongest type commonly available.

Bonded Neo magnets are prepared by melt spinning a thin ribbon of the Nd-Fe-B alloy. This ribbon is then pulverized into particles, mixed with a polymer and compressed into bonded magnets. Bonded magnets offer less flux than sintered magnets but can be formed into shaped parts and do not suffer significant eddy current losses. These magnets achieve 0.6-0.7 tesla values of remnant flux density (Br).

In the 4.1.3 chapter, a small research study will be made, comparing the Sm2Co17 and the NdFeB magnets regarding their capacity to obtain higher maximum output torques for different temperature ambient conditions.

3 Theoretical fundamentals

This chapter provides a theoretical explanation of synchronous motors. The electrical circuit, the phasor diagram, and the calculation of the parameters that describe them have been explained on the basis that the load on the motor is variant. Furthermore, the same has been done focusing the study on the specific case of PMSM.
However, there is something that should be pointed out, the analytical calculation of the following parameters has not been used to correlate results with simulations and test measurements, since the results obtained were not consistent, at the end of this second chapter there is a brief explanation of this problem and the proposed solution.

3.1 Synchronous motors

A synchronous machine is an alternating current machine whose speed under steady state conditions is proportional to the frequency of the current in its armature. The magnetic field created by the alternating armature currents rotates at the same speed as that created by the field current in the rotor (which rotates at synchronous speed), and a stationary torque is produced. The synchronous speed is described as:

$$n_s = \frac{120\,f}{p} \tag{3.1}$$

Where $n_s(rpm)$ is the rotational synchronous speed, $f(Hz)$ is the applied electrical frequency and p is the number of poles.

A synchronous motor is not self-starting. The rotor poles are subjected to attractions and repulsions, in a short period of time, by the stator poles, but the rotor fails to rotate, then it will vibrate. But if we take the rotor to the speed of synchronism, turning it with an auxiliary motor, when facing opposite sign poles, a magnetic hook can be established that forces them to continue turning together, being able to remove the auxiliary motor.

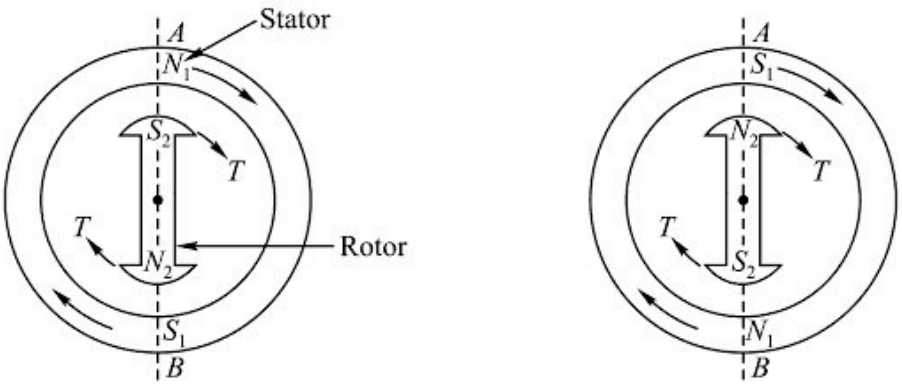

Figure 5. Vibration due to not self-starting (Electricalexams 2018-20)

Before beginning the study of the designed prototype, it is necessary to make a descriptive and comparative analysis between the different electric motors of the synchronous type depending on the rotor characteristics, to later focus on the prototype in question and explain the reasons for the election of the electro-magnetic equations that describe its behaviour.

The synchronous machine can be made up of:

1. **DC excited rotor(conventional synchronous motors)**
   1.1. Cylindrical pole rotor
   1.2. Salient-pole rotor

2. **Non-excited rotor(special synchronous motors)**
   2.1. Surface mounted permanent magnet
   2.2. Interior/buried permanent magnet

The next Fig 6 shows a scheme of the different configurations of these motor types

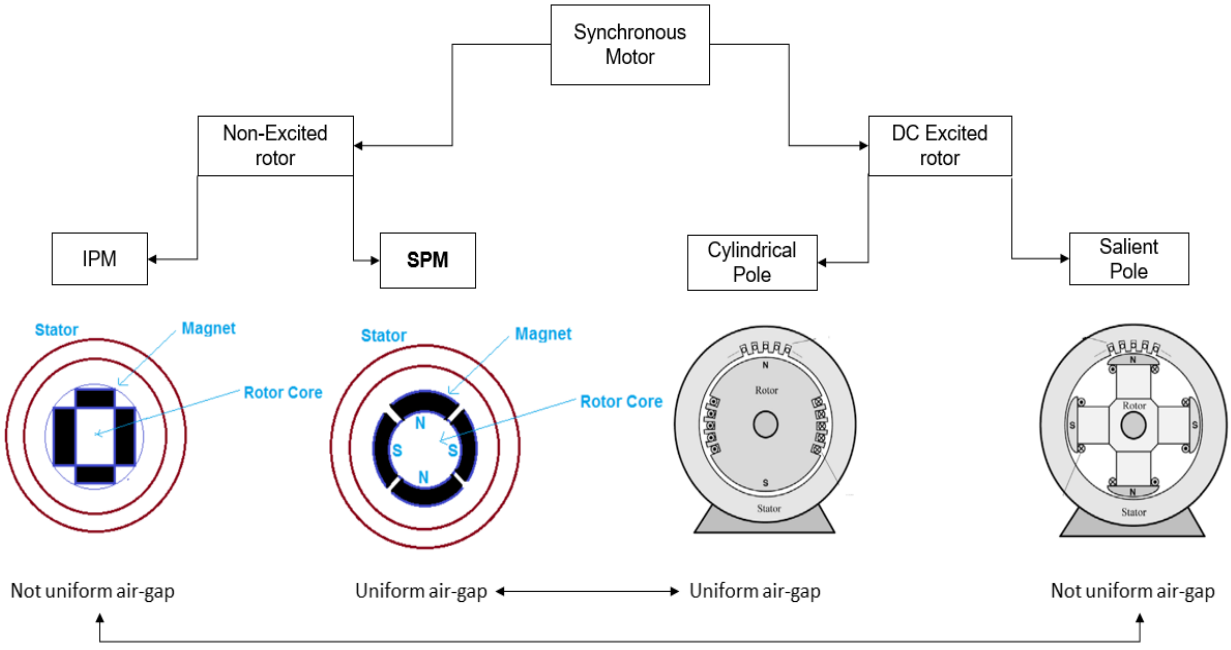

Figure 6. Synchronous motor configurations. Figures from (Electricalbaba, 2018)

From the previous scheme we can see how the DC excited cylindrical pole rotor has the same shape configuration as the Non-excited PM surface mounted motor(SPM), having both a uniform air gap, although the SPM motor apparently does not seem to possess this characteristic due to the protuberances of the magnets which would cause a variation in the air gap. However, we can consider it uniform since the magnetic permeability of the air is very similar to that of the magnets, and consequently the synchronous motor reactance is also constant, thus X_q (synchronous reactance of the q imaginary axis) = X_d(synchronous reactance of the d imaginary axis) =

Xs(synchronous reactance). This is a great advantage for the theoretical analysis of the motor since it simplifies the equations due to its configuration is completely symmetrical, then we only have to pay attention to the value of the synchronous reactance X_s.

In the case of the salient-pole rotor configuration, its asymmetric geometry causes a variation in the motor inductances (reactances), to have a rather complex analytical development. This is the case of the Salient pole DC excited motor and the case of the interior permanent magnet motor. Due to the above we can use the equations of the conventional CD excited cylindrical motor, which are much simpler to understand than those of the permanent magnets found in the literature. However, before calculating the equations of the cylindrical motor, the main differences between an excited motor and one of permanent magnets should be noted.

3.2 Difference between DC excited SM and PMSM. Back EMF

Back EMF

Eb (back EMF) = $(\boldsymbol{P} \times \boldsymbol{\varphi}) \times W_s$

- P(N°poles) ⇒ Constant
- φ(Flux linkage rotor) ⇒ Varies ~ I_f (Rotor field current)
- W_s(Synchronous speed) ⇒ Constant at constant frequency

⇓

Measured K_t (Back EMF constant)

Starting from the basis that we maintain the synchronous motor speed constant-this can be achieved by keeping the electric frequency of the stator constant- and the number of motor poles being a constant characteristic of the motor itself-, in a conventional synchronous motor we can control the magnetic flux density caused by the electromagnets feeding the winding of the rotor that causes them, with greater or lesser electric current I_f (electric field current), as can be seen in the Back EMF scheme. This also implies that if the back EMF can be controlled by controlling the rotor field current, we can also control the parameters that depend on those parameters. This is the main difference with respect to permanent magnet motors because, as their name indicates, the magnetic flux they produce is permanent. However, there are other methods of magnetic flux control of permanent magnet synchronous motors like the field weakening control method, but it is not the objective of this thesis to delve deeper into the motor control system, so for more information the bibliography exposed at the end of the thesis may be useful. Therefore Non-excited rotor(Permanent magnets) being SPM or IPM, represent the simplest configuration since it avoids the use of rotor winding in order to create the magnetic poles , however its application at high powers is limited since the magnetic flux densities of the magnets are not generally high.

3.3 Difference between IPM and SPM synchronous motors

Torque produced by a PM machine is developed by the stator MMF (or flux) interacting with the excitation flux provided by the rotor magnets in exactly the same way as in wound field machines (DC excited motors). Permanent magnet rotors are constructed in a wide variety of topologies but generally fall into two general classes (KWON, 2013).

Interior permanent magnet (IPM) designs: Also known as buried magnet machines, the magnets are mounted inside the rotor, held in place by steel pole pieces. An additional torque is produced by the rotor saliency in interior magnet machines as it happens in conventional salient-pole motor as we will see in the torque calculation section.

Surface permanent magnet (SPM) designs: The magnets are fastened directly on the rotor surface. For surface magnet machines there is no saliency effect and the uniform air gap equivalent circuit of the cylindrical rotor synchronous machine applies. Since the effective air gap is very long(from stator to the shaft) since we can take into account the magnets as air, the armature reaction MMF does not create much flux and the synchronous reactance is very small; only slightly larger than the stator leakage reactance.

3.4 Effect of load on a synchronous motor

The output torque-load angle curve has the following behaviour by varying the load angle:

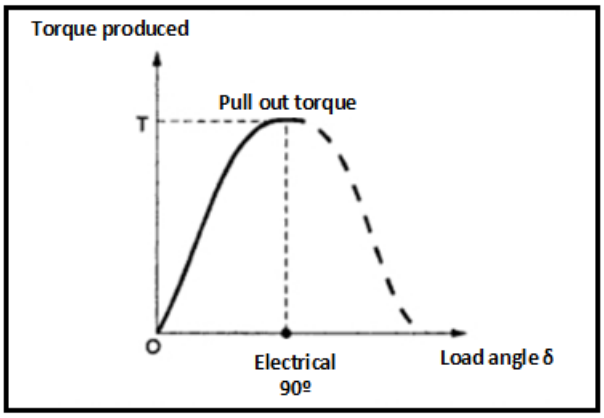

Figure 7. Torque-Load angle curve of a synchronous motor (Fraser, 1994)

We can check how the maximum torque (pull out torque) is reached when the load angle reaches 90º electric. When the load angle is higher than 90º the motor will be in the unstable region and it will be out of synchronism, then it will stop rotating and vibrate heavily due to the same reason it is not self-starting. The relationship between mechanical and electrical degrees is as follows:

$$\delta_m = \frac{\delta_e}{p} \tag{3.2}$$

Where δ_m is the mechanical load/torque angle, δ_e the electrical load angle and p the number of poles. These angles depend on the weight of load applied to the shaft. A synchronous motor always runs at constant synchronous speed, regardless of the load.

When the load on the shaft is increased, the rotor slows down for a moment, as it requires some time to take increased power from the line. In other words, it can be said that even if the rotor is rotating at synchronous speed, the rotor slips back in space because of the increase in the load. In this process, the torque angle δ becomes larger and, as a result, the induced electromagnetic torque increases. Then increased torque increases the rotor speed, and the motor again regains

the synchronous speed, but with the larger torque angle tan with the previous load situation. In the next image it can be seen how in the first situation the load angle is 0 (pole alignment between the stator flux and the rotor magnets flux) when no load applies, and in the second how the angle increases when increasing the load.

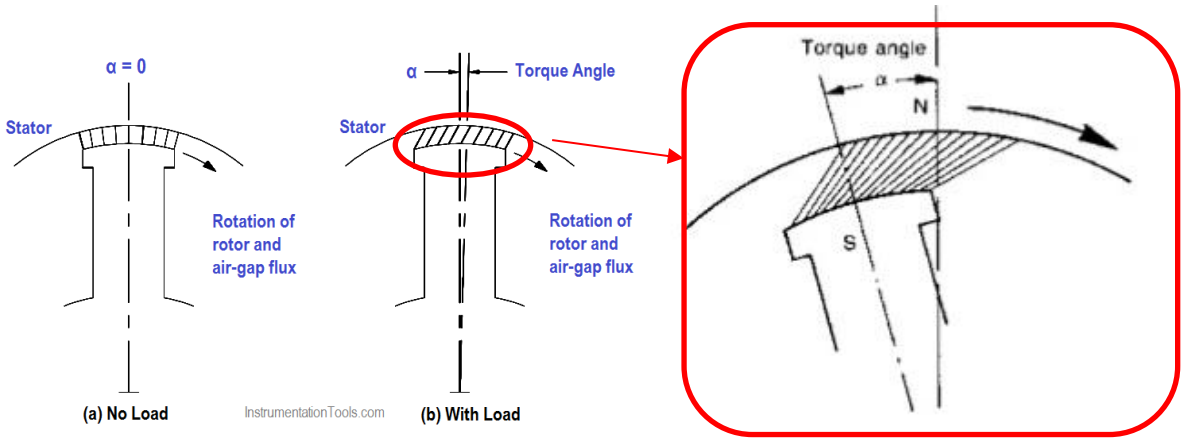

Figure 8. Load/torque angle (Starting a Synchronous Motor, 2020)

3.4.1 Phasor diagram of a synchronous motor under loads

It is possible to make an equivalence between the phasor diagram, electrical circuit and the equations of the Permanent Magnet motors with the conventional synchronous motors, the reason has been previously explained, but as a resume this has been done because the equations dependent on the load angle found of the PM literature were more complex to understand and it is not the main goal of this thesis to make a deep theoretical study on the behaviour of the permanent magnets synchronous motors. Therefore, considering a cylindrical rotor synchronous motor we have the next phasor diagram which is a vector description of the electrical parameters of the motor and its respective electrical circuit.

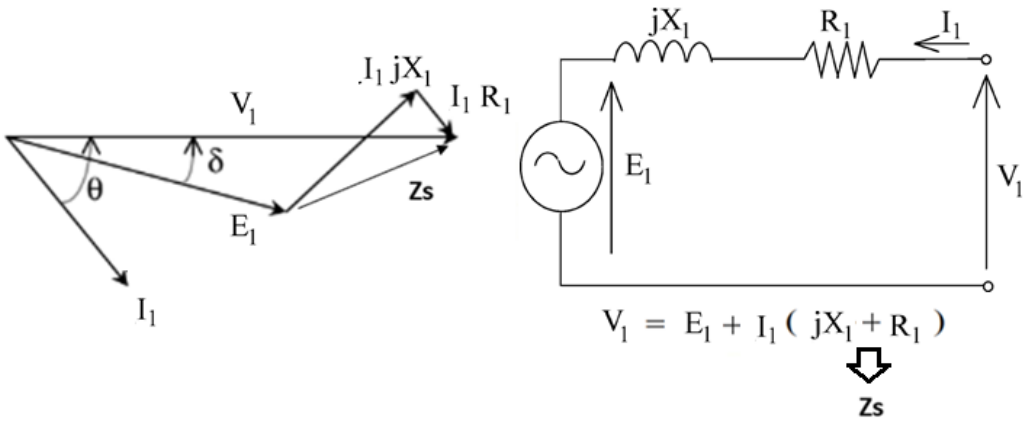

Figure 9. Phasor diagram and synchronous motor electrical circuit

Where V_1 is the terminal voltage (Volts), $E_1$is the back-EMF (Volts), $I_1$is stator current (Amps), δ the electrical load/torque angle (Degrees), θ the power factor presented at supply, $R_1$is the

armature resistance (Ohms), X_1 is the Armature reactance (Ohms), and $Z_s$is the impedance (Ohms). The resistance can be neglected and the phasor diagram would look like in figure 11, then, $E_1 = I_1 j\, Z_s \approx I_1 j\, X_s$.

3.4.2 Phasor diagram of the prototype PMSM under loads

Once the theoretical study of a synchronous cylindrical synchronous motor with its respective equations has been carried out, including electromagnetic torque and power, phasor diagram and electrical circuit, we can proceed to study the specific case of the synchronous motor designed in the institute.

The study of a conventional cylindrical engine has been carried out in the previous chapter with the objective of contrasting the differences between both behaviour models. The following study has been proposed by the author of this thesis without having been able to find in the literature of synchronous motors a means of verification that this study is correct, mainly because the characteristics presented by this engine are really uncommon, among them the very low measured phase inductance L (40 µH), and the high resistance of the winding R_a(4.2 Ω).

All synchronous electric motors found in the literature lack these characteristics since in all of them the winding resistance is almost negligible due to its low value compared to the value of the inductance L and then the reactance $X_s(2\pi f L)$. This is the main reason why the study of a conventional cylindrical synchronous motor has been done in the previous section.

It is worth noting again that these studies are carried out based on conventional synchronous motors, since there are equivalences between these and permanent magnet synchronous motors that have already been previously commented, with the aim of simplifying the study. Therefore:

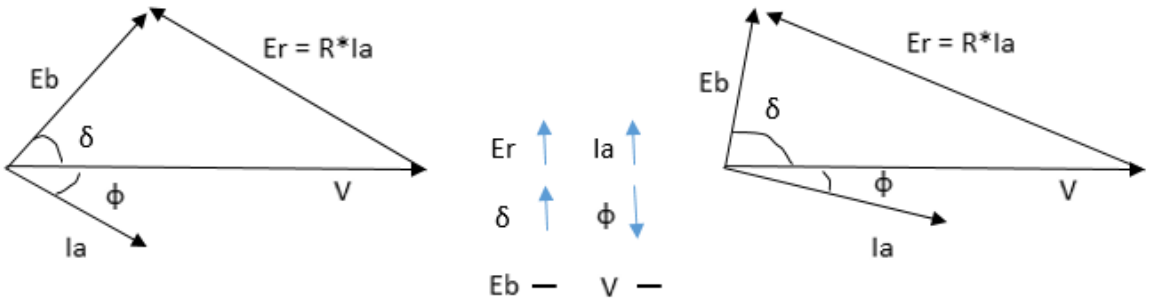

Figure 10. Phasor diagram synchronous motor proposed of for the case of the synchronous motor prototype under different loads

Where V is the terminal voltage (Volts), E_b is the back-EMF (Volts), $I_a$is the stator current (Amps), δ the electrical load/torque angle (Degrees), Φ is the power factor presented at supply, and R is the armature resistance (Ohms). The reactance can be neglected, $E_r = I_a R$.

In Figure 10 we can check the phasor diagram proposed under two different load situations (load 1 and load 2). It can be seen how the diagram changes the vector position completely in situation 2, as the load increases the load angle increases, and also the armature current, and therefore, since the resistance is a constant parameter the vector E_r also increases. However, the power factor angle decreases so the cos(phi) power factor increases, both the EMF Back and the supply voltage remain constant in this situation change.

The interesting thing about this process is the increment in the current flowing through the winding when the load increases, without having to vary any electrical parameter. This occurs because as we increase the load, we are increasing the power demanded by the motor to supply the weight of the torque caused by that load, thus, it is necessary to increase the input power to achieve the output torque demanded. And if the supply voltage and the back EMF are constant, the only way that the motor has to increase the input power as we will see later in the equations, is by increasing the winding current.

Difference with respect to the phasor diagram previously analysed:
In the case of the diagram in Figure 10, we can verify that there is no reactance since the measurements of the motor showed that it was much lower than the winding resistance, and it is neglected; on the contrary, the opposite happens in the conventional motor diagram where the reactance is much higher than the resistance. It is clear that the positioning of the phasor diagram changes completely when one of both (reactance, resistance) is taken into account, and the other is neglected.

3.5 Parameters calculation of the motor under loads

3.5.1 Parameters calculation of a typical cylindrical synchronous motor

Before describing the equations, it should be noted that this study has been done thinking on obtaining equations with relationship between the parameters that are going to be calculated and the load angle that depends on the load applied to the motor shaft since the measurements and data collected of the real motor were taken varying the loads, and in order to compare the results of the measurements with the results of the analytical calculation, it was necessary to look for the equations dependent on the load angle.
We can assume that the resistance of the stator phases is negligible (≈ 0 R_1) for most synchronous motors and as it is a cylindrical rotor, the air-gap is uniform and therefore its synchronous reactance X_1 can be considered as constant.

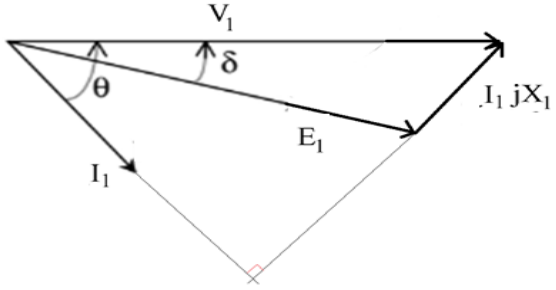

Figure 11. Phasor diagram without resistance

The electrical circuit equation of the motor neglecting the resistance is described as (Rodríguez Pozueta, 2018):

$$\bar{V} = \bar{E}_0 + jX_s\bar{I} \tag{3.3}$$

Then the armature current is:

$$\bar{I} = \frac{\bar{V} - \bar{E}_0}{jX_s} \tag{3.4}$$

These polar numbers can be written in polar form:

$$\bar{V} = V|0 \qquad \bar{I} = I|-\theta \qquad \bar{E}_0 = E_0|-\delta \tag{3.5}$$

$$\bar{I} = \frac{V|0 \; - E_0|-\delta}{jX_s} \tag{3.6}$$

$$\bar{I} = \frac{E_r}{X_s j} \tag{3.7}$$

Through trigonometry calculations of the phasor diagram, the vector E_r is equal to:

$$E_r = (V_t - E_f \cos\delta) + E_f \sin\delta \, j \tag{3.8}$$

We can obtain the current equation related with the load angle δ.

$$\bar{I} = \frac{(V_t - E_f \cos\delta) + E_f \sin\delta \, j}{X_s j} \tag{3.9}$$

To calculate the final apparent power we must obtain the current conjugate:

$$\bar{I}^* = \frac{(V_t - E_f \cos\delta) - E_f \sin\delta \, j}{-X_s j} \tag{3.10}$$

Complex apparent power can be finally obtained as:

$$\overline{S} = P + Qj = 3\overline{V}\,\overline{I}^{*} \tag{3.11}$$

$$\overline{S} = 3V\frac{(V_t - E_f\cos\delta) - E_f\sin\delta\, j}{-X_s j} = \frac{3V_tE_f}{X_s}\sin(\delta) + \left(\frac{3V_tE_f}{X_s}\cos\delta - \frac{3V_t^2}{X_s}\right) \tag{3.12}$$

Then, separating the real and imaginary parts of $\overline{S}$, the following expressions of the active powers P and reactive Q of a cylindrical synchronous machine are (Rodríguez Pozueta, 2018):

$$P = \frac{3V_tE_f}{X_s}\sin(\delta) \tag{3.13}$$

$$Q = \frac{3V_tE_f}{X_s}\cos\delta - \frac{3V_t^2}{X_s} \tag{3.14}$$

Dividing the power by the motor synchronism speed we obtain the electromagnetic torque equation. We must take into account that the motor losses are being neglected because, as previously stated, most synchronous motors have a much higher reactance than the resistance, thus the losses due to Joule effect can be neglected.

$$T = \frac{P}{W_s} = \frac{3V_tE_f}{X_sW_s}\sin(\delta) \tag{3.15}$$

For a Salient-pole synchronous motor: Through the process described above for the cylindrical motor, for a salient-pole synchronous motor we arrive to the equation of active power:

$$P = \frac{3V_tE_f}{X_d}\sin(\delta) + \frac{3V_t^2}{2}\left(\frac{1}{X_q} - \frac{1}{X_d}\right)\sin(2\delta) \tag{3.16}$$

And the output torque:

$$T = \frac{P}{W_s} = \frac{3V_tE_f}{X_dW_s}\sin(\delta) + \frac{3V_t^2}{2W_s}\left(\frac{1}{X_q} - \frac{1}{X_d}\right)\sin(2\delta) \tag{3.17}$$

Comparing the torque and power of a salient-pole machine with that of the cylindrical rotor it can be noted that:

- The cylindrical motor is equivalent to a salient-pole motor where the longitudinal synchronous reactors X_d and transverse X_q are equal (X_d=X_q=X_s)
- An additional torque appears in the salient-pole machine as was comment previously due to this difference of reactances depending on the axis of the rotor called reluctance torque which is a function of sin (2δ).

3.5.2 Parameters calculation of the prototype synchronous motor

As the calculation development of the electrical parameters was presented in the previous phasor diagram until arriving to the output torque and power; this analysis will only focus on the equation of active power and how it changes with respect to that obtained with the typical synchronous motor.

To do this, the equation already obtained from salient poles will be transformed until it becomes the equation of our motor.
This is the power equation of a conventional salient-pole synchronous motor, which is similar to that of the internal permanent magnet synchronous motor:

$$P = \frac{3V_t E_f}{X_d}\sin(\delta) + \frac{3V_t^2}{2}\left(\frac{1}{X_q} - \frac{1}{X_d}\right)\sin(2\delta) \tag{3.18}$$

It is worth making a series of considerations although some of them are repeated in order to clarify the situation of our motor:

1-Being our motor of the surface mounted permanent magnets type (SPM), the magnetic permeability of the magnets is similar to that of the air, so we could consider that there is a uniform air gap, and therefore there is no variation of the reactance, so $X_d = X_q = X_s$. In this way we could say that the description of a (SPM) is similar to that of a synchronous motor with a conventional cylindrical rotor, in which the division of its parameters on the d-q axes is not necessary, and this greatly simplifies the phasor diagram as well as the equations. In this way the second term that is the reluctance active power caused by the variation of the air gap (salient poles) can be eliminated:

$$P_{input} = P_{output} \Rightarrow 3\overline{V}\,\overline{I}cos(\Phi) = \frac{3V_t E_f}{X_s}\sin(\delta) \tag{3.19}$$

Having a resistance much higher than the reactance, the equation should be divided by the resistance instead of the reactance.

$$P_{input} = P_{output} \Rightarrow 3\overline{V}\,\overline{I}cos(\Phi) = \frac{3V_t E_f}{R_a}\sin(\delta) \tag{3.20}$$

3- When taking into account the resistance in this equation, the Joule effect losses should be taken into account. Therefore, the equation would look like:

$$P_{input} = P_{output+}P_{losses} \Rightarrow 3\overline{V}\,\overline{I}cos(\Phi) = \frac{3V_tE_f}{R_a}\sin(\delta) + 3I^2R_a \quad (3.21)$$

$$P_{output} = 3\overline{V}\,\overline{I}cos(\Phi) - 3I_a^2R_a \Rightarrow P_{output} = \frac{3V_tE_f}{R_a}\sin(\delta) - 3I_a^2R_a \quad (3.19)$$

However, since the power equation has to be obtained through trigonometric calculations from the phasor diagram, and by taking into account the resistance and not the reactance, the positioning of the vectors changes completely thus this last equation can not be correct since it has been taken from the trigonometric calculation of the x phasor diagram.

The trigonometric calculus development of the MPE PMSM is as following:

$$V = E_b\cos\delta + E_r\cos\Phi \Rightarrow \cos\Phi = \frac{V - E_b\cos\delta}{E_r = RI_a} \quad (3.23)$$

$$P_{input} = P_{output+}P_{losses} \Rightarrow 3VI_acos(\Phi) = 3VI_a\frac{V - E_b\cos\delta}{E_r = R_aI_a} \quad (3.24)$$

$$3VI_acos(\Phi) = 3\frac{V^2 - VE_b\cos\delta}{R_a} + 3I_a^2R_a \quad (3.25)$$

$$P_{output} = 3VI_acos(\Phi) - 3I_a^2R_a \Rightarrow P_{output} = 3\frac{V^2 - VE_b\cos\delta}{R_a} - 3I_a^2R_a \quad (3.26)$$

3.5.3 Inconsistent results problem

This last equation should be the one used to calculate the active power and the electromagnetic torque of the load dependent motor, remember that it is essential to find an equation for the load dependent torque applied because the test motor measurements were made for different loads. So this equation should get the same results as the torque measurements of our motor. However this has not been possible for the following reason, here is a brief explanation of the problem that will be developed in the chapter of the motor test: The behavior of the motor in the measurements has been unexpected, this is because when the load on the motor increased, the phase current measured in the winding decreased which makes no sense. This is a big problem since the equation described above is only valid for the opposite case. The current must increase by increasing the torque demanded by the load as explained above, so all the equations obtained from the phasor diagram of electrical parameters are not valid. This current problem will be explained in more detail in the corresponding chapter. But having not been able to find a correct equation that describes the electromagnetic torque related to the load angle, from a phasor diagram, we have proceeded to find solutions to verify the results of the measurements with the analytical calculations of the torque. The next chapter a solution is developed.

4 Analytical Calculations

4.1 Electromagnetic torque analytical calculation

One of the objectives of this thesis was the verification of the measured values of the motor test by comparing them with the analytical formulas and with the simulation results. It was decided that this comparison should focus on the electromagnetic torque that was measured for different mechanical loads on the shaft (different load angles), the equation finally used for this verification can be expressed as:

$$T_e = \frac{3}{2}(\mathrm{DL})(B_m \sin(\beta))(N_s I_m)\sin(\delta) \tag{4.1}$$

This expression, shows that the torque is determined according to (Krishnan, 2009) by "the product of bore diameter D and stack length L, magnet flux density B_m and magnet arc angle β, the number of turns per phase N_s, the line current I_m and finally the load angle. All these parameters can be easily obtained from the already designed motor but it is necessary the calculation of the magnet flux density B_m. Many different forms of this expression can be found in various publications and care must be taken to understand the definitions of various variables before the expression can be confidently exploited in the design".

4.1.1 Electromagnetic circuit and theoretical explanation

To do this, a simplification of the motor's magnetic circuit has been proposed below.

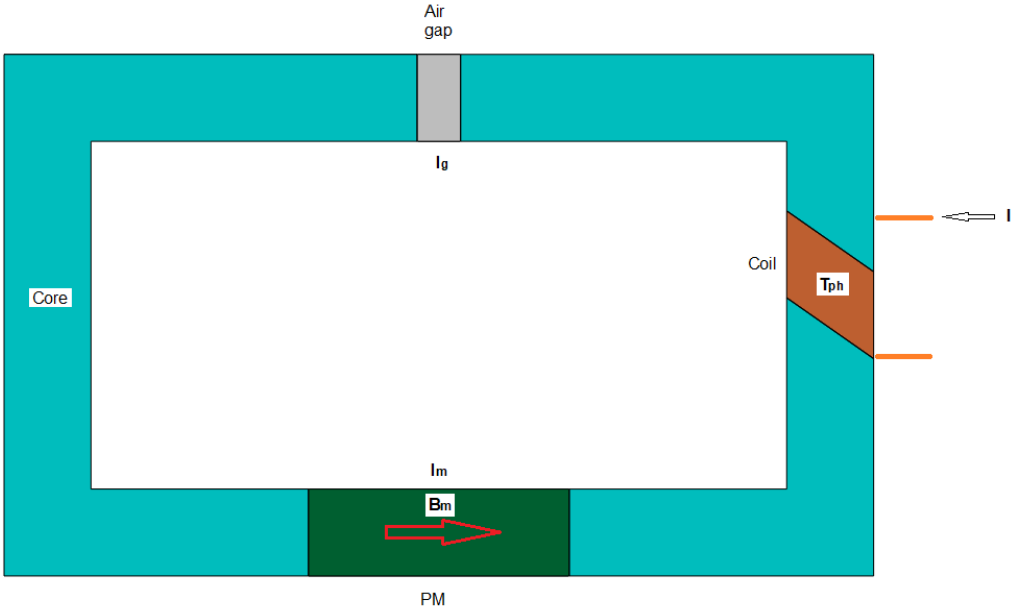

Figure 12. Magnetic circuit simplification of a PMSM (Krishnan, 2009)

PMSM experiences a magnetic field due to two circumstances, one is due to the excitation of the armature windings in the stator and the second is due to the field of PMs on the rotor. The interaction of these magnetic fields has certain consequences depending on whether the fields are

in the same direction or in opposite directions. External excitation (due to the winding excitation) is always intended to reduce the value of the total magnetic field in the air gap. Therefore, the flux due to the external excitation of the winding is directed in the opposite direction to that of the PM rotor flux.
Another inconvenient is that if the flux produced by the winding is in the same direction as that produced by the magnets, the total sum of the flux would produce the saturation of the stator core laminations and therefore higher core losses.
In summary and focusing this explanation on the value of the magnet flux density that we want to obtain for the calculation of the torque, the excitation produces a flux in opposition to that produced by the magnets, thus there will be a demagnetization and a decrease of the magnet flux density. This will be verified at the end of this theoretical development with the final equation.

The magnet flux density is given by (Krishnan, 2009):

$$B_m = B_r + \mu_o \mu_{rm} H_m \tag{4.2}$$

Where B_m is the magnet flux density, B_r is the remanence flux of the magnet, μ_o is the vacuum magnetic permeability, μ_{rm} is the relative magnetic permeability of the magnet and H_m is the magnet field intensity.

Neglecting the MMF (magnetomotive force) in the core, the MMF around the flux path is:

$$H_m l_m + H_g l_g = T_{ph} I \tag{4.3}$$

Where H_m is the magnet field intensity, H_g is field intensity in the air gap, $l_m$is the magnet lenght l_g the air gap lenght T_{ph} is the number of coil turns per phase and I is the current through the winding.

The magnet field intensity is then:

$$H_m = \frac{T_{ph} I - H_g l_g}{l_m} \tag{4.4}$$

And the magnetic field intensity in the air gap is related to the air gap flux density as:

$$B_g = \mu_0 H_g \tag{4.5}$$

There is a clear relationship between the flux densities in the air gap and magnet and it can be modelled as follows. The useful flux, which is in the air gap, is always a fraction of the magnet flux, which is expressed in terms of the leakage factor:

$$\Phi_g = \frac{\Phi_m}{k} \tag{4.6}$$

But the air gap and magnet flux in terms of the flux densities and areas of cross section are:

$$\Phi_g = B_g A_g \ ; \ \Phi_m = B_m A_m \tag{4.7}$$

We can consider for this calculation and for the followings in next chapters that the area of the magnets crossed by the flow is equal to that of the air gap so Am = Ag, although as we can see in this image the flow lines that cross the air gap generally cross a larger area than that of the magnets

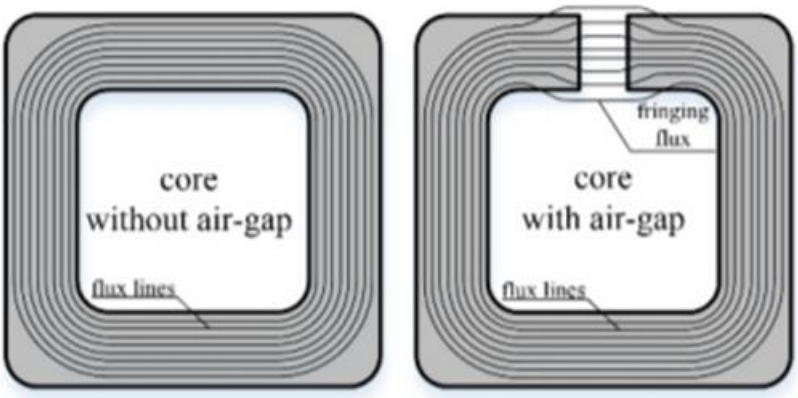

Figure 13. Flux lines distribution in magnetic cores; without air-gap and with air-gap (fringing flux can be observed) (Radoslaw Jez, 2014)

Based on the Permanent Magnet material properties we can easily obtain the value of the magnet flux density, necessary to calculate the electromagnetic torque (Krishnan, 2009).

$$B_m = \frac{1}{1 + \mu_{rm} \frac{l_g}{l_m} \frac{A_m}{A_g} \frac{1}{k}} \left[B_r + \mu_0 \mu_{rm} \frac{T_{ph} I}{l_m} \right] \tag{4.8}$$

The equation consists of two terms, the first term is the no electrical load flux density without externally applied field intensity (no current through the winding) and the second term is due to external excitation.

The excitation can cause an electromagnetic flux in the same direction of the magnet flux or opposite to the flux. When the excitation produces the flux in the same direction that the magnet, the magnet flux density will increase, however, this is not feasible in practice because it can lead to saturation of the stator core and more losses. Thus, the excitation has to produce the flux in the

reverse direction to the magnet and therefore produces the demagnetization and reduction of the magnet flux density.

Different forms of this equation exists in literature and it is necessary to understand the definitions of every parameter before the expression can be used in the design.

4.1.2 Electromagnetic torque results

The objective of this section is the calculation of the electromagnetic torque with the formula presented at the beginning of the chapter in order to compare it with the virtual simulation carried out and with the measurements of the motor test. Because the measurements were taken in a laboratory at normal conditions of pressure and temperature for different electric currents, the analytical calculation should also be at these conditions. Finally, the results of the calculation of the permanent magnet magnetic flux density necessary to calculate the torque, and the torque itself for different phase electric currents is:

Table 4.1: Magnet magnetic flux density and maximum electromagnetic torque values for NDFEB magnets depending on the electric current and at ambient normal conditions.

	I1 547(mA)	**I2 573(mA)**	**I3 641(mA)**	**I4 825.7(mA)**	**I5 852(mA)**	**I6 889.7(mA)**	**I7 946.5(mA)**	**T (K)**
Bm(T)	1.272967	1.273263	1.274039	1.276147	1.276447	1.276877	1.277525	**293.15**
T(N.m)	48.42	50.73	56.79	73.27	75.62	79	84.08	

4.1.3 Research study in PMs and induced Torque

Apart from the results compiled in the previous table, it was decided to extend this chapter through two interesting studies:

1. The first study has made a comparison of the maximum electromagnetic torque that the motor can achieve for different external temperatures. First, the magnetic flux produced by the NDFEB magnet used in the first prototype has been calculated for different temperatures, this shows us what is the variation in the magnetic capacity of the magnet under different external conditions. Once the results were obtained, the torque was calculated for these different values of magnetic flux. The study was not made for different temperatures using the SmCo12 magnet because it has not been possible to find in the literature its magnetic properties under cryogenic conditions.
2. The second study is a comparison of the maximum torque produced for two different types of permanent magnets, NdFeB and Sm2Co17. As a result, the most capable magnet material is obtained.

4.1.4 Research study results

4.1.4.1 Study 1: Maximum torque depending on ambient temperature for NdFeB magnets

The first results show us that the magnetic flux density hardly varies when the electric current varies, however it does vary when the ambient temperature varies, because the intrinsic properties of the magnetic material are improving at low temperatures, thus the flux will be higher, and this will have an immediate effect on maximum electromagnetic torque. The results also show us that by increasing the electric current the maximum torque will increase, and by decreasing the ambient temperature the maximum torque also increases, therefore the motor will have a greater output power capacity and it will be able to withstand higher loads at low temperatures such as at cryogenic temperatures (77 K), than at higher temperatures, such as under normal conditions (293.15 K).

Table 4.2: Magnet flux density values dependent on current and ambient temperature for NdFeB magnets

Bm(T)	I1 547(mA)	I2 573(mA)	I3 641(mA)	I4 825.7(mA)	I5 852(mA)	I6 889.7(mA)	I7 946.5(mA)	T (K)
Bm1	1.491713	1.492000	1.492751	1.494791	1.495081	1.495498	1.496125	**77**
Bm2	1.368538	1.368828	1.369588	1.371651	1.371945	1.372366	1.373001	**233.15**
Bm3	1.272967	1.273263	1.274039	1.276147	1.276447	1.276877	1.277525	**293.15**
Bm4	1.154652	1.154973	1.155813	1.158093	1.158418	1.158883	1.159585	**373**

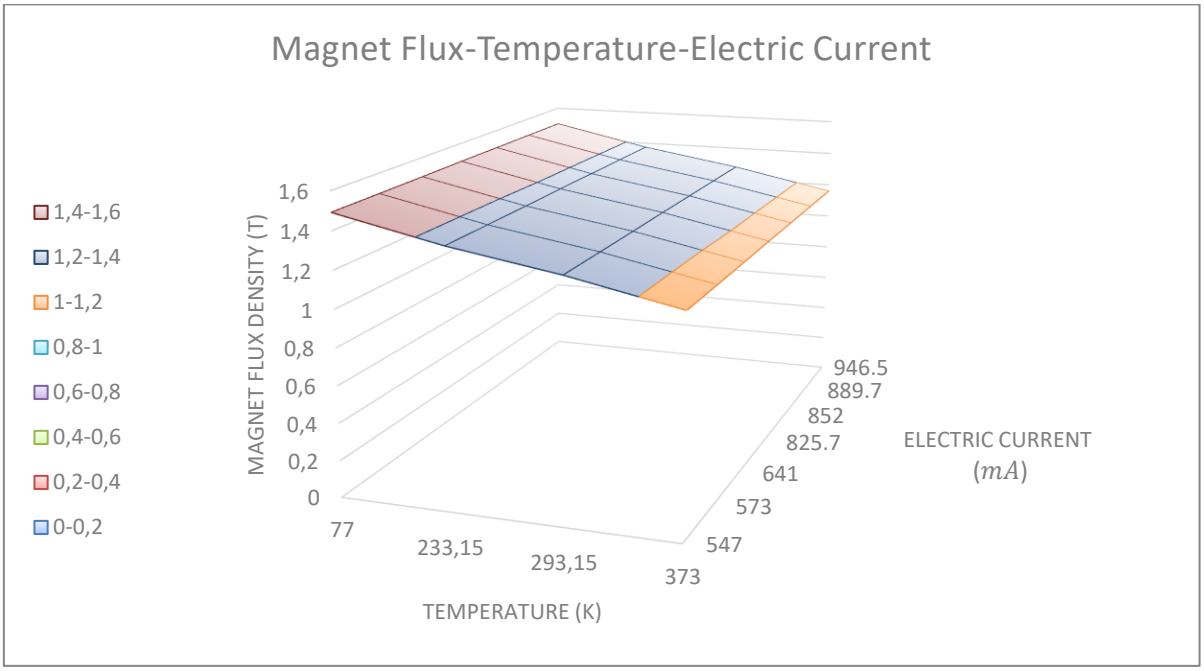

Graphic 4.1. Magnet flux-Temperature-Electric current graphic for NdFeB magnets

This first graph and table are necessary to observe how the magnetic properties of the magnet improve and so, the magnet flux density, as the temperature decreases. And hardly change with the electric current. This study is necessary to understand how the magnetic properties influence the following electromagnetic torque results.

Table 4.3: Maximum torque values dependent on current and ambient temperature for NdFeB magnets

Torque (mN.m)	I1 547(mA)	I2 573(mA)	I3 641(mA)	I4 825.7(mA)	I5 852(mA)	I6 889.7(mA)	I7 946.5(mA)	T (K)
T1	56.74	59.45	66.54	85.83	88.58	92.52	98.47	**77**
T2	52.05	54.54	61.05	78.76	81.28	84.91	90.37	**233.15**
T3	48.42	50.73	56.79	73.27	75.62	79	84.08	**293.15**
T4	43.92	46.02	51.52	66.49	68.63	71.7	76.32	**373**

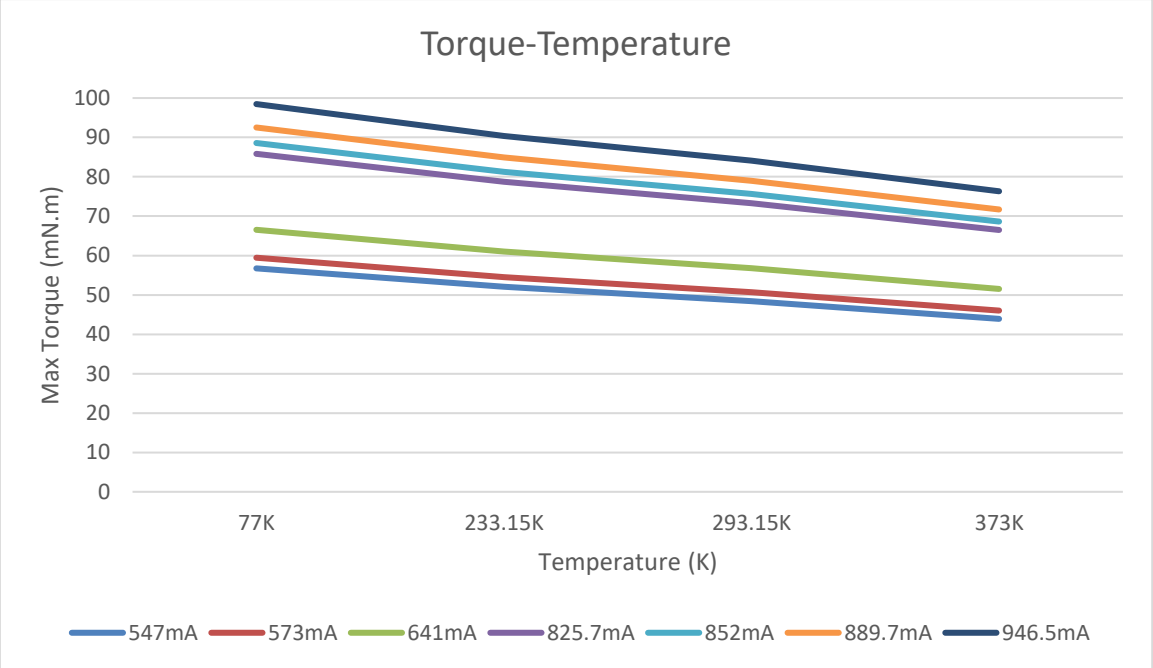

Graphic 4.2. Max torque-Temperature graphic for NdFeB magnets

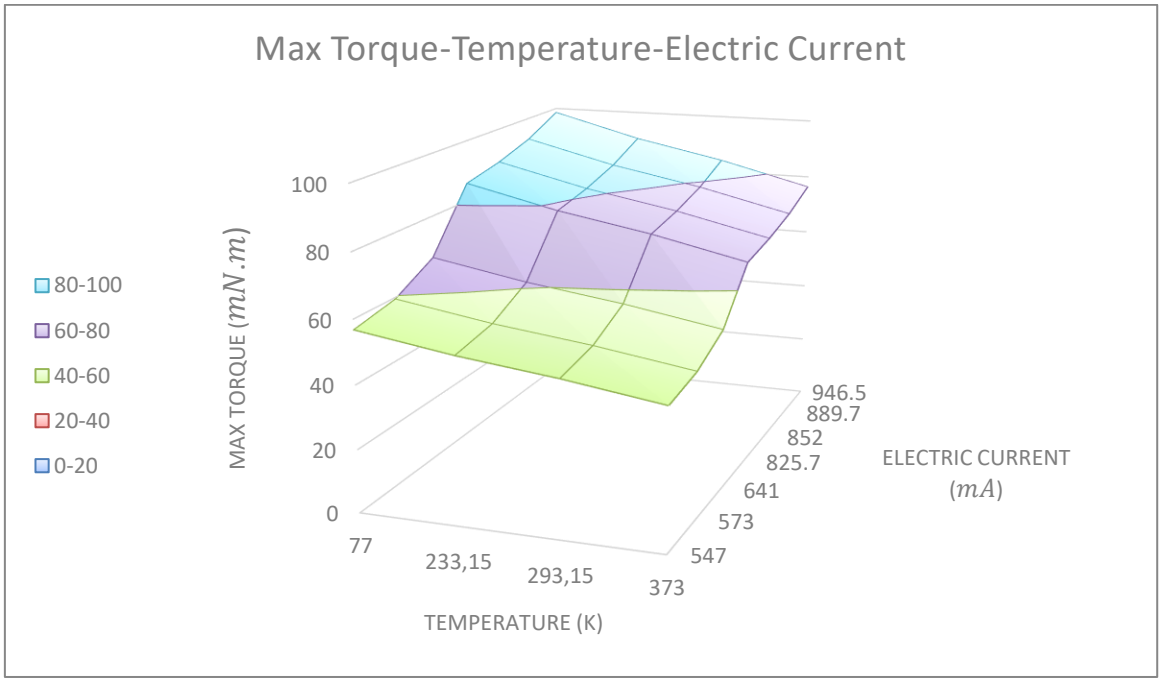

Graphic 4.3. Max torque-Temperature-Electric current graphic for NdFeB magnets

These graphs show how the maximum torque will be higher at low temperatures and at high electrical current supplies. Therefore, the motor will be able to withstand greater mechanical loads at cryogenic temperature conditions than at room temperature.

4.1.4.2 Study 2: Maximum torque depending on magnet material at normal temperature conditions

The following results show us that since the electromagnetic properties of the NdFeB magnet are higher than Sm2Co17 properties (Table 1: Material properties) at any temperature, its electromagnetic torque will also be greater regardless of the operating temperature.

Table 4.4: Maximum torque depending on the magnet material at normal conditions

Torque (mN.m)	I1 547(mA)	I2 573(mA)	I3 641(mA)	I4 825.7(mA)	I5 852(mA)	I6 889.7(mA)	I7 946.5(mA)	T (K)
Sm2Co17	39.45	41.34	46.28	59.74	61.67	64.42	68.58	**293.15**
NDFEB	48.42	50.73	56.79	73.27	75.62	79	84.08	

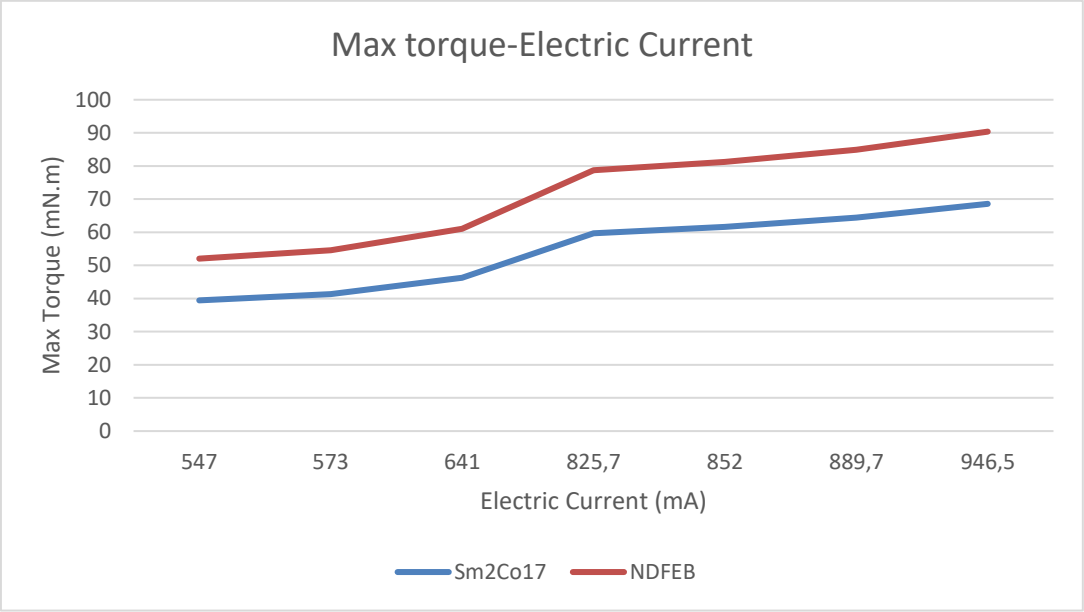

Graphic 4.4. Maximum torque depending on the magnet material at normal conditions

It can be seen from the graph that effectively, the red line representing the NdFeB magnet, will be able to obtain a maximum torque regardless of the electric current supplied to the motor, this is because the properties of the material, necessary to calculate the maximum torque, are higher and they are hardly influenced by the current supplied. However, a study of the SmCo17 magnet at different temperatures is very useful and should be carried out in the future, to improve the comparison between these two materials. Because the properties of the magnet at such low temperatures could not be found in the literature, it has not been done in this thesis.

4.2 Motor losses analytical calculation

In order to obtain the boundary conditions for thermal analysis, a power loss analysis is required (Faizan, s.f.). The losses represent the heat source and they can be divided into the following:

- Resistive losses (Winding losses)
- Iron losses
- Permanent magnet losses
- Mechanical losses

Resistive Losses

The electrical losses produced by the joule effect increase rapidly with the electrical load of the motor. The losses appear as heat generated by the electrical resistance of the winding to the current that flows through the conductors. They are also influenced by the temperature.

$$P_{Cu} = I^2 R = I^2 \rho \frac{l_{total}}{A_l} = I^2 \rho \frac{l\,(1 + l_{wk})\,w}{A_l} \tag{4.9}$$

Iron Losses

The iron losses are the second most important thermal source in the electric motors. These losses are due to the time variation of the magnetic flux density B, and they are divided into hysteresis and eddy current losses. The losses occur in the stator and rotor material. To reduce them, the stator is designed in the form of sheets instead of a compact block, in this way losses are minimized. In the case of our PMSM the rotor loss can be neglected, since it rotates synchronously with the poles produced by the stator.

Specific Hysteresis Losses

The magnetization and demagnetization process causes heating in the material which provokes energy dissipation. These losses are due to the difference between the energy transferred to the field during magnetization and that returned in demagnetization. The value of these losses coincide with the area enclosed by the contour of the hysteresis loop. Specific hysteresis losses $^{W}/_{Kg}$ are expressed by (Karnehm, 2017):

$$P_{Hyst} = k\frac{4\,H_C}{\rho}\,B_{max}\,f \tag{4.10}$$

Where k is a constant close to $k \approx 1$, f is the frequency, ρ the density of the material, H_C is the coercive field strength and B the flux density.

Specific Eddy Current Losses

These are currents induced in a conductive medium (with conductivity σ) as a consequence of being subjected to the flux of a variable magnetic field. In order to reduce the effect of the eddy currents, the ferromagnetic metal core is often divided in laminations.
The specific eddy current losses $^{W}/_{Kg}$ can be expressed by (Karnehm, 2017):

$$P_W = K_e {B_{max}}^2\, Ws^2 \tag{4.11}$$

$$Where\ K_e = \frac{d^2\sigma}{24}\ and\ W_s = 2\pi f \tag{4.12}$$

$$P_W = \frac{\pi^2\,\sigma\,d^2}{6\,\rho}{B_{max}}^2\,f^2 \tag{4.13}$$

Where d is the lamination thickness and σ is the specific conductivity of the material.

For most permanent magnet synchronous motors it is necessary to find the losses of both, hysteresis and eddy currents in the tooth and in the back stator separately but in the case of our motor, there are no teeth in the stator so it will only be necessary to Calculate what the maximum magnetic flux density will be in the stator back. We can consider that the cross section area of the magnet is the same as that of the air gap

$$A_m = A_g \tag{4.14}$$

and the scattering leakage factor is equal to 1.15, then

$$B_g = \frac{B_m\, A_m}{1.15\, A_g} \tag{4.15}$$

and based on, the max flux density in the stator has the following relation with the air gap flux density (Krishnan, 2009):

$$B_{\max(st)} = \frac{b_m B_g}{2\, h_{st}} \tag{4.16}$$

Where b_m is the magnet width and h_{st} the stator height.

Permanent magnet losses

Magnets are composed of materials that are characterized by having a relatively high electrical conductivity and therefore, this incite the appearance of eddy currents, causing losses and heating. They are given by:

$$P_m = \frac{V_m b_m^2 B_g^2 f^2}{12 \rho_m} \tag{4.17}$$

Where f is the frequency, V_m is the magnet volume, ρ_m is the magnet resistivity, the rest are already described above.

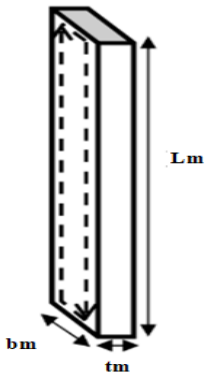

Figure 14. Eddy currents in magnet

Mechanical Losses

Mechanical losses will be neglected in this thermal analysis study due to the low speed at which the motor will be exposed, that will cause low mechanical losses in comparison with copper losses and iron losses.

These losses are composed of two parts: bearing friction losses and windage losses.

4.2.1 Results. Motor losses

All the parameter values intervening in these formulas can be seen in APPENDIX 1: MATLAB codes. Calculations.

- Copper losses $P_{Cu} = I^2R = I^2\rho\frac{l_{total}}{A_l} = I^2\rho\frac{l\,(1+l_{wk})\,w}{A_l}$ (W)

  Current from Comsol = 0.37434 (A)

  Resistance from Comsol model = 0.4748 (Ohm)

  → Pcu = 0.07 (W)

- Iron losses
  - Hysteresis → $P_{Hyst} = k\frac{4\,H_C}{\rho}B_{max}\,f$ (W/Kg)
  - Eddy current → $P_W = \frac{\pi^2\,\sigma\,d^2}{6\,\rho}B_{max}{}^2\,f^2$ (W/Kg)

  (Lamination thickness)

  Physt = 0.3546(W/Kg)

  Ptotal = 0.3612(W/Kg)

  Ped = 0.0066(W/Kg)

Ptotal = 0.3612(W/Kg)*Mstator(Kg) = 0.150 (Kg) = 0.054 W → Pstator = 0.054(W)

Motor losses = Pstator + Pcu = 0.125 W

4.3 Thermal analytical calculation

The theoretical analytical analysis carried out by the implementation of the equations that describe the heat transfer in the motor in the Matlab code which will be attached in the appendix of the thesis.

The heat flux developed during motor operation is based on the generation of heat in the winding due to the Joule effect and the generation of heat in the stator core due to hysteresis losses, and eddy currents which have been calculated in the previous chapter, therefore the goal of this analysis is not calculating the heat as this value is already known, but calculating the temperature distribution.

4.3.1 Basic concepts of heat transfer. Mechanisms

Heat transfer is defined as the transit of energy due to a spatial difference in temperatures. Being in the same or in different mediums, whenever there is a difference of temperatures there will be

heat transfer. There are three methods of heat transfer, conduction convection radiation that will be briefly explained focusing on the case of transfer produced on a cylindrical object such as an electric motor. The conduction is produced in a solid object, when there is a difference of temperature between two points of it. There is also conduction in the air, but its conductive properties are very low and it can be considered as an insulator. Convection refers to the heat transfer between a surface and a fluid at different temperatures. Thermal radiation is understood as the transfer of energy between two surfaces in the form of electromagnetic waves, this mode of transmission occurs between two surfaces even if there is no physical medium between them. For each transfer method there is an equation that quantifies the amount of energy transferred between two points.

4.3.1.1 Conduction heat transfer. Cylinder

In order to understand where the subsequent equations for the specific case of the motor are coming from, a theoretical study is carried out on the equations involved in heat transfer in a hollow cylinder with an inner radius r1 at temperature T1, and outer radius r2 at temperature T2 and of length L.

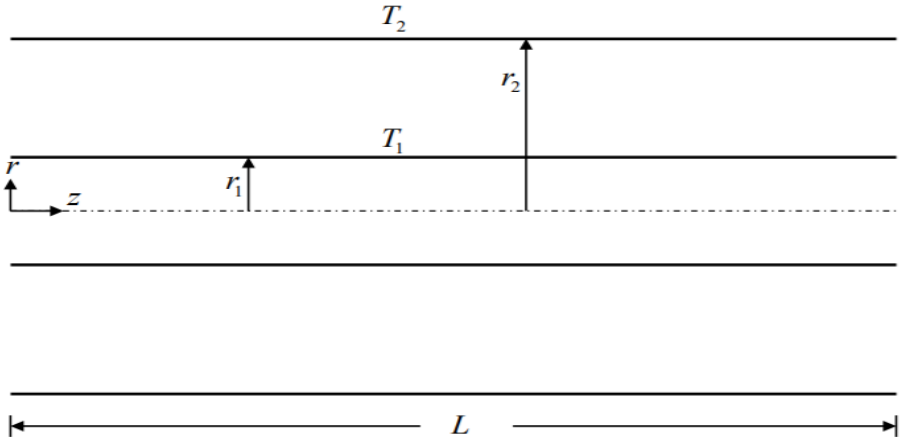

Figure 15. Cylinder model for heat transfer basic mechanisms description

The general equation of the conduction is then reduced in the unidimensional (radial) stationary case to (José Ramón Navarro Andreu y C. Nicolás Madrid Garcia):

$$\frac{1}{r}\frac{\partial}{\partial r}\left(r\frac{\partial T}{\partial r}\right)=0 \quad \Rightarrow \quad \frac{d}{dr}\left(r\frac{dT}{dr}\right)=0 \tag{4.18}$$

Having as boundary conditions:

$$\begin{aligned} r=r_1 \;\; ; \;\; T=T_1 \\ r=r_2 \;\; ; \;\; T=T_2 \end{aligned} \tag{4.19}$$

Integrating the general equation we get:

$$r\frac{dT}{dr} = B \;\; ; \;\; dT = B\frac{dr}{r} \tag{4.20}$$

Reintegrating we get the solution:

$$T = B\ln r + C \tag{4.21}$$

based on two integration constants calculated from the boundary conditions:

$$\begin{aligned} T_1 &= B\ln r_1 + C \\ T_1 &= B\ln r_1 + C \end{aligned} \tag{4.22}$$

$$B = \frac{T_2 - T_1}{ln\frac{r_2}{r_1}} \;\; ; \;\; C = T_1 - \frac{T_2 - T_1}{ln\frac{r_2}{r_1}} ln\, r_1 \tag{4.23}$$

replacing the constants, the following temperature distribution is obtained:

$$T = T_1 + \frac{T_2 - T_1}{ln\frac{r_2}{r_1}} ln\frac{r}{r_1} \tag{4.24}$$

Therefore, the temperature varies logarithmically through the cylinder wall instead of linearly as in a plate. The heat transmitted through the cylindrical layer can be calculated by Fourier's law:

$$q = -k_{12}A\frac{dT}{dr} = -k_{12}(2\pi rL)\frac{dT}{dr} = -k_{12}(2\pi rL)\frac{B}{r} \tag{4.25}$$

replacing the value of B results in the general conduction heat transfer equation:

$$q = \frac{2\pi Lk_{12}(T_1 - T_2)}{ln\frac{r_2}{r_1}} = \boxed{\frac{T_1 - T_2}{\frac{ln\frac{r_2}{r_1}}{2\pi Lk_{12}}}} \tag{4.26}$$

And the thermal conduction resistance is expressed as:

$$\boxed{R = \frac{ln\frac{r_2}{r_1}}{2\pi Lk_{12}}} \tag{4.27}$$

Where k_{12} is the conduction heat transfer coefficient.

4.3.1.2 Convection heat transfer. Cylinder

In the convective case:

$$q = h_c A \left(T_{1f} - T_2\right) \tag{4.28}$$

$$q = h_c 2\pi r L \left(T_{1f} - T_2\right) \tag{4.29}$$

and thermal the resistance is:

$$R = \frac{1}{2\pi r L h_c} \tag{4.30}$$

Where T_{1f} is the external fluid temperature, and T_2 is the cylindrical surface temperature, A is the external surface area of the cylinder and h_c is the convection heat transfer coefficient which will be explained in the following sections.
The form of these squared equations of the conduction and convection heat transfer will be used in the motor analysis for the design of the thermal network.

4.3.1.3 Radiation heat transfer. Concentric Cylinders

Based on (José Ramón Navarro Andreu y C. Nicolás Madrid Garcia) , the radiation exchanged between a gray body at an absolute temperature T1 towards the external environment T2 that surrounds the body, can now be calculated using the expression:

$$q = \sigma \, \varepsilon \, A \, (T_1^4 - T_2^4) \tag{4.31}$$

$$q = \sigma \, \varepsilon \, 2\pi r L \, (T_1^4 - T_2^4) \tag{4.32}$$

Where σ is the Stefan Boltzmann constant, with a value of $5.6697 \times 10^{-8} \frac{W}{m^2 K^4}$ in the SI, and ε is the emissivity of the gray surface which is in a value range between [0-1] and is numerically equal to the ratio of the radiation emission of a gray body E, with respect to that of a black one E_b.

$$\varepsilon = \frac{E}{E_b} \;\; ; \;\; E_b = \sigma T^4 \tag{4.33}$$

The radiation exchanged between two concentric cylindrical surfaces in order to describe the heat transfer in the vacuum gap of the motor is:

$$q = \frac{\sigma(T_1^4 - T_2^4)}{\frac{1-\varepsilon_2}{A_1\varepsilon_1} + \frac{1}{A_1 F_{12}} + \frac{1-\varepsilon_2}{A_2\varepsilon_2}} \tag{4.34}$$

Where A_1, ε_1 are the surface area and the thermal emissivity respectively of the inner cylindrical surface, $A_2 \varepsilon_2$ are the surface area and the thermal emissivity respectively of the outer cylindrical surface, and F_{12} is a radiation shape factor or view factor of the surface , which represents the fraction of energy leaving surface 1 and reaching surface 2

4.3.2 Motor analysis at normal conditions

Motor heat transfer division by components:

1. Stator analysis
    - Free convection heat transfer from the external area of the stator to the environment with normal conditions of pressure and temperature.
    - Conduction heat transfer between the exterior and the interior of the stator.
2. Winding analysis
    - Conduction heat transfer between the exterior and the interior of the copper winding.
    - Force convection between the interior surface of copper winding and the air gap flux.
3. Air gap analysis
    - Force convection between the interior surface of copper winding and the air gap flux.
    - Conduction heat transfer between the inner surface of the winding and the outer surface of the magnets.
    - Force convection between the outer surface of magnets and the air gap flux.
4. Magnets analysis
    - Force convection between the outer surface of magnets and the air gap flux.
    - Conduction heat transfer between the outer and the interior surface of the magnets.
5. Rotor shaft analysis
    - Conduction heat transfer between the outer surface of the rotor shaft and the centre axis of the motor.

The radiation transmission to the environment is neglected in this first analysis against the heat transmitted by convection. Subsequently, the same analysis will be carried out but in a cryogenic environment.

4.3.2.1 Assumptions

The thermal analysis is based on the following assumptions:

1- The thermal network required for an accurate thermal analytical analysis is complicated. In a cylindrical electrical motor, the radial, axial and circumferential heat transfer should be analysed separately, however only radial heat transfer will be analysed in order to reduce complexity of the model and because the Multiphysics simulation will deliver the final results.
2- A simplification of the model will be made by converting permanent magnets and winding into two unifom cylinders.

3- The heat losses that have been previously calculated will act as the heat source. Mechanical losses as well as losses in permanent magnets will be neglected, so only losses in the stator and winding will be taken into account.
4- The winding will assume the sum of all losses, and will act as the only heat source so the transfer direction will be from the outer surface of the winding to the motor interior, and from the surface of the stator to the environment.
5- All the thermal properties of the air both in the air gap and outside will be selected at room temperature. These are usually selected at medium temperature between the fluid and the contact surface, but taking into account the thermal simulations already carried out, the temperature difference between the environment and the maximum temperature reached by the engine is minimal (1.25K) at stationary operation.

4.3.2.2 Heat transfer model

The thermal analysis of multiple cylindrical layers, consisting of several different materials in intimate contact and cylinders with convective contour conditions, can easily be done by resorting to a thermal circuit through an electrical analogy. The electrical motor is divided geometrically into 8 parts or nodes. Each node is a heat source represented by the temperature of every contour material and it is connected to the thermal resistances for the interconnection to other nodes. Ad it has already been explained in the previous chapters, the heat represented by the losses is transferred from the node T4 represented by the temperature surface between the winding and the inner surface of the stator that will have the maximum temperature, with directions towards the interior of the motor and towards the environment. The resistances are the denominators of the fractions.

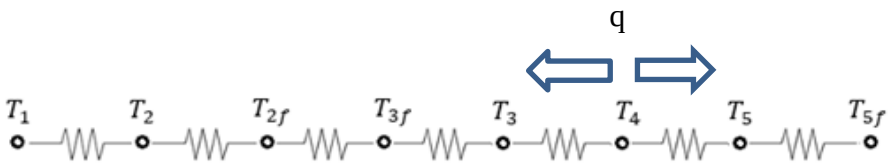

$$q_{loss} = \frac{T_1 - T_2}{\frac{ln^{r_2}/_{r_1}}{2\pi L k_{12}}} = \frac{T_2 - T_{2f}}{\frac{1}{2\pi r_2 L h_1}} = \frac{T_{2f} - T_{3f}}{\frac{ln^{r_3}/_{r_2}}{2\pi L k_{2f3f}}} = \frac{T_{3f} - T_3}{\frac{1}{2\pi r_3 L h_2}} = \frac{T_3 - T_4}{\frac{ln^{r_4}/_{r_3}}{2\pi L k_{34}}} = \frac{T_4 - T_5}{\frac{ln^{r_5}/_{r_4}}{2\pi L k_{45}}} = \frac{T_5 - T_{5f}}{\frac{1}{2\pi r_5 L h_3}} = \frac{T_i - T_j}{R_i}$$

Table 4.5: Node-surface assignment

Nodes	Surfaces
Node T1	Inner magnets surface=Outer shaft surface
Node T2	Outer magnets surface
Node T2f	Inner air-gap surface
Node T3f	Outer air-gap surface
Node T3	Inner copper winding surface
Node T4	Outer copper winding surface=Inner stator surface
Node T5	Outer stator surface

Node T5f	Environment

Table 4.6: Thermal resistance assignment

Thermal resistances	Resistance description
Resistance (T1-T2)	Magnet conduction resistance
Resistance (T2-T2f)	Magnet-Air gap convection resistance
Resistance (T2f-T3f)	Air gap conduction resistance
Resistance (T3f-T3)	Air gap-winding convection resistance
Resistance (T3-T4)	Winding conduction resistance
Resistance (T4-T5)	Stator conduction resistance
Resistance (T5-T5f)	Stator-Ambient convection resistance

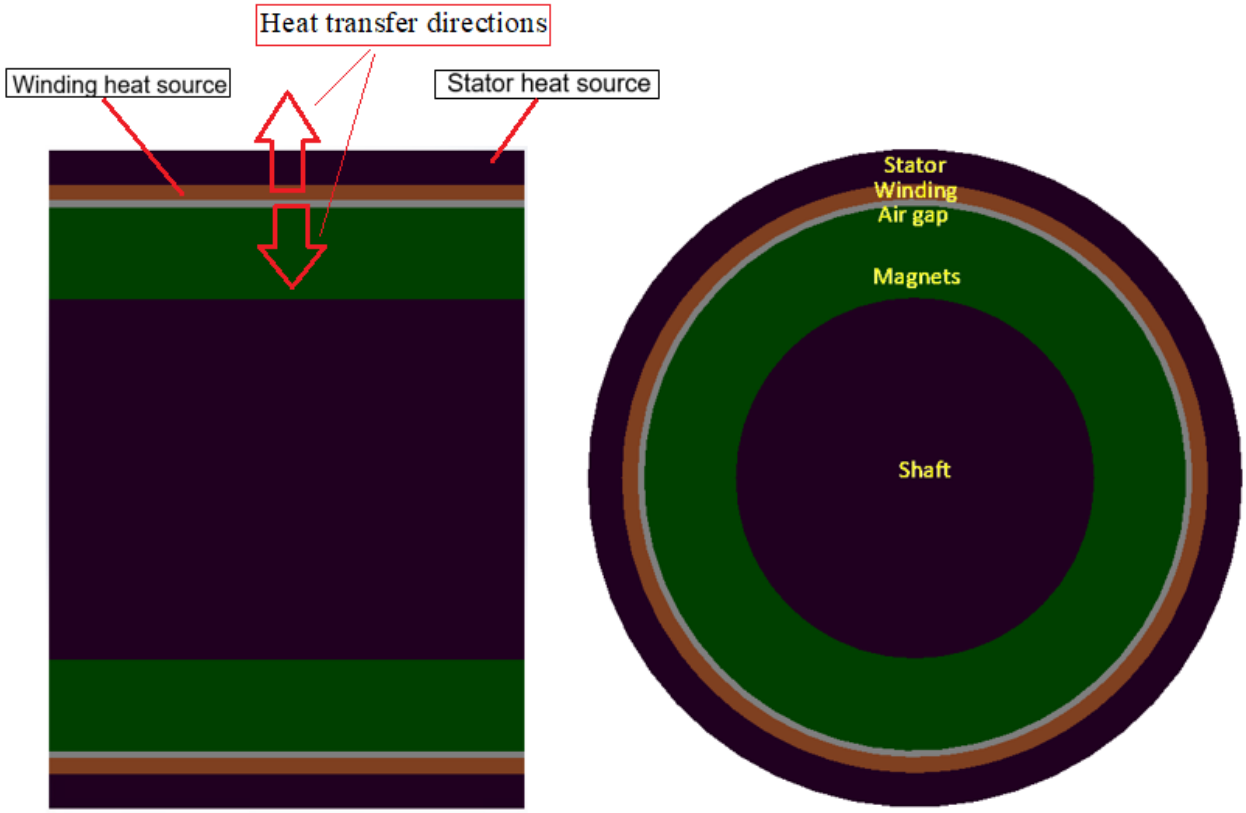

Figure 16. design by CAD solidworks, of the simplified motor; the sources of heat and the directions of the heat flow towards the interior and exterior of the motor

4.3.2.3 Stator analysis

4.3.2.3.1 Stator convection

The convection heat transfer in the stator goes from the higher temperature of the external surface T_5 to the environmental temperature (293.15 K) T_{5f} and it can be represented by:

$$q_{loss} = h_3 A \left(T_5 - T_{5f}\right) \tag{4.35}$$

Where q is the convection heat transfer, A the transfer area of the motor, h_3 the heat transfer coefficient by convection, T_5 as the temperature motor surface, and T_{5f} the ambient temperature. As we already know the q losses value, it is evident there are two parameters to be found in order to have the equation complete, one is the convection transmission coefficient h3 and the other is the surface temperature T5. However, in order to obtain h3 it is necessary to know in advance the value of the surface T5 for **two issues**:

1. The properties of the air involved in the calculation of the dimensionless numbers that will be explained below must be measured at the average temperature of the film. between T5 and T5f.
2. The Grashof number necessary to calculate h3 depends on the difference between these two temperatures.

Both issues will be explained in the development of the procedure when they appear on the scene.

To find the coefficient h_3 many factors must be taken into account, such as the geometry of the system, as well as the physical properties and characteristics of the fluid flow.
For the theoretical analysis of free convection of the motor towards the environment, a cylinder in horizontal position has been proposed as a simplification of the motor.

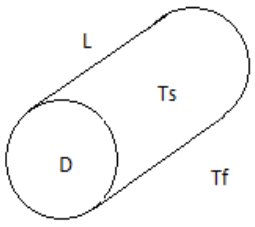

Figure 17. Cylinder model for heat transfer

Being free convection, the air fluid properties are evaluated at average film temperature. This is the **first issue** to be solved mentioned above because the surface temperature is unknown.

$$T_{af} = \frac{T_5 + T_{5f}}{2} \tag{4.36}$$

For the study in question, the average film temperature will be taken as the ambient temperature under normal conditions (293.15 K) since taking into account previous simulations in which the increase in surface temperature is a few Kelvins above the ambient temp, we can conclude that the real average temperature does not move far from 293.15 K and so the values of the properties.

Table 4.7: Air properties at T_{af}

Air property	Name	Unit SI
β	Coefficient of thermal expansion	$^1/_K$
ν	Kinematic viscosity	$^{m^2}/_s$
k	Thermal conductivity	$^W/_{m.K}$
P_r	Prandtl number	Dimensionless

Due to the complexity of the differential equations that describe the processes of heat transfer, practical problems are solved according to empirical correlations obtained from experimental research. These correlations are expressed as a function of certain dimensionless parameters that represent the different processes of relevance that constitute the heat transfer phenomenon. Each parameter has a specific physical meaning, and depending on the problem it can be determined which parameters must intervene. For the given problem three dimensionless parameters are used. The Grashof number Gr_D represents in free convection an analogous role to that of the Reynolds number Re_D in forced convection. The regime type (laminar or turbulent) is specified by the numerical value of the $Gr_{D.}P_r$ product.

$$Gr_D = \frac{g\ \beta\ (T_s - T_f)\ D^3}{\nu^2} \tag{4.37}$$

Where D is the motor diameter, g the gravitational acceleration.

The calculation of the Grashof number Gr_D is the **second issue** to be solved as T5 is unknown. To solve it, an iterative method has been proposed for the calculation of h and T5. It will begin taking as a value of T5 300 K with which we will finally obtain a determined value of h to calculate the value T5 by means of the heat transmission equation. Of course the value of T5 obtained will be different from the one proposed for the number of Grashof, however this procedure will be repeated iteratively changing the value of T5 in the number of Grashof replacing it with the calculated result, until both values are equal. Then that will be considered the true value of T5 as well as that of h.

The Prandtl number $\mathrm{P_r}$ controls the relative thickness of the momentum and thermal boundary layers. When Pr is small, it means that the heat diffuses quickly compared to the velocity (momentum). It can be obtained from the air properties tables.

$$\mathrm{P_r} = \frac{\nu}{\alpha} \tag{4.38}$$

The Nusselt number represents the ratio of convective to conductive heat transfer at a boundary in a fluid. And It can be determined by:

$$Nu_D = C\ (Gr_D\ \mathrm{P_r})^{m} \tag{4.39}$$

Where C and m are constants values that depend on the result of the product $Gr_{D.}\mathrm{P_r}$.
Finally the heat transfer coefficient by convection is obtained by the following expression

$$h_3 = \frac{Nu_D\ k}{D} \tag{4.40}$$

And it can be obtained T5 from the heat transfer equation:

$$q_{loss} = \frac{T_5 - T_{5f}}{\frac{1}{2\pi r_5 L h_3}} \tag{4.41}$$

4.3.2.3.2 Stator conduction

The conduction heat transfer in the stator goes from the higher temperature T_4 to T_5 and it can be represented by:

$$q_{loss} = \frac{T_4 - T_5}{\frac{ln^{r_5}/_{r_4}}{2\pi L k_{45}}} \tag{4.42}$$

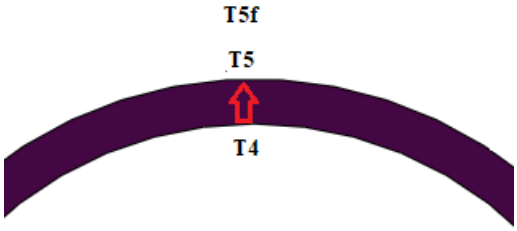

Figure 18. Conduction heat transfer stator

Where T_4 and r_4 are the temperature and radius of the inner surface; and T_5 r_5 of the outer surface.

4.3.2.4 Winding analysis

The conduction heat transfer in the winding goes from the higher temperature T_4 to T_3 and it can be represented by:

$$q_{loss} = \frac{T_3 - T_4}{\frac{ln\,{}^{r_4}/_{r_3}}{2\pi L k_{34}}} \tag{4.43}$$

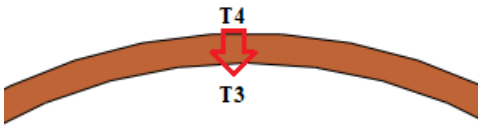

Figure 19. Conduction heat transfer winding

Where T_4 and r_4 are the temperature and radius of the outer surface; and T_3 r_3 of the inner surface.

4.3.2.5 Air gap heat transfer analysis

4.3.2.5.1 Air gap convection

One of the most important and particular aspects when analyzing in thermal analysis of an electric motor is to accurately model the heat transfer produced in the air gap.

Based on (Ruiz, 2014) Heat transfer in the air gap of cylindrical machines with a smooth rotor (in general, induction machines or buried magnets) is solved by assuming that the air in the air gap behaves like a Taylor-Couette, which occurs in the gap between two concentric cylinders that rotate with each other, and separated by a small distance (see Figure 20). The heat transfer in this type of space was treated for the first time by Taylor and his research was extended by Gazley.
Although there is recent research that offers new formulation for convection in the air gap of machines of different types [Howey et al., 2012], in this study the classical formulas of Taylor and Gazley have been used, since they are also validated by other authors [Staton et al., 2005; Motor-CAD, 2014].
To model convection in the air gap, correlations based on these two classical studies are used [Taylor, 1935; Gazley Jr., 1958], who evaluate Taylor's number to obtain the Nusselt number of these surfaces. Taylor's number assesses whether the flow is laminar, vortex or turbulent:

$$Ta = Re\sqrt{\frac{l_g}{R_r}} \tag{4.44}$$

To calculate convection in cylindrical rotating surfaces a correlation is used for rotating cylinders

around the air at constant temperature [Kendoush, 1996]. Where the Reynold number is:

$$Re = \frac{\frac{\pi\, n\, D}{60} D}{v} \tag{4.45}$$

And for the concrete case of the air gap:

$$Re = \frac{\frac{\pi\, n\, l_g}{60} D}{v} \tag{4.46}$$

Then the Taylor number can be expressed as:

$$Ta = \frac{\pi\, n}{30\, v} \sqrt{l_g^3\, R_r} \tag{4.47}$$

$$Nu_g = \frac{h_g l_g}{k} = \begin{cases} 2 \\ 0.212\, Ta^{0.63} Pr^{0.27} \\ 0.386\, Ta^{0.5} Pr^{0.27} \end{cases} \begin{cases} if\ Ta < 41 \\ if\ 41 < Ta < 100 \\ if\ Ta > 100 \end{cases} \tag{4.48}$$

From this formula it can be obtained the convection heat transfer coefficient h_g ($h_1 and\ h_2$in the thermal resistances) of the air gap needed to calculate the convection resistance between the air gap and the rotor and stator surfaces.

$$q_{loss} = \frac{T_{3f} - T_3}{\frac{1}{2\pi r_3 L h_2}} \;;\; q_{loss} = \frac{T_2 - T_{2f}}{\frac{1}{2\pi r_2 L h_1}} \tag{4.49}$$

In the previous expressions n is the rotor rotational speed in R.P.M, v is the kinematic viscosity of the air at average film temperature (rotor surface temperature), l_g is the length of the air gap; R_r is the radius of the rotor and k is the conductivity of air at average film temperature.

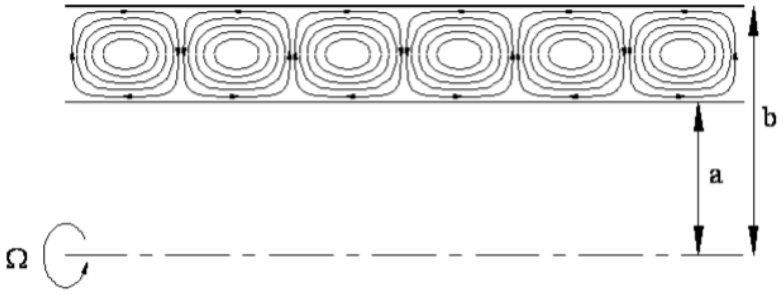

Figure 20. Taylor vortex in the concentric two-cylinder hollow with rotation.

4.3.2.5.2 Air gap conduction

The conduction heat transfer in the air gap goes from the higher temperature T_{3f} to T_{2f} and it can be represented by:

$$q_{loss} = \frac{T_{2f} - T_{3f}}{\frac{ln^{r_3}/_{r_2}}{2\pi L k_{2f3f}}} \tag{4.50}$$

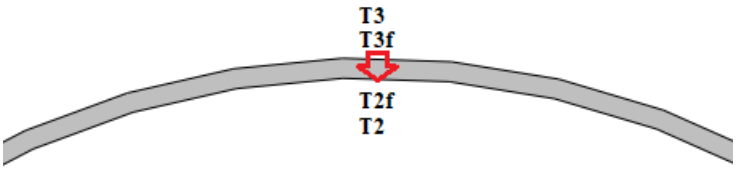

Figure 21. Conduction heat transfer air gap

Where T_{3f} and r_3 are the temperature and radius of the outer surface; and T_{2f} r_2 of the inner surface.

4.3.2.6 Magnet analysis

The conduction heat transfer in the winding goes from the higher temperature T_4 to T_3 and it can be represented by:

$$q_{loss} = \frac{T_1 - T_2}{\frac{ln^{r_2}/_{r_1}}{2\pi L k_{12}}} \tag{4.51}$$

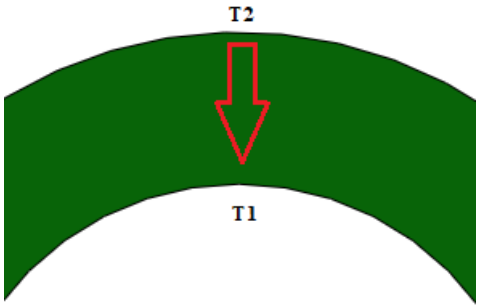

Figure 22. Conduction heat transfer magnet

Where T_4 and r_4 are the temperature and radius of the outer surface; and T_3 r_3 of the inner surface.

4.3.2.7 Rotor shaft analysis

It will be considered that given the high thermal conductivity properties of the rotor shaft material, the temperature on the outer surface of the shaft calculated in the magnet analysis (inner surface temperature of magnet) will be uniform in the complete shaft.

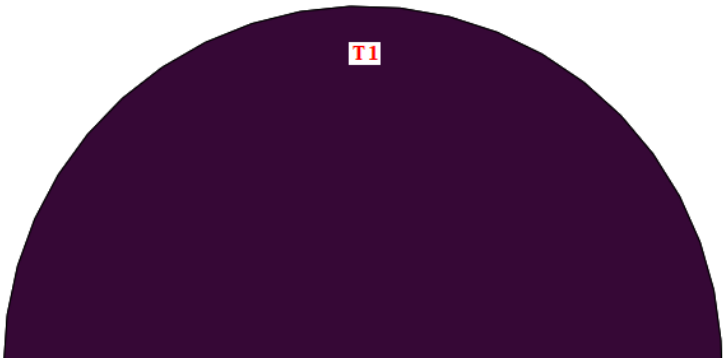

Figure 23. Rotor shaft temperature

4.3.2.8 Analytical results. Temperature distribution normal conditions

We can check how the highest temperature is on the external surface of the winding/ internal stator surface, and the surface temperature decreases both in the external direction of the heat flow and towards the interior of the motor.
We can also appreciate how the temperature barely varies on the three outermost surfaces due to the high thermal conductivity of the materials, however there are appreciable temperature jumps in the heat transferred produced in the air gap, to subsequently achieve the homogeneity of temperatures in the magnets and the shaft.

Table 4.8: Temperature distribution at normal conditions

T5	T4	T3	T3f	T2f	T2	T1
296.7739K	296.7793 K	296.7792 K	296.5916 K	295.995 K	295.8809 K	295.7667 K

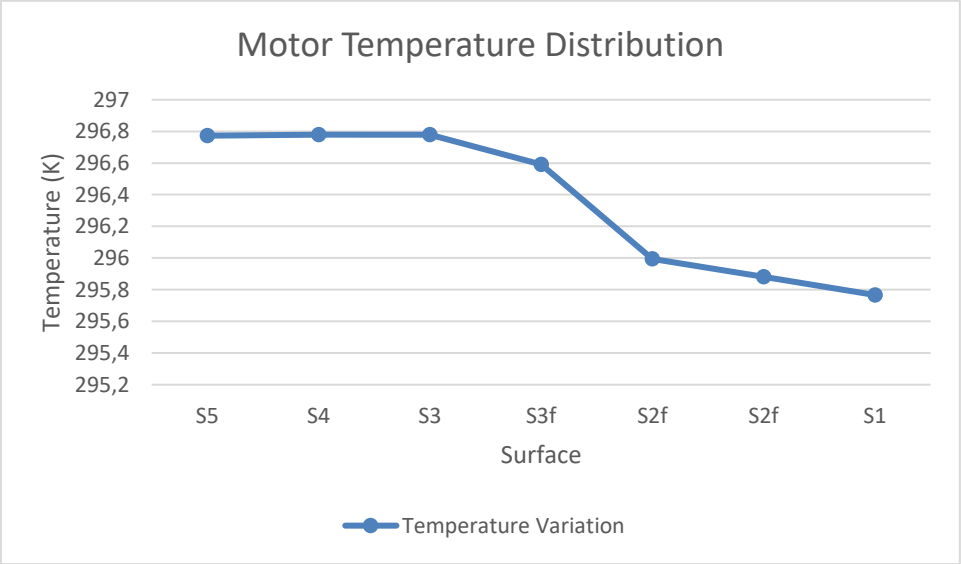

Graphic 4.5. Motor temperature distribution at normal ambient conditions

4.3.3 Motor analysis at cryogenic conditions

In the cryogenic ambient temperature and vacuum pressure heat transfer model, there is no convection so the previous analysis performed for the engine operating in an environment of normal conditions of pressure and temperature would not be valid and the convection equations must be eliminated.

In the following model the equations that describe the conduction behavior apply in the same way as in the previous model and to save writing the equations for every component will not be repeated in this model, only the equations corresponding to the radiation transfer process will be added. Radiation in this case can be described with two equations.

1. Radiation from the external surface of the engine to the environment:

$$q = \sigma \, \varepsilon \, 2\pi r L \, (T_1^4 - T_2^4) \tag{4.52}$$

2. Radiation from the inner surface of the winding to the magnets through the vacuum gap

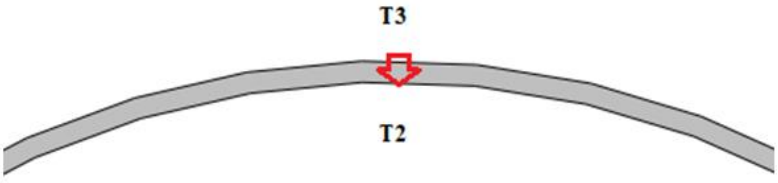

Figure 24. Radiation heat transfer vacuum gap

$$-q = \frac{\sigma(T_2^4 - T_3^4)}{\frac{1-\varepsilon_2}{A_1\varepsilon_1} + \frac{1}{A_1 F_{12}} + \frac{1-\varepsilon_2}{A_2\varepsilon_2}} \tag{4.53}$$

As the heat is from the outer surface to the inner surface, the heat is negative. And the shape factor is equal to 1, it can be obtained from the next graphics.

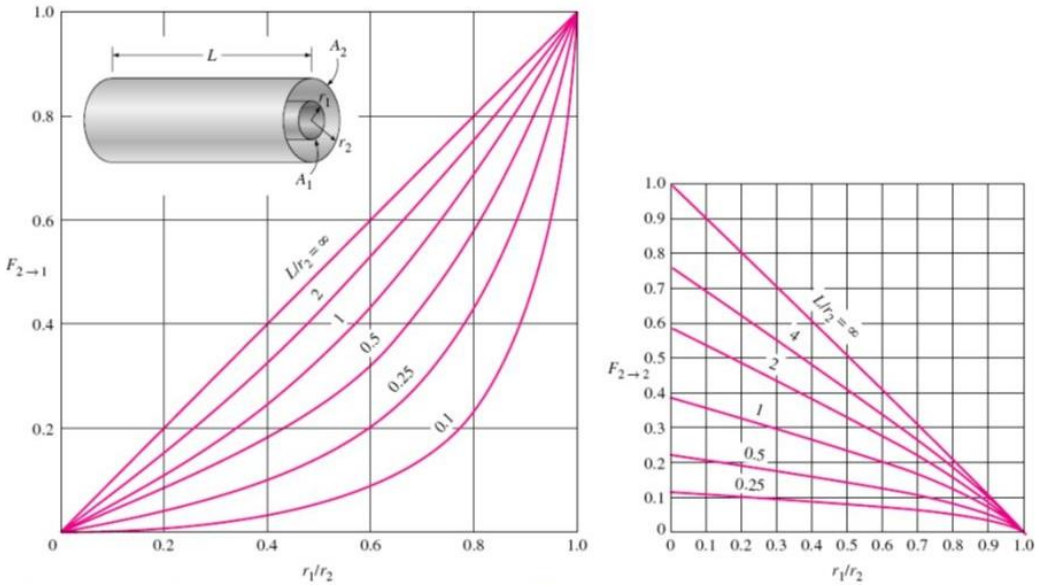

Graphic 4.6. Shape factor graphics for two concentric cylinders

4.3.3.1 Analytical results. Temperature distribution at cryogenic conditions

In this analytical calculation there have must been some calculating failures, since the temperature results obtained for the rotor surfaces had complex number values, however the stator and winding surface temperatures are consistent with the results obtained in the simulation as we will see in the respective chapter. Although the two last temperatures are not consistent, the values obtained in the simulation (85 K) have been used to design the graphic.

Table 4.9: Temperature distribution at cryogenic conditions

T5	T4	T3	T2	T1
135.0619 K	135.0673 K	135.0672 K	x	x

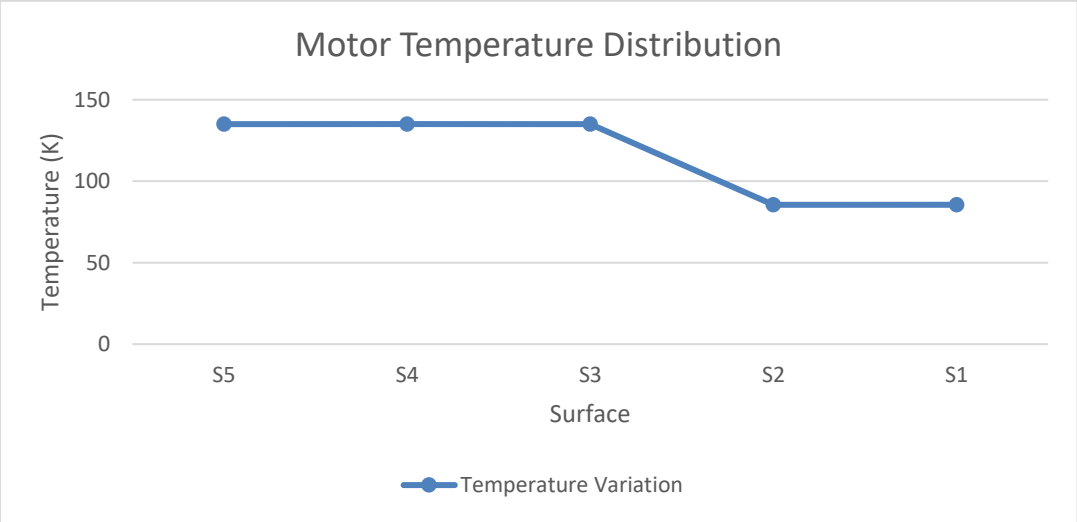

Graphic 4.7. Motor temperature distribution at cryogenic ambient conditions

4.4 Thermal contact resistance. Theory

According to the UPCT book "Transmisión del calor" (José Ramón Navarro Andreu y C. Nicolás Madrid Garcia), in the analysis of the heat conduction through solids of multiple layers, as is the case with our motor, a perfect contact has been assumed at the interface between two different material layers and, as a consequence, no temperature drop has been obtained between the surfaces in contact. This situation occurs when the joining surfaces are perfectly smooth and produce perfect point-to-point contact. However, even the seemingly smooth surfaces have rugosity that originate zones with contact points and zones with holes filled with air. This circumstance has not been taken into account for the thermal analysis of this thesis, but it is worth being explained theoretically for possible future solutions and achieve an optimum precision in the thermal analysis.

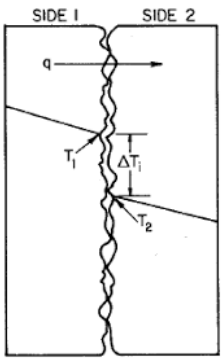

Figure 25. Imperfect contact between surfaces

As a result of this type of union in an interface there will be a large number of peaks (real contact) and spaces of variable sizes filled with air that will act as an insulator due to the low thermal conductivity of the air. Basically, a union interface between two materials has a certain resistance

to heat transmission and this resistance per unity area of the interface is called Thermal Contact Resistance $R_c\left(\frac{m^2K}{W}\right)$.
If the heat flux across two solid surfaces in contact is $\frac{q}{A}$ and the effective temperature difference in the interface is ΔT_{12}, the thermal contact resistance in the interface is:

$$R_c = \frac{\Delta T_{12}}{\frac{q}{A}} \tag{4.54}$$

It can also be expressed as:

$$R_c = \frac{1}{h_c} = \frac{\Delta T_{12}}{\frac{q}{A}} \tag{4.55}$$

where h_c is the heat transmission coefficient called Thermal Contact Conductance.

The values of thermal contact resistance or conductance have been determined experimentally and are usually found within the ranges of: $5\,e^{-7} < \ R_c \ < 5\,e^{-4}$ and $\ 2e^3 < h_c < 2e^5$.
Thermal contact resistance can be minimized by applying a thermally conductive liquid, called thermal grease, such as silicone oil, on surfaces, before compressing with each other. Another procedure consists in introducing gases more conductive than air between the surfaces or inserting thin sheets of silver stannous copper nickel or aluminum among them.
This tip can be used for future motor models and for any machine to study thermally. In the case of our motor it can be applied between the stator laminations or between the magnets embedded in the rotor

5 COMSOL Software Simulations

5.1 Electromagnetic simulations

5.1.1 Modeling PMSM dynamics in COMSOL Multiphysics

Since the result that we need to obtain in this simulation is only the electromagnetic torque, the following brief explanation of the simulation is focused on the dynamic modelling of the 2D simulation. There are other more extensive works such as (Bratke, 2018) explaining in detail the electromagnetic simulations. Nevertheless, a brief explanation of the simulation software framework will be explained in the thermal analysis. Based on (Paudel, 2016):

"The material properties used in this model are listed in the table 1. The RMS current is maintained at I_{RMS} = 1 A per winding for the 2D simulation. The three-phase winding is excited at f = 8 Hz.

We use the Rotating Machinery, Magnetic interface to simulate the electromagnetic fields in this three-phase PMSM. Since all the electrical and magnetic material properties are linear, the default Ampère's Law node works without any modification. We model the three phases using the Homogenized and Multi-turn Coil features. The number of turns for each winding is n_0= 4. Each stranded wire carries 1[A] current with 120° out of phase between the three phases. The currents through the three phases are described as":

$$I_A = 1[A]\cos(W_0 t)\sqrt{2}$$

$$I_B = 1[A]\cos(W_0 t + 120\ [deg])\sqrt{2} \qquad (5.1)$$

$$I_C = 1[A]\cos(W_0 t - 120\ [deg])\sqrt{2}$$

Here, 1 A is the RMS value of the input current so we need to multiply it with $\sqrt{2}$ to make it a peak value, and W_0=$2\pi f$ is the angular electrical speed.

According to (Paudel, 2016) "We can obtain the electromagnetic torque in the rotor directly by using the Force Calculation feature in the Rotating Machinery, Magnetic interface. By adding this feature, the spatial component of the magnetic forces (rmm.Forcex_0, rmm.Forcey_0, rmm.Forcez_0) and the axial torque (rmm.Tax_0) in this interface can be obtained when postprocessing. The Force Calculation feature simply integrates the Maxwell stresses over the entire outer boundary of the domain selection. Since this method is based on surface integration, the computed force is sensitive to mesh size. When using this method, it is important to always perform a mesh refinement study to correctly compute the force or torque.

The alternative approach would be to use Arkkio's method of torque calculation, a volume integration of the product of the magnetic flux densities. In this method, the electromagnetic torque in 2D models of electrical rotating machines can be calculated using the following expression":

$$T_e = \frac{1}{\mu_0(r_o - r_i)} \int r B_r B_\Phi dS \tag{5.2}$$

Arkkio's method theory;

"Where r_o is the outer radius, r_i is the inner radius, and S is the cross-sectional area of the air gap. The magnetic flux density in the radial and azimuthal directions is B_r and B_Φ , respectively. The rotational motion of the rotor is given by the following two equations":

$$\frac{dw_m}{dt} = \frac{T_m - T_L}{I} \tag{5.3}$$

$$\frac{d\Phi}{dt} = w_m \tag{5.4}$$

Where T_m is the rotor axial electromagnetic torque, T_L is the load torque, w_m is the angular speed of the rotor, and Φ is the angular position of the rotor. It is modeled using the Global ODE and DAEs interface in two separate Global Equations nodes as shown in the picture below.

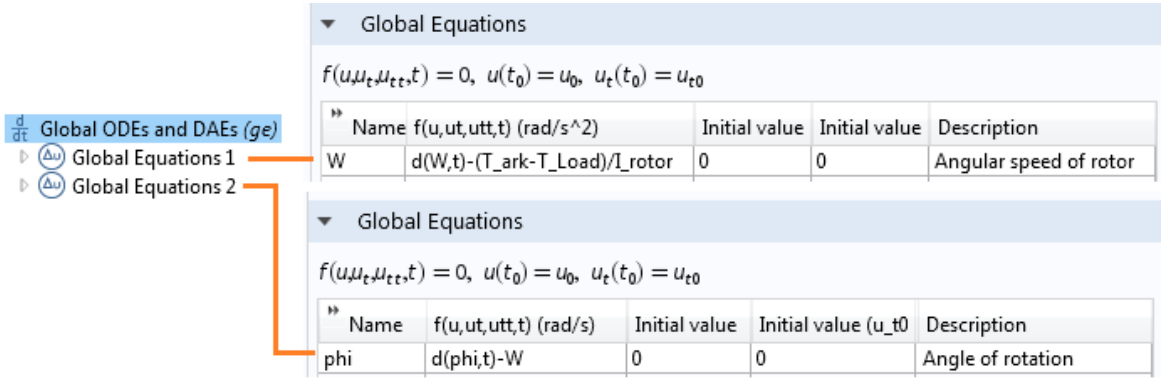

Figure 26. Implementing the differential equations for rotor angular velocity and angle using the *Global ODEs and DAEs* interface. (Paudel, 2016)

5.1.2 Electromagnetic results

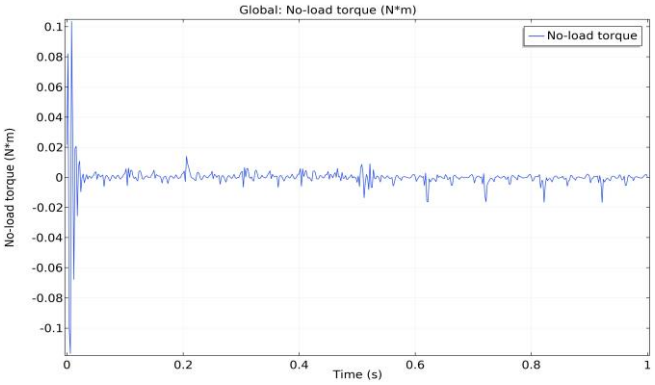

Figure 27. No-load output torque

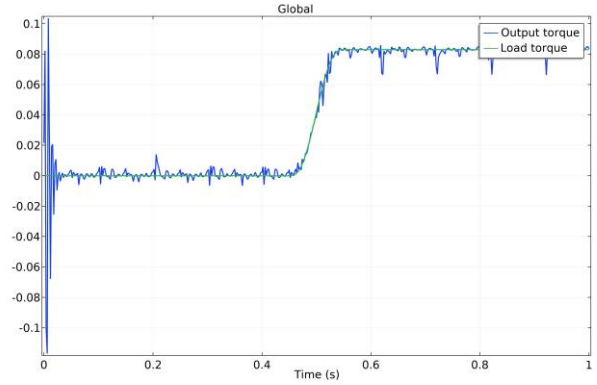

Figure 28. Loaded output torque

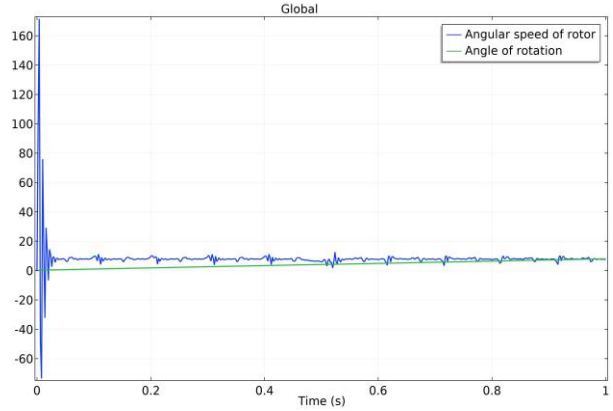

Figure 29. Rotational speed of the motor (10 rad/s)

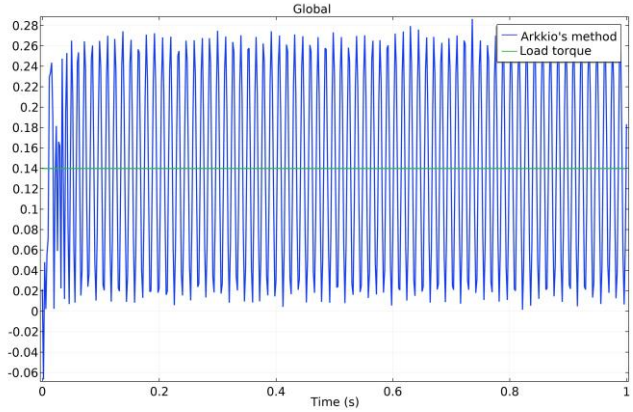

Figure 30. Loaded at 0 (s) output torque

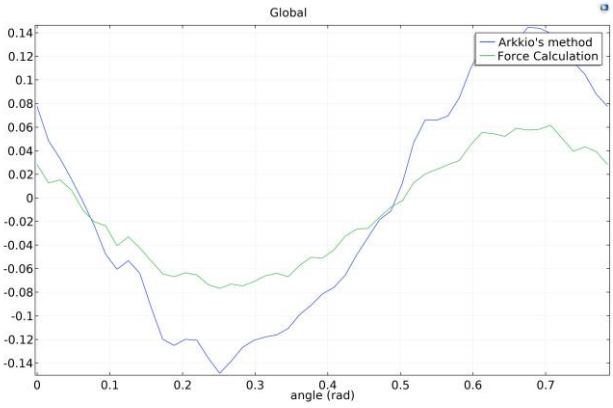

Figure 31. 3D simulation. Output torque (Arkkio and force calculation methods) Parametric sweep

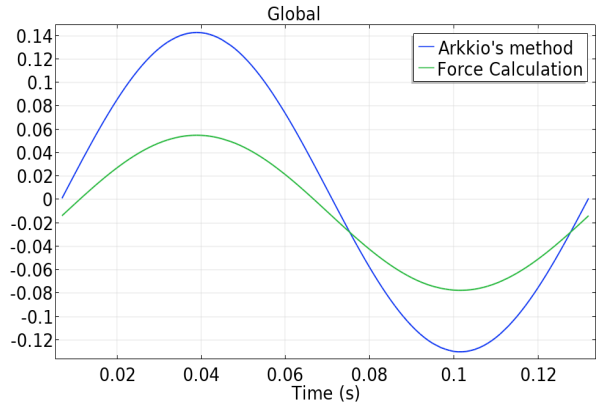

Figure 32. 3D simulation. Output torque (Arkkio and force calculation methods) Time dependent

The Figure 27 is the no-load output torque of the motor, and Figure 28 is the electromagnetic torque for a load of 0.08 (N.m). The Figure 29 shows the kinematic behaviour of the motor and how the angular speed of around 10 rad/s remains constant regardless of the load 0.1 (N.m) applied. In the Figure 30, a load of the same magnitude as the previous one was applied but for

t=0(s), thus the torque response shows this random behaviour without achieving stability and following the path of the load, unlike in the previous load situation. The captures 31 and 32 were taken from the 3D simulation. Number 31 was carried out by the author of this thesis and number 32 was taken from (Bratke, 2018). Next is the explanation of the behaviour of Figures 27,28,31,32.

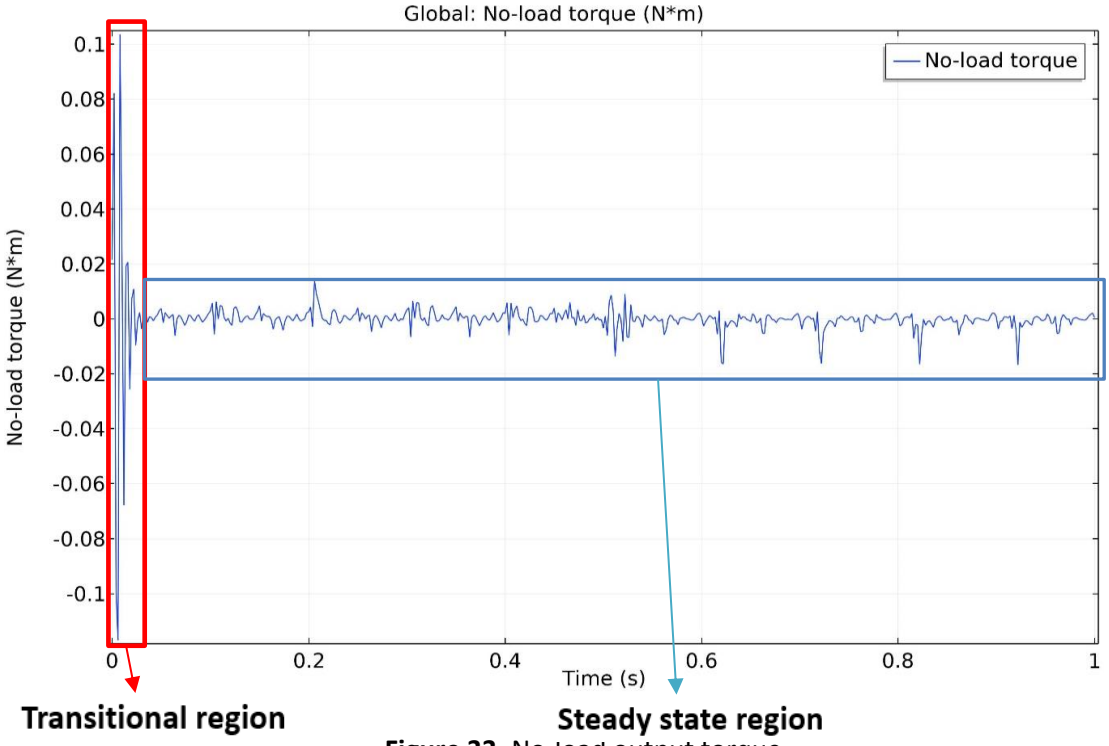

Figure 33. No-load output torque

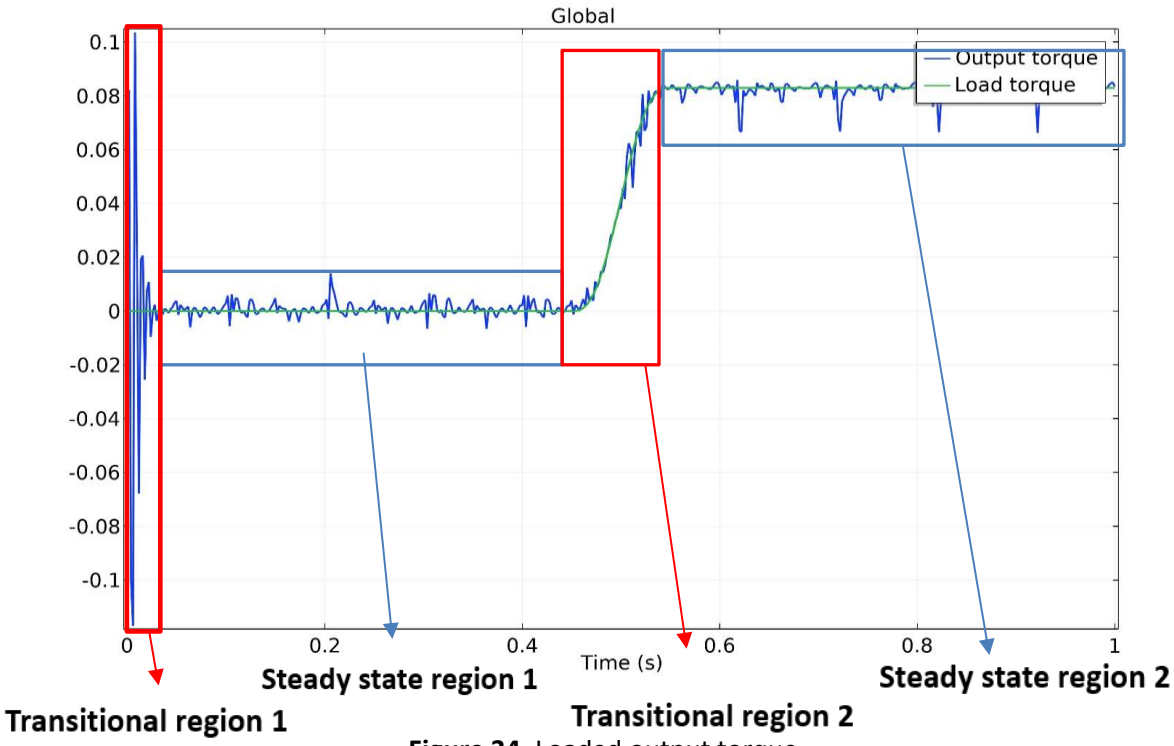

Figure 34. Loaded output torque

The electromagnetic torque in figure 33 exhibits two regions, the transient region during the start-up and the stationary region with a stability value of 0 (N.m), this is due to the fact that no load has been applied to the motor. The figure 34 can be divided in 4 regions, first, there is a transitional region during the start-up of the motor and when it reaches the stability, a step change in the load torque is applied at 0.5 seconds, this increment in the load can be consider as a transitional region between the two steady states zones, and the motor gradually generates the equal amount of torque that the step load itself, in this case 0.08 (N.m).

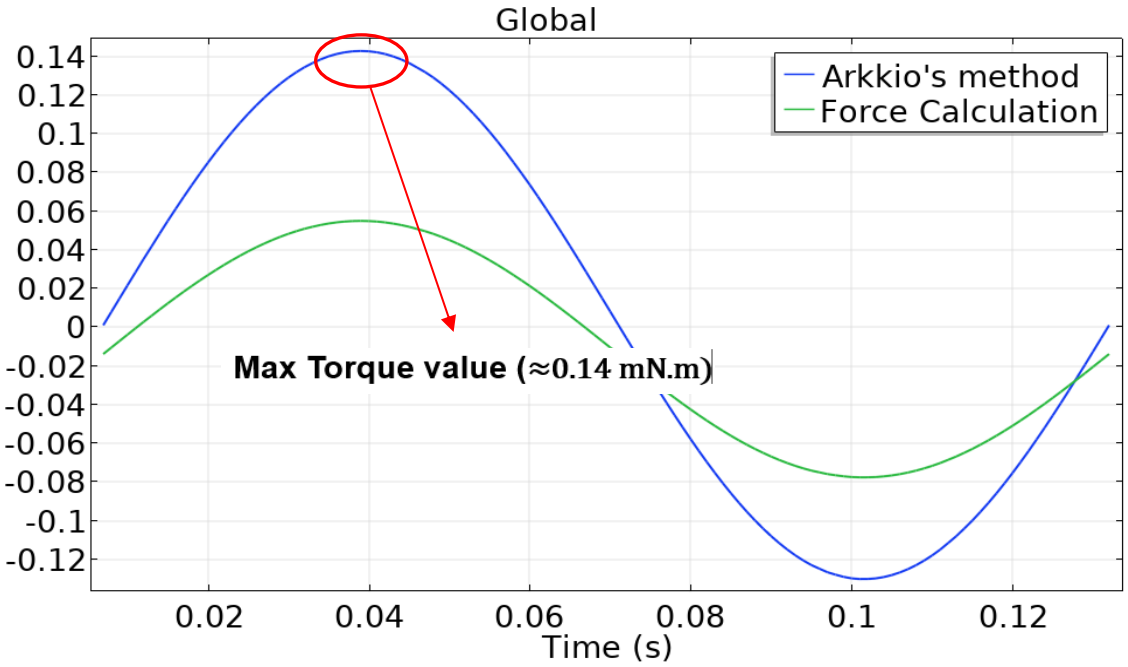

Figure 35 . 3D simulation. Output torque (Arkkio and force calculation methods) Time dependent

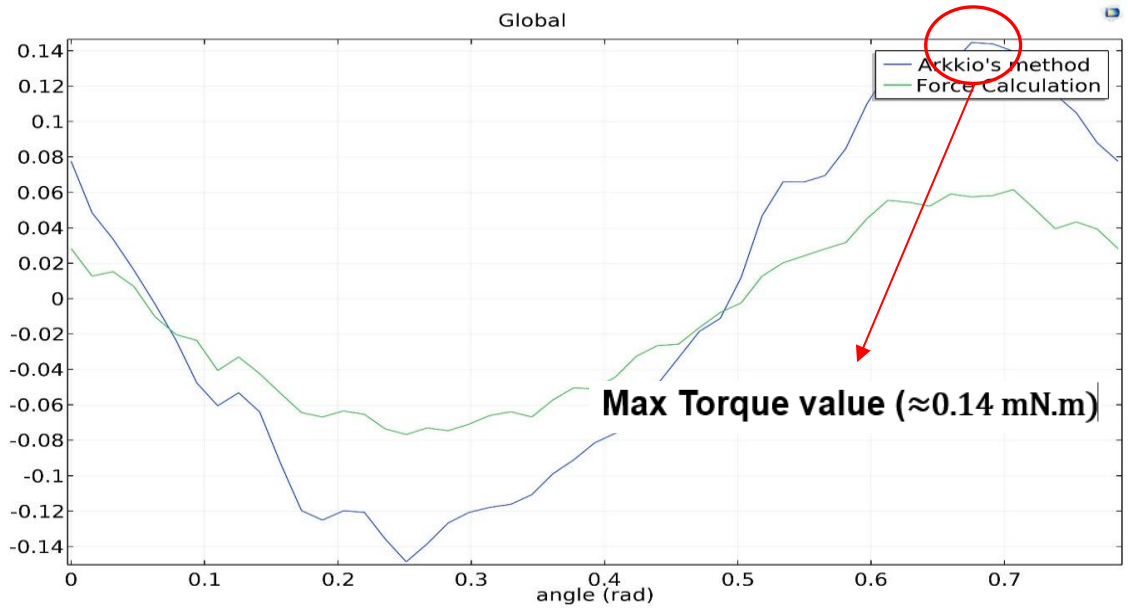

Figure 36. 3D simulation. Output torque (Arkkio and force calculation methods) Time dependent

The torque transmission in PMSM 3D modelled can actually be obtained by solving the stationary study for different angular positions. Varying the angular position is possible via the parametric sweep in the stationary study. However, for transient simulations, it would be needed to set up a time dependent study like the one in figure 35. Interestingly, we can obtain the identical torque transmission results from these two studies. The electromagnetic torque obtained in figure 35 was computed by (Bratke, 2018), and the second one have been computed as a verification of the first one, also looking for reduce computation time, computing a stationary study instead of a time-dependent study. Regardless of the study, we obtain the same sinusoidal behaviour with a maximum peak value of 0.14 (N.m).

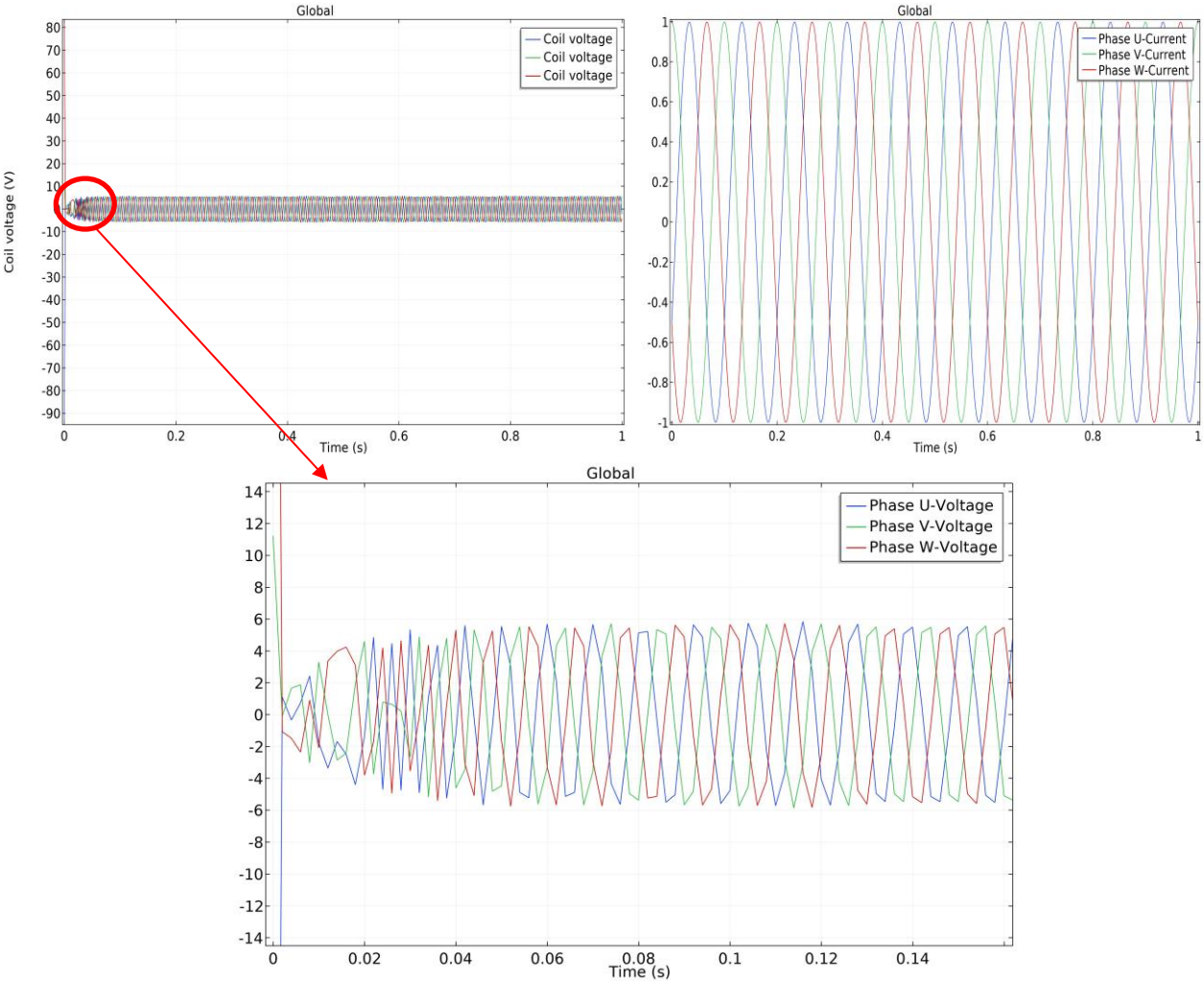

Figure 37. AC Voltage and current of the 2D motor simulation

With these pictures we can verify that the motor has been electromagnetically modelled correctly. It shows the results of alternating current and voltage. Unlike in the motor test, as explained at the beginning of the chapter, phase currents have been taken as input values instead of phase voltages. The alternating current reaches a peak value of 1 A and the corresponding voltage value is around 5 V, which are very similar values to those used in the measurement tests of the real motor prototype.

5.2 Thermal simulation

The thermal analysis was made through simulations with COMSOL Multiphysics software. The results of temperature distribution obtained analytically and by simulation will be compared as a verification method of the results. It is worth noting that both, the simulation method and the theoretical calculations are not completely independent from each other, because in order to perform the simulation it has previously been necessary to analytically calculate some fundamental factors to be implemented in the simulation such as convection coefficients (h) in the air gap and in the external environment. In the next chapter, a series of motor thermal simulations will be performed. These simulations will be divided into stationary regimen, which are the ones that participate in the objective of this thesis, for the correlation of the results with the analytical calculations; and transitory regime, which are more important for the future optimization and redesign of the motor prototype because in the reality the motor will operate for specific periods of time and not infinitely. Those of stationary regime will be divided as well in simulations of normal conditions (293.15 K, 1 atm), in cryogenic conditions of temperature (77 K, 1 atm), and in cryogenic conditions of temperature and vacuum pressure (77 K, 10^{-8}atm). The first, will take convection and heat conduction into account, but the radiation will be neglected and so, eliminated. In the last two, only radiation and conduction in the motor elements will be considered. The only difference between these two cryogenic conditions arising is that for the first one, the air will be taken into account as the environment therefore, the air gap between the rotor and the stator should be modelled. However, in vacuum conditions there will be no air gap between rotor and stator thus, there will be no heat conduction between these two elements into which the motor is divided. In any case, in both simulations at cryogenic temperatures, only the heat transfer by radiation will be taken into account, and the transfer by convection will be deleted. In addition, the distribution of temperatures will be organised according to the different components of the motor (winding, magnets, rotor, and whole sector). At the end of these simulations a table has been added in summary mode of the maximum temperatures reached for each simulation in a perfectly ordered way with the aim of compiling temperature data.
The simulations in transitory regime are more important for optimizing the real motor prototype because in the reality the operating time conditions will not be infinitely as in stationary regime. The structure organization of the simulations will be as in the stationary regime, but only two operating conditions are presented instead of three in this study: Normal temperature conditions (293.15 K, 1 atm), and cryogenic temperature conditions with vacuum pressure (77 K, 10^{-8}atm), where there will be no air gap between the stator and the rotor. In addition, the simulations are divided according to the components (winding, magnets, rotor, and whole sector), however, unlike in the stationary regime, we must add the temperature distributions for specific periods of time. It was decided to carry out the simulations for periods of t = (0.1,5,10,15,20,25, and 30) minutes.

The development of the simulation is not explained in detail because it can be read from (Bratke, 2018), however, a brief schematic explanation and description of the Model Builder Tree, with the parameters used, the selection of materials, the physical interfaces and the two studies computed (stationary and time-dependent) as well as the results obtained, are presented. Figure 127 shows Model Builder Tree of COMSOL Multiphysics, Figure 128 is the Selection and description of the

motor materials (winding, rotor-stator, magnets, air), and Figure129 the Convection heat transfer and stator heat source descriptions are presented.

Model Builder Tree of COMSOL Multiphysics

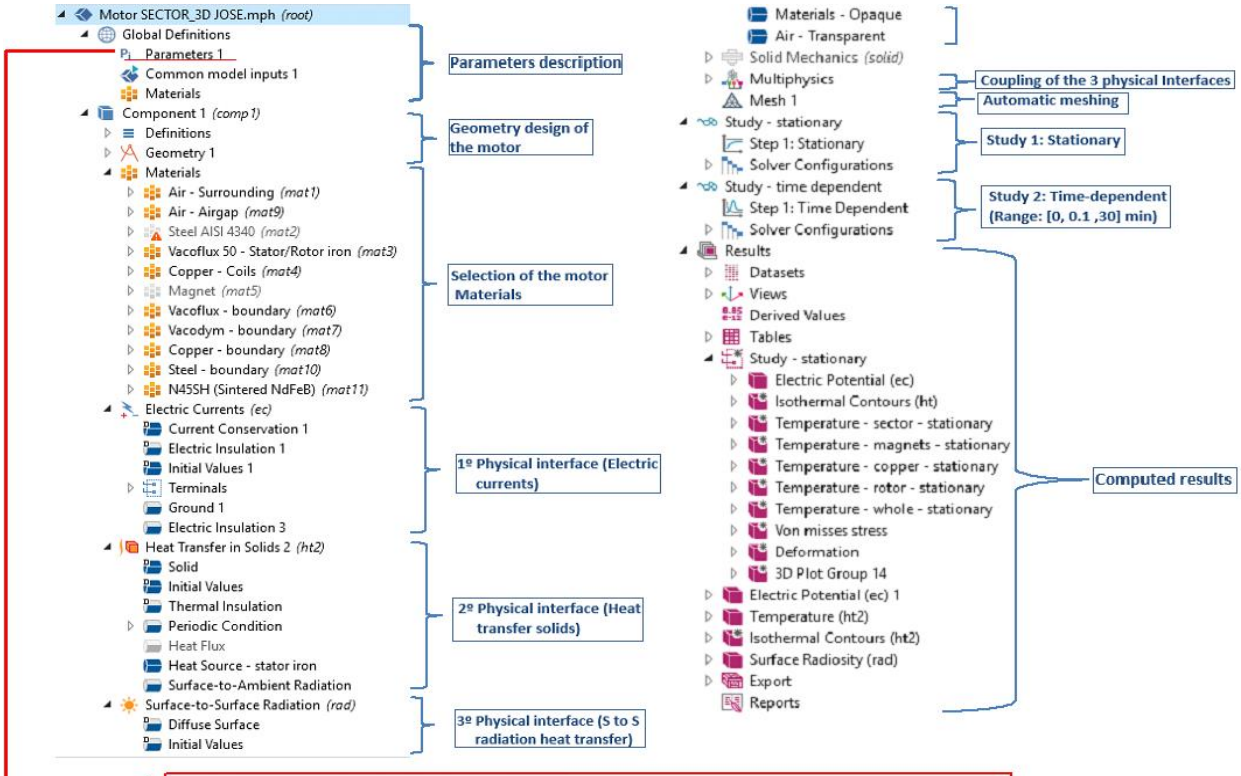

Parameters

Name	Expression	Value
r_shaft	10.8[mm]	0.0108 m
r_rotorFE	13.7[mm]	0.0137 m
r_PM	20.7[mm]	0.0207 m
r_delta_1	20.95[mm]	0.02095 m
r_delta_2	21.2[mm]	0.0212 m
r_winding_1	21.8[mm]	0.0218 m
r_winding_2	22.4[mm]	0.0224 m
r_statorFE	29[mm]	0.029 m
r_outerAir	30[mm]	0.03 m
p	8	8
N	192	192
q	N/(2*p*m)	4
m	3	3
L	37[mm]/2	0.0185 m
L_air	5[mm]	0.005 m
tau_PM	0.8	0.8
delta_mod	360/p	45
delta_PM	delta_mod*tau_PM/2	18
delta_airPM	delta_mod*(1-tau_PM)/2	4.5
delta_win...	360/N	1.875
d_coil	0.5[mm]	5E-4 m
I_N	0.5294[A]	0.5294 A
a_coil	pi*(d_coil/2)^2	1.9635E-7 m²
M	1.6[T]	1.6 T
f	8[1/s]	8 1/s
rpm	1[1/s]	1 1/s
omega	2*pi*f	50.265 1/s
t	0[s]	0 s
air_gap	0.5[mm]	5E-4 m
phi0	0	0
meshsize	3.5e-4	3.5E-4
i_U	I_eff	0.37434 A
i_V	I_eff	0.37434 A
i_W	I_eff	0.37434 A

I	0.5294[A]	0.5294 A
I_eff	I/sqrt(2)	0.37434 A
rho_Vaco_...	8.12[g/cm^3]	8120 kg/m³
k_iso_Vac...	30[W/(m*K)]	30 W/(m·K)
CP_iron	0.444[J/(g*degC)]	444 J/(kg·K)
rho_Vaco...	7.6[g/cm^3]	7600 kg/m³
k_iso_Vac...	10[W/(m*K)]	10 W/(m·K)
CP_Vacod...	450[J/(kg*K)]	450 J/(kg·K)
h_air	2.9[W/(m^2*K)]	2.9 W/(m²·K)
T_initial	77[K]	77 K
T_amb	77[K]	77 K
P_loss_sta...	0.047[W]*(1/(p*2))	0.0029375 W
velocity	0.5[km/h]	0.13889 m/s
Pressure	10^-8[bar]	0.001 Pa

Figure 127: Model Builder Tree of COMSOL Multiphysics

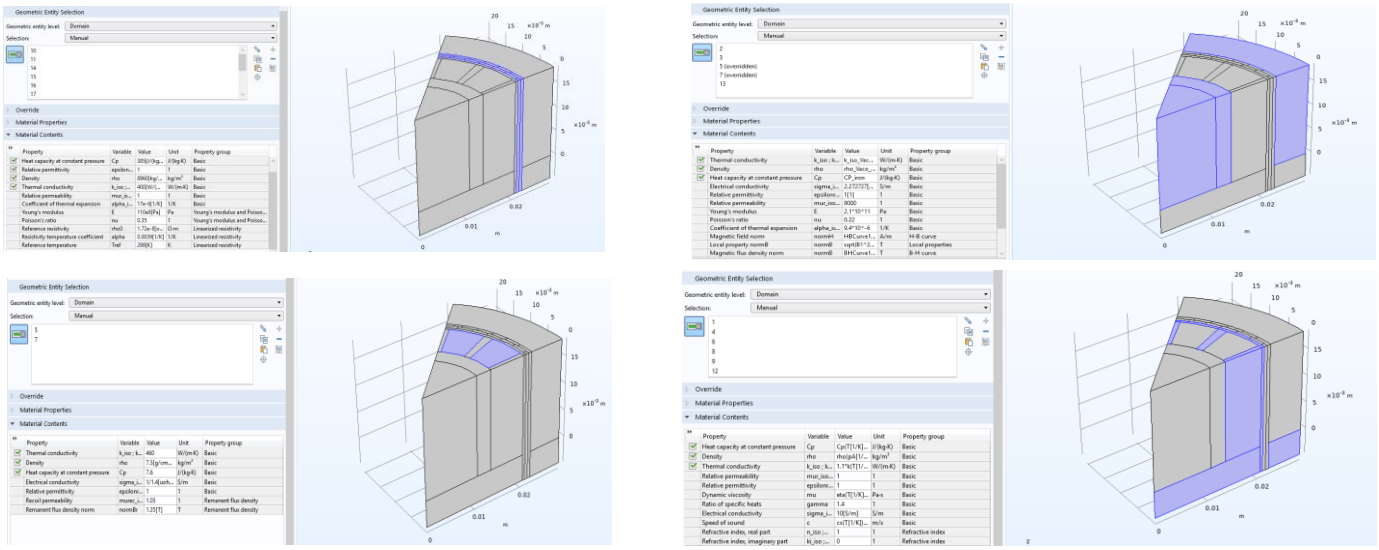

Figure 128: Selection and description of the motor materials (winding, rotor-stator, magnets, air).

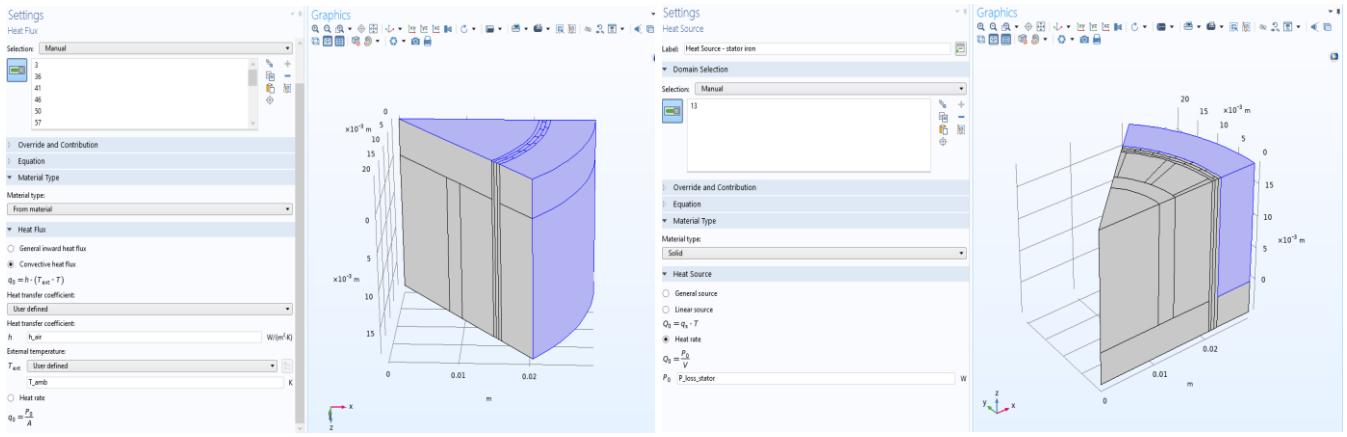

Figure 129: Convection heat transfer and stator heat source descriptions

The following Figures 38 and 39 show the meshing of the motor, necessary for computing the simulation, and the winding selection as one of the two heat sources due to the Joule effect provoked by the electric current.

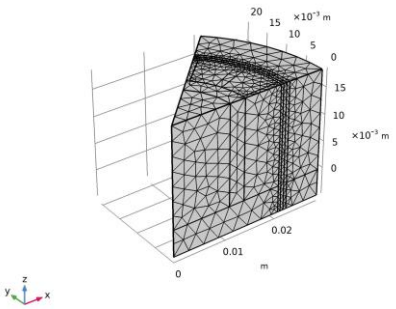

Figure 38. Mesh model

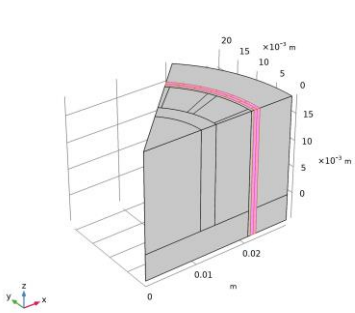

Figure 39. Winding heat source

5.2.1 Stationary thermal simulations

5.2.1.1 Temperature distribution at normal conditions

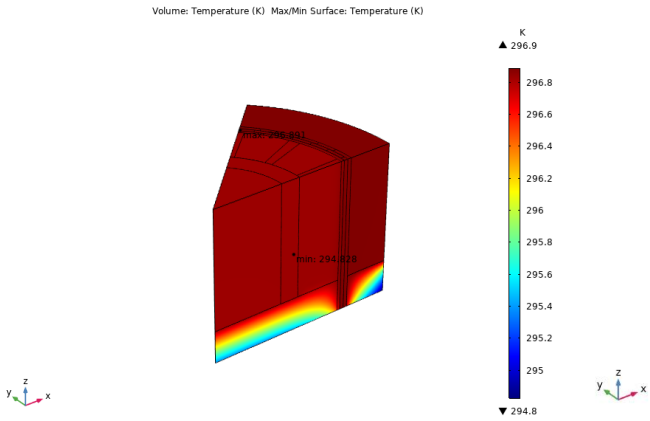

Figure 40. Temperature distribution. Motor sector

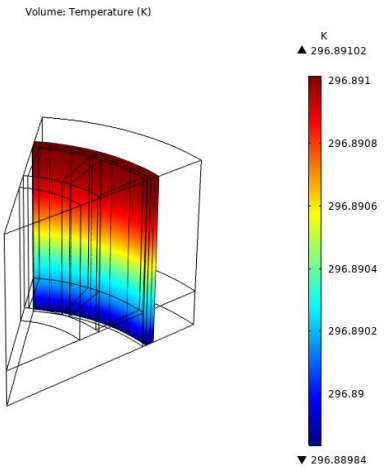

Figure 41. Temperature distribution. Winding

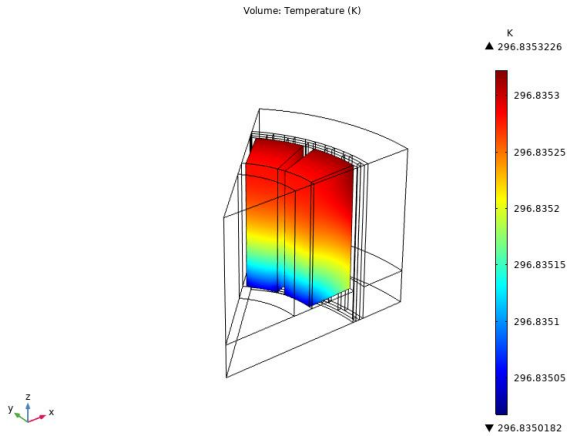

Figure 42. Temperature distribution. Magnets

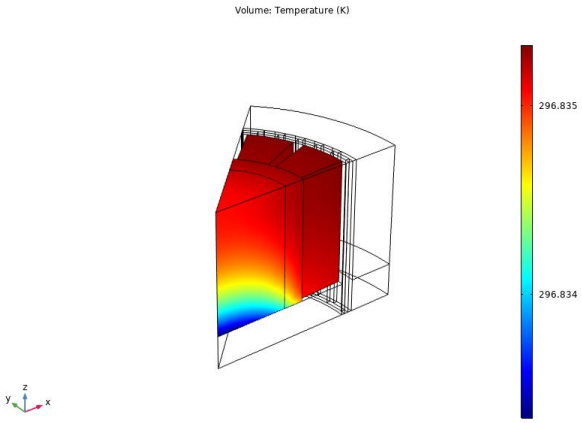

Figure 43. Temperature distribution. Rotor

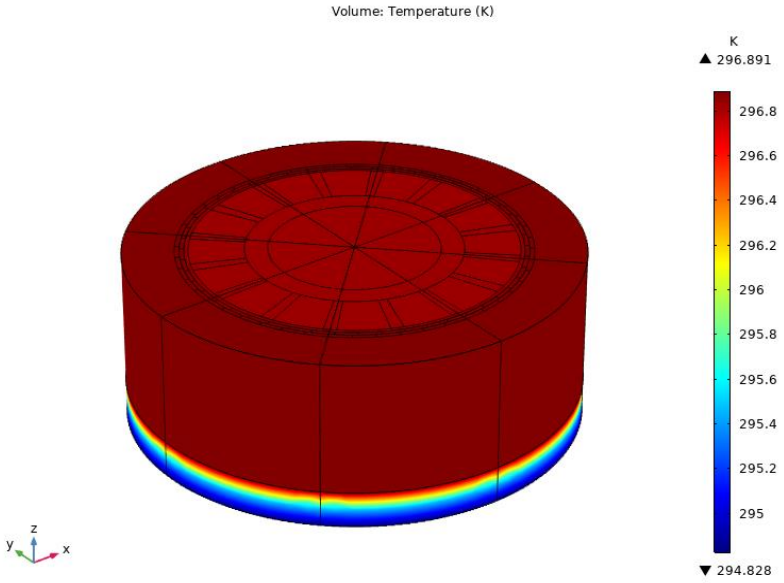

Figure 44. Temperature distribution. Whole model (normal conditions)-Stationary-

5.2.1.2 Temperature distribution at cryogenic conditions with air gap

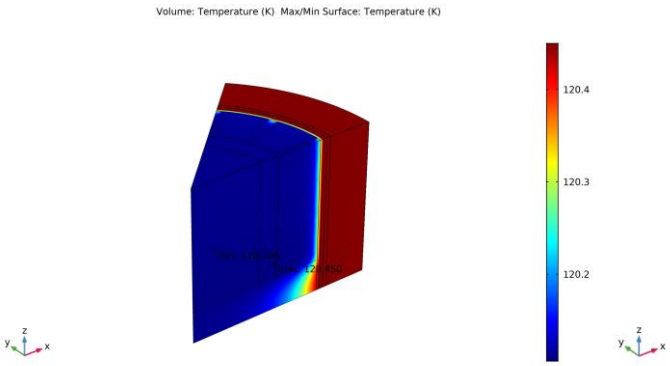

Figure 45. Temperature distribution. Motor sector

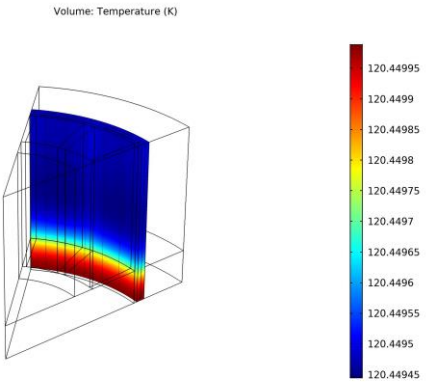

Figure 46. Temperature distribution. Winding

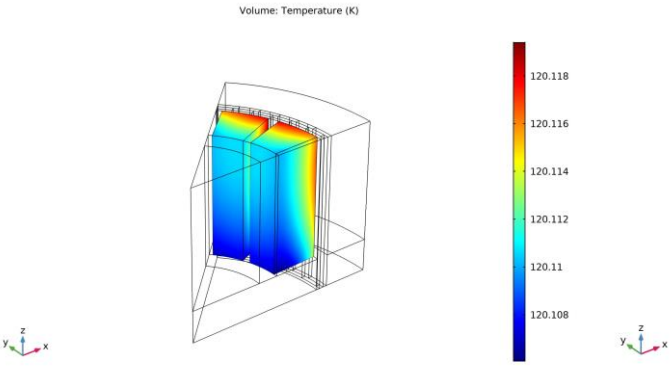

Figure 47. Temperature distribution. Magnets

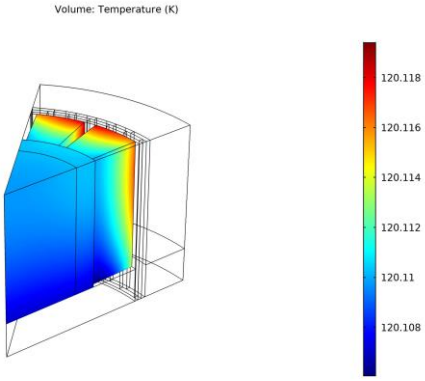

Figure 48. Temperature distribution. Rotor

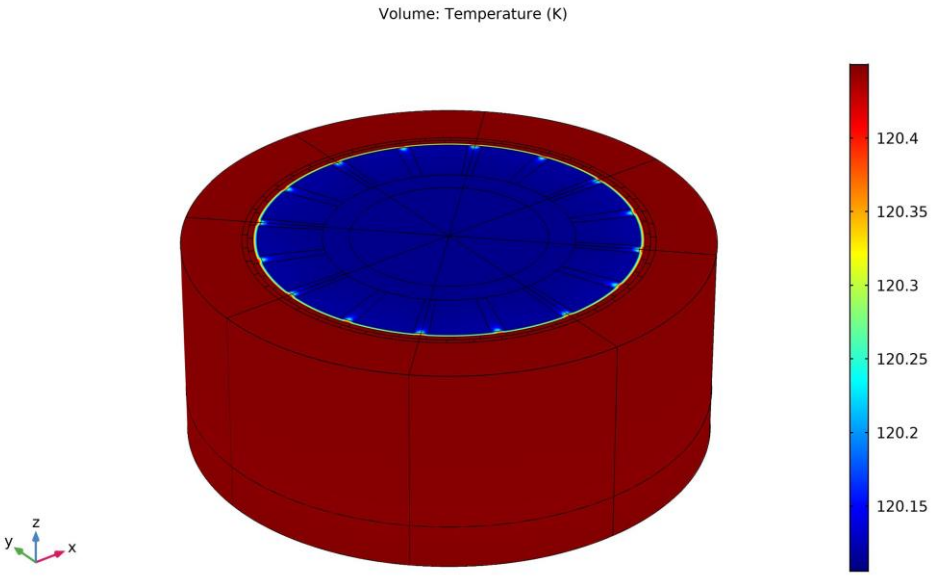

Figure 49. Temperature distribution. Whole model (cryogenic conditions with air gap) -stationary-

5.2.1.3 Temperature distribution at cryogenic conditions with vacuum gap

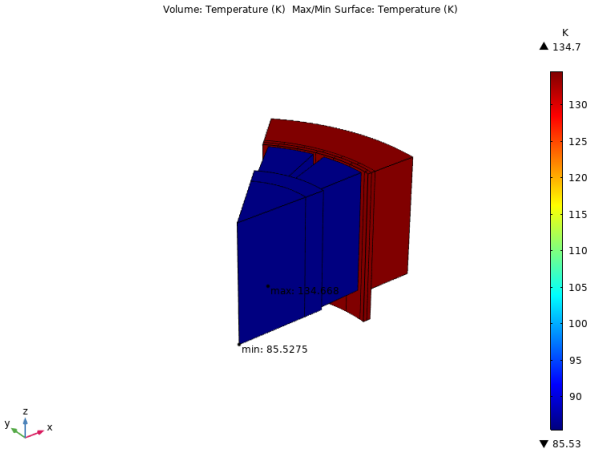

Figure 50. Temperature distribution. Motor sector

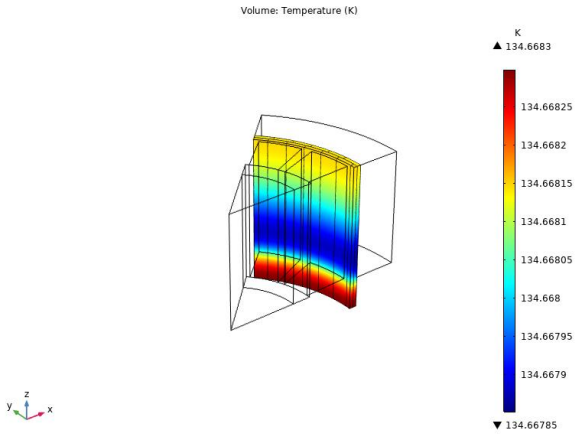

Figure 51. Temperature distribution. Winding

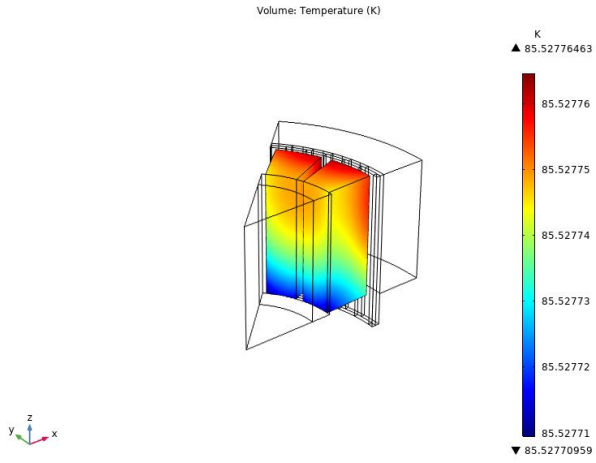

Figure 52. Temperature distribution. Magnets

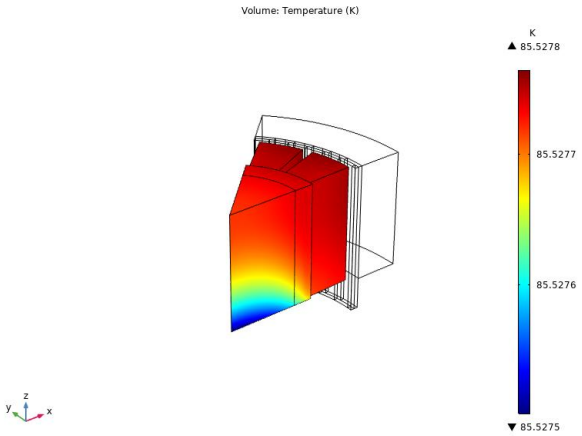

Figure 53. Temperature distribution. Rotor

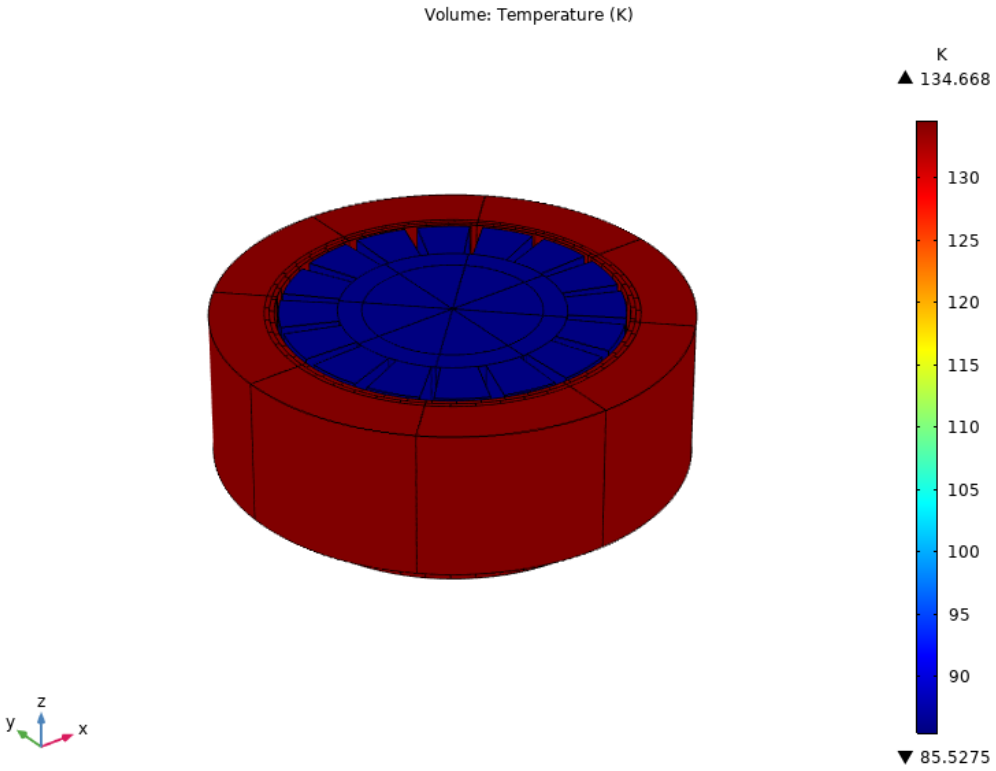

Figure 54. Temperature distribution. Whole model (cryogenic conditions without air gap) -stationary-

Table 5.1: Resume of maximum temperatures in the stationary studies

Ambient conditions	Motor component	Maximum Temperature (K)
Normal ambient conditions (293.15 K)	**Whole motor**	296.9
	Rotor	296.89102
	Magnets	296.8353
	Winding	296.8353
Cryogenic ambient conditions with air gap (77K)	**Whole motor**	120.45
	Rotor	120.4495
	Magnets	120.118
	Winding	120.118
Cryogenic ambient conditions without air gap (77K)	**Whole motor**	134.668
	Rotor	134.6683
	Magnets	85.5277
	Winding	85.5777

The maximum temperature reached by the motor under normal operating conditions is 296.9 K, therefore it increases 3.75 K from its initial ambient temperature. The maximum temperature reached by the motor under cryogenic operating conditions with air gap is 120.45 K, therefore it increases 43.45 K. And the maximum temperature reached by the motor under cryogenic operating conditions without air gap is 134.668 K, therefore it increases 57.668 K from its initial temperature. These results are necessary to perform the correlation with the calculations, but in order to determine the true increase in motor temperature, it is necessary to perform the transient simulations.

5.2.2 Transitionary thermal simulations

5.2.2.1 Temperature distribution at normal conditions

5.2.2.1.1 Sector

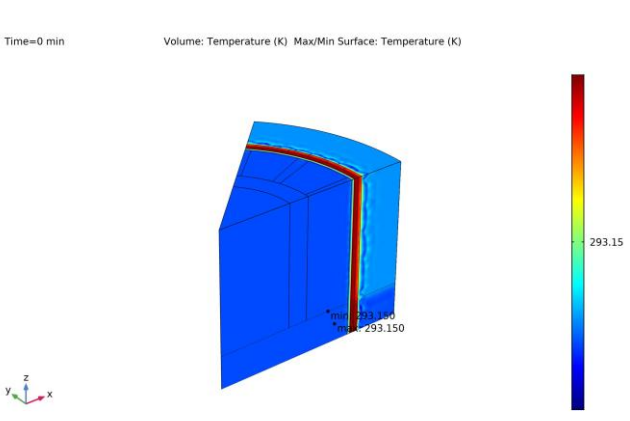

Figure 55. Temperature distribution. Sector (t=0 min)

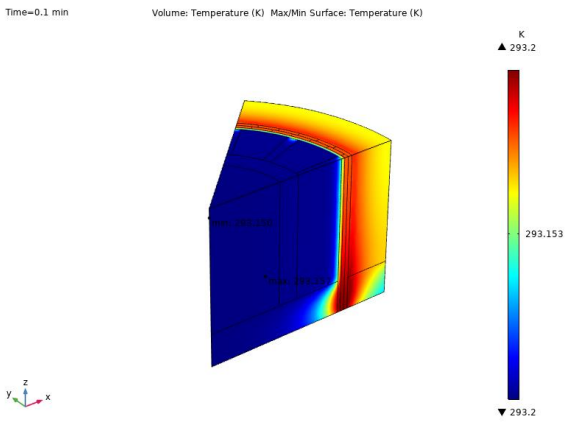

Figure 56. Temperature distribution. Sector (t=0.1 min)

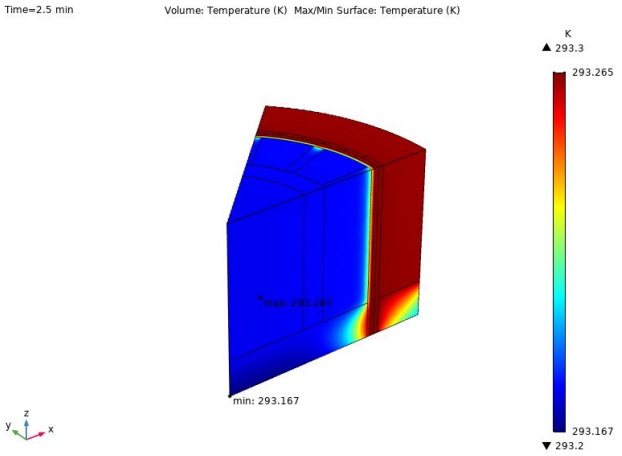

Figure 57. Temperature distribution. Sector (t=2.5 min)

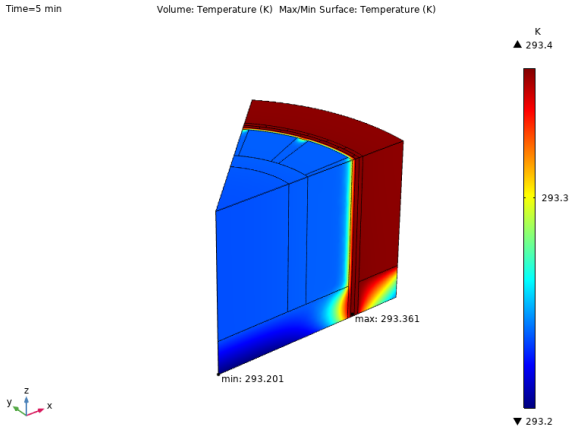

Figure 58. Temperature distribution. Sector (t=5 min)

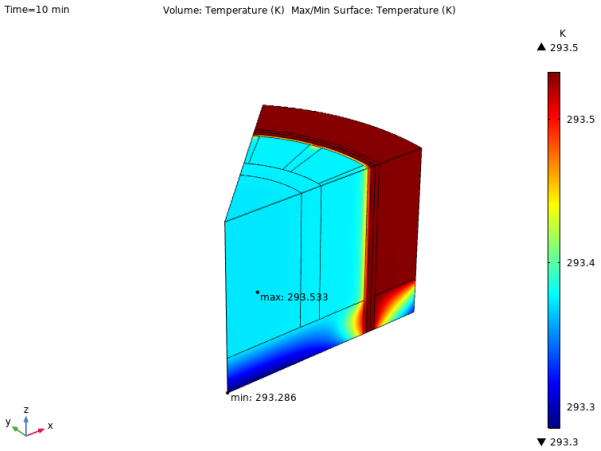

Figure 59. Temperature distribution. Sector (t=10 min)

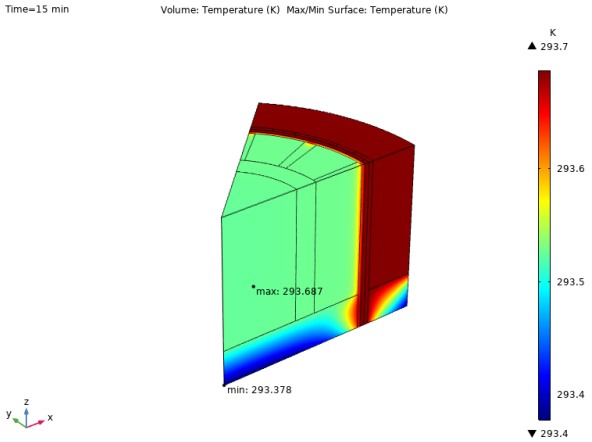

Figure 60. Temperature distribution sector (t=15 min)

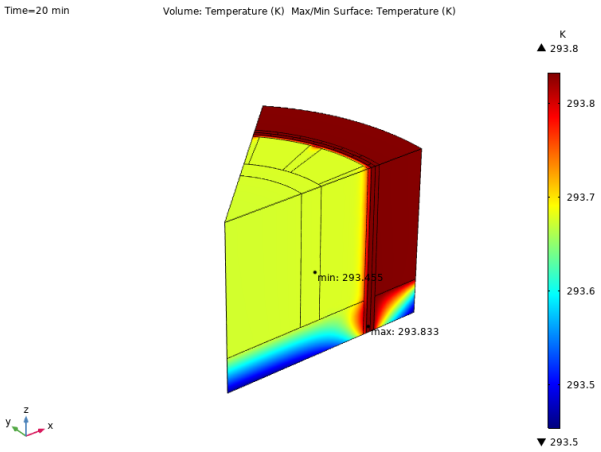

Figure 61. Temperature distribution.Sector (t=20 min)

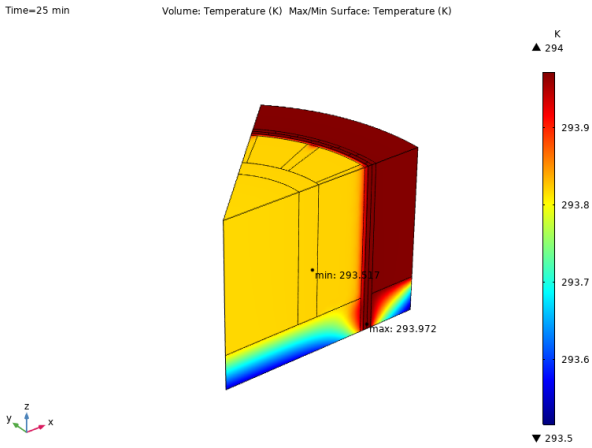

Figure 62. Temperature distribution. Sector (t=25 min)

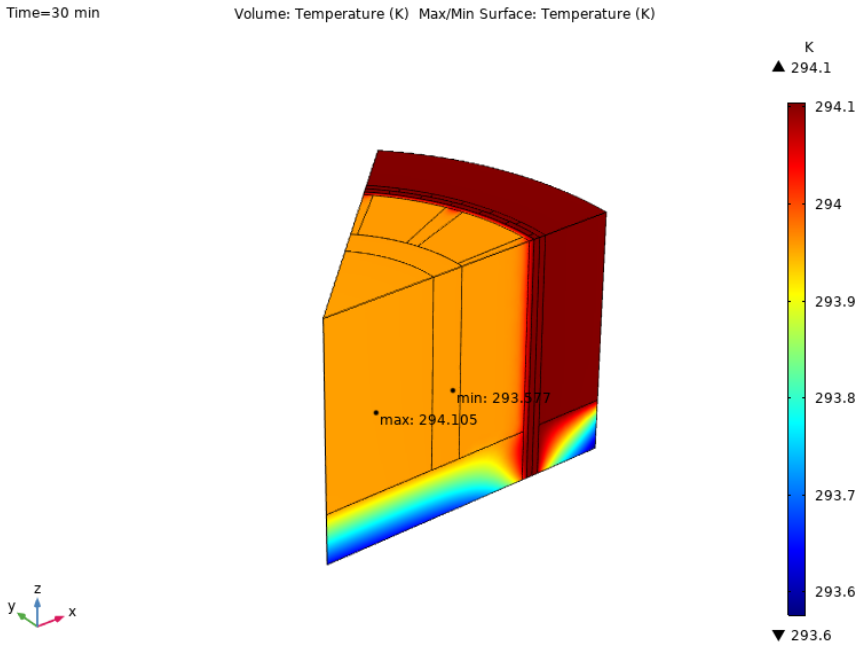

Figure 63. Temperature distribution. Sector (t=30 min)

5.2.2.1.2 Winding

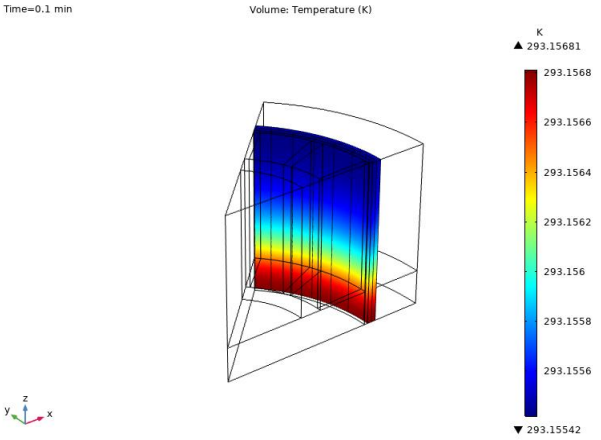

Figure 64. T(K) distribution. Winding (t=0.1 min)

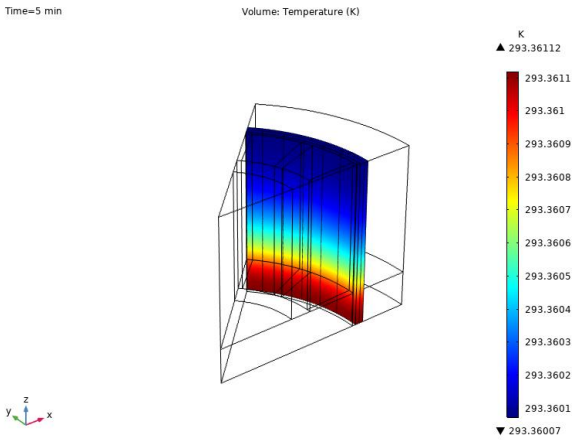

Figure 65. T(K) distribution.Winding (t=5 min)

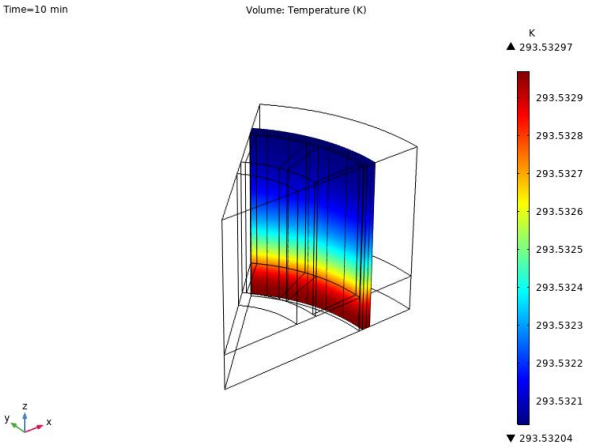

Figure 66. T(K) distribution. Winding (t=10 min)

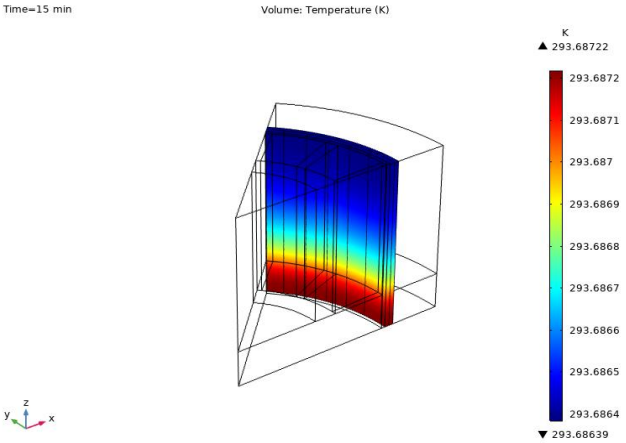

Figure 67. T(K) distribution. Winding (t=15 min)

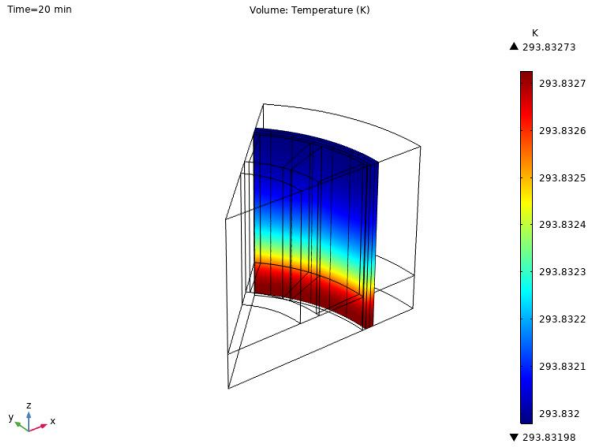

Figure 68. T(K) distribution. Winding (t=20 min)

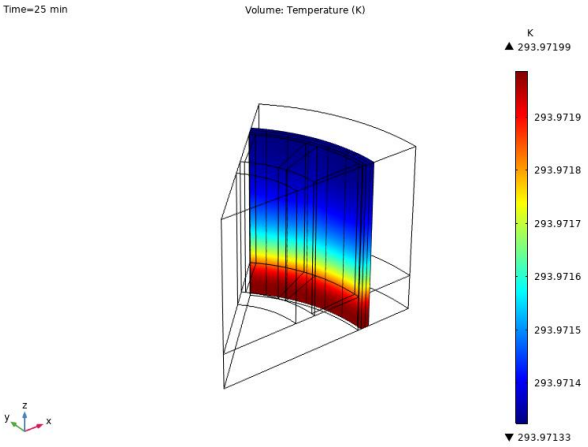

Figure 69. T(K) distribution. Winding (t=25 min)

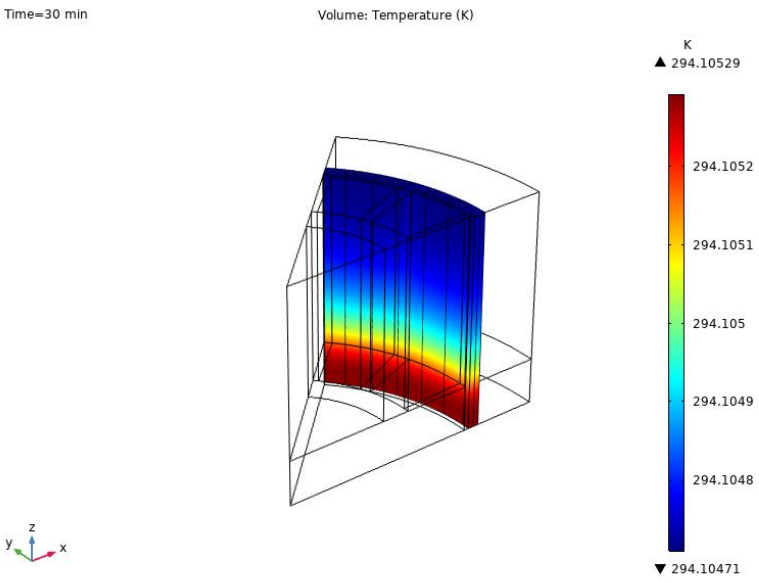

Figure 70. T(K) distribution. Winding (t=30 min)

5.2.2.1.3 Magnets

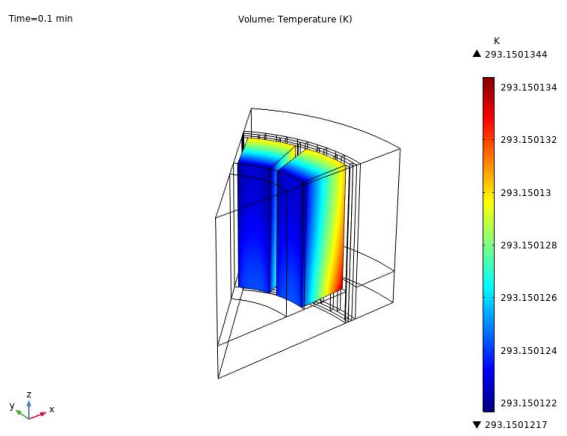

Figure 71. T(K) distribution. Magnets (t=0.1 min)

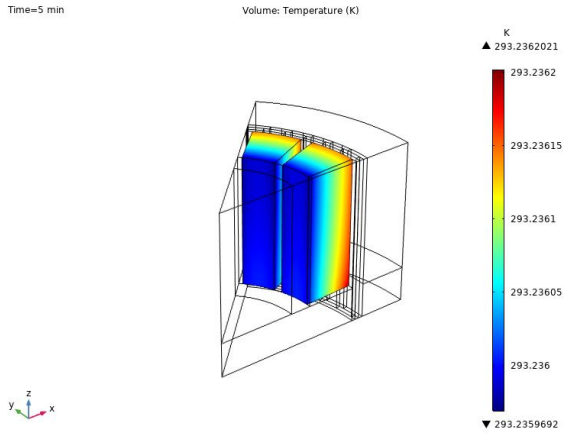

Figure 72. T(K) distribution. Magnets (t=5 min)

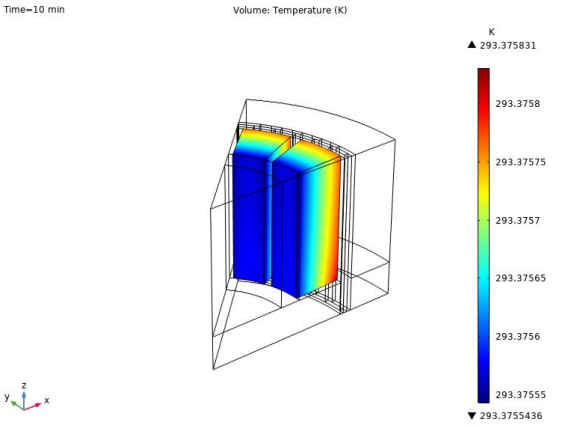

Figure 73. T(K) distribution. Magnets (t=10 min)

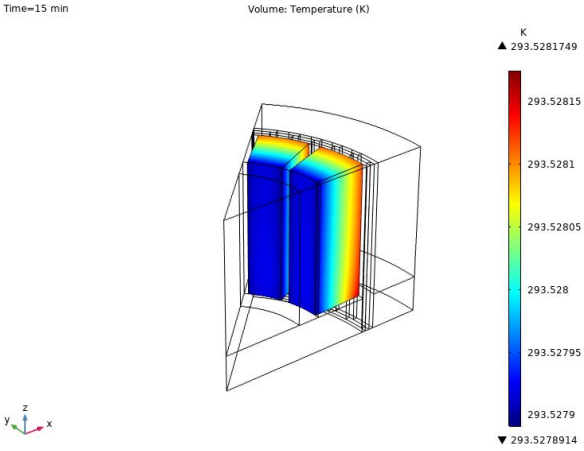

Figure 74. T(K) distribution. Magnets (t=15 min)

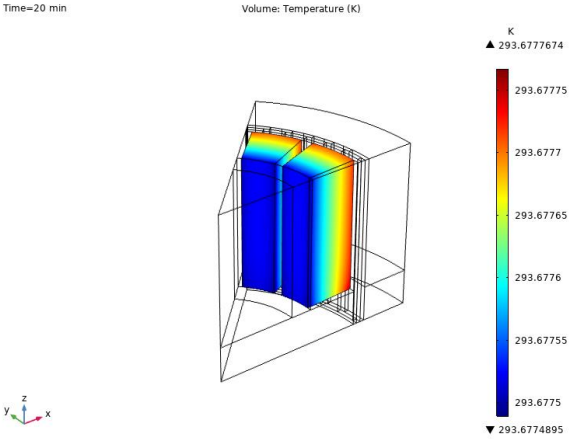

Figure 75. T(K) distribution. Magnets (t=20 min)

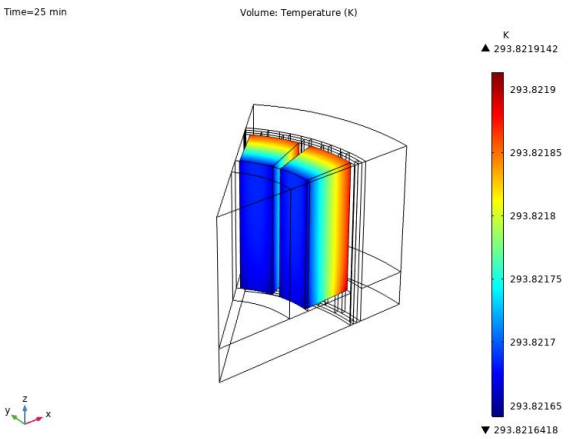

Figure 76. T(K) distribution. Magnets (t=25 min)

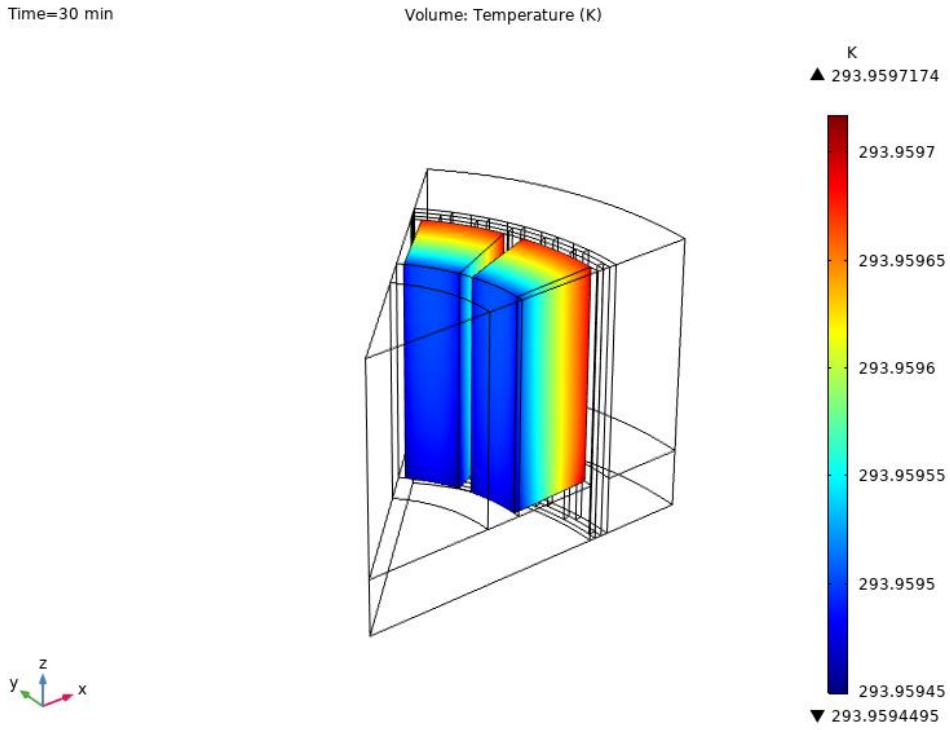

Figure 77. T(K) distribution. Magnets (t=30 min)

5.2.2.1.4 Rotor

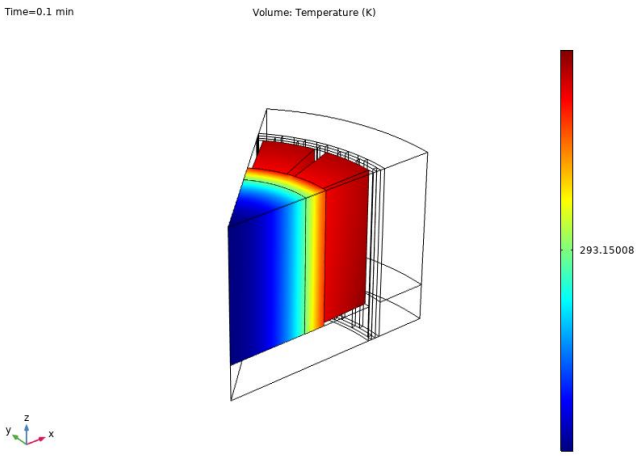

Figure 78. T(K) distribution. Rotor (t=0.1 min)

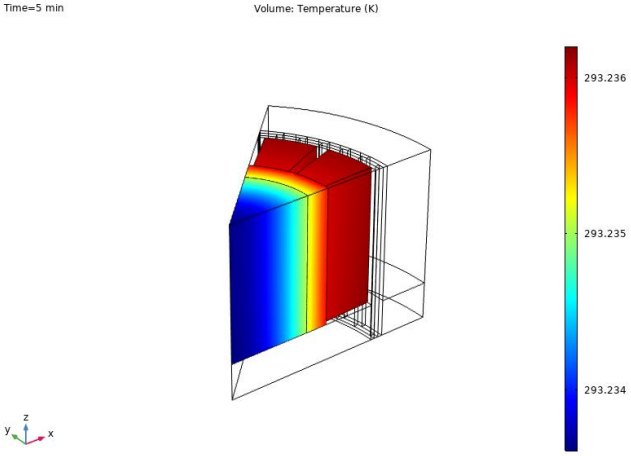

Figure 79. T(K) distribution. Rotor (t=5 min)

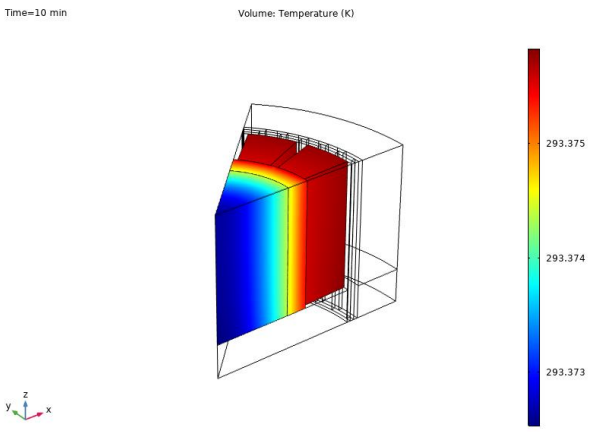

Figure 80. T(K) distribution. Rotor (t=10 min)

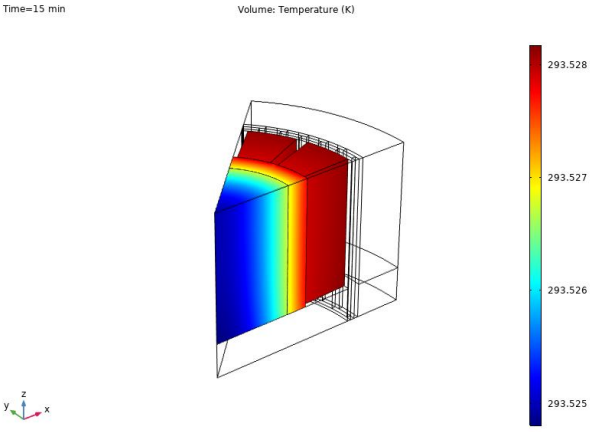

Figure 81. T(K) distribution. Rotor (t=15 min)

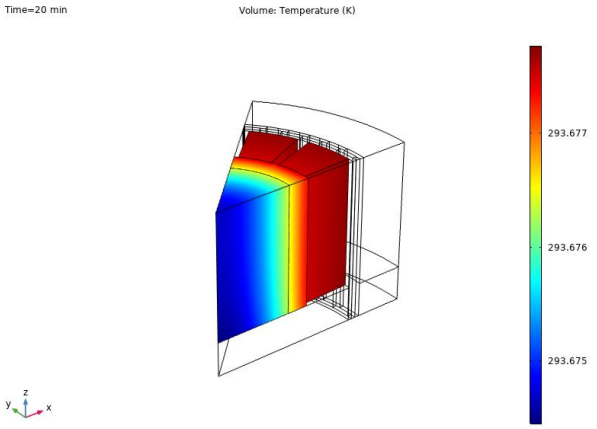

Figure 82. T(K) distribution. Rotor (t=20 min)

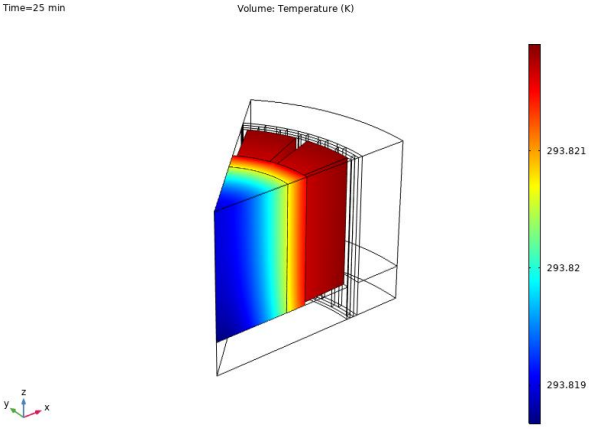

Figure 83. T(K) distribution. Rotor (t=25 min)

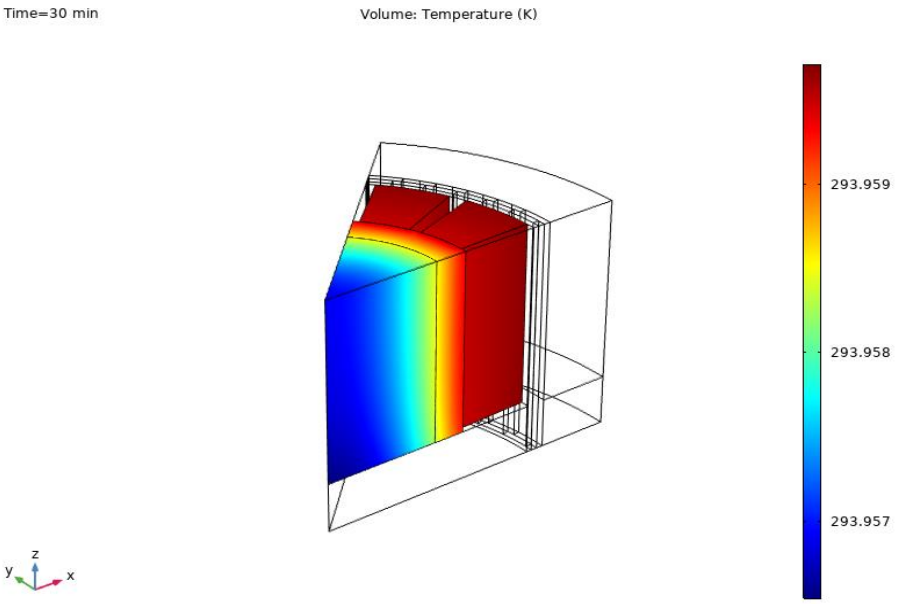

Figure 84. T(K) distribution. Rotor (t=30 min)

5.2.2.2 Temperature distribution at cryogenic conditions with vacuum gap

5.2.2.2.1 Sector

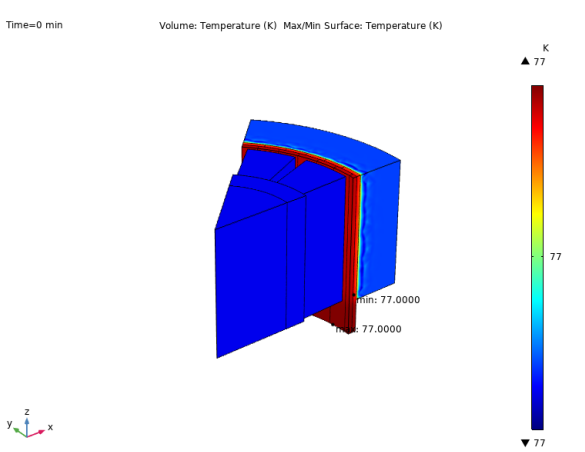

Figure 85. T(K) distribution. Sector (t=0 min)

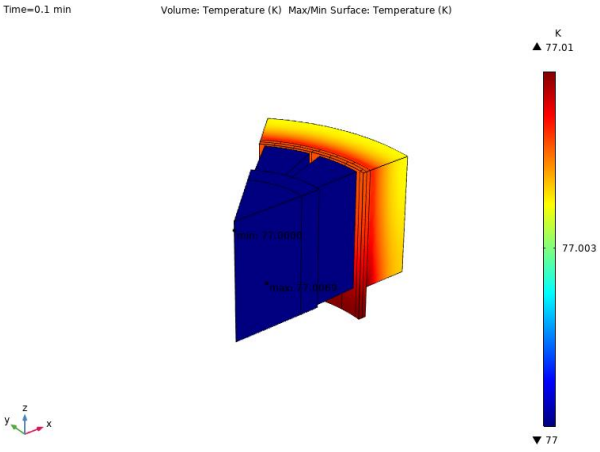

Figure 86. T(K) distribution. Sector (t=0.1 min)

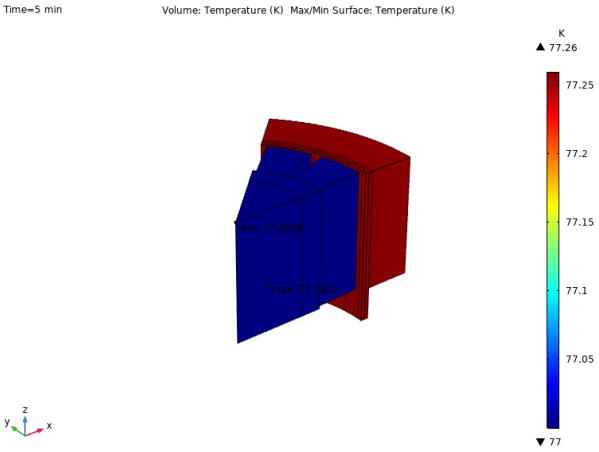

Figure 87. T(K) distribution. Sector (t=5 min)

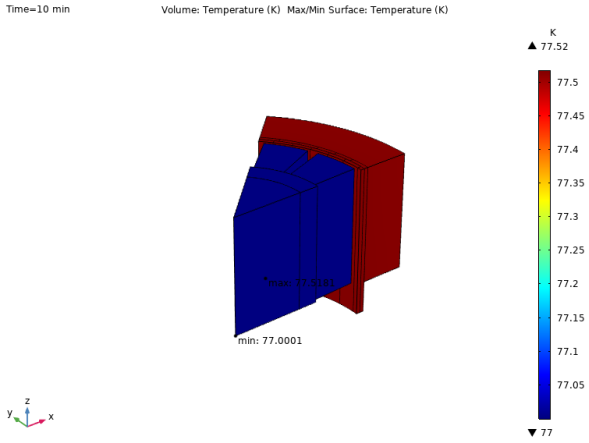

Figure 88. T(K) distribution. Sector (t=10 min)

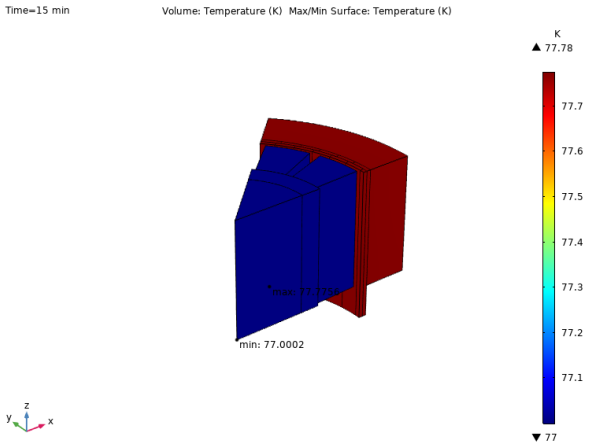

Figure 89. T(K) distribution. Sector (t=15 min)

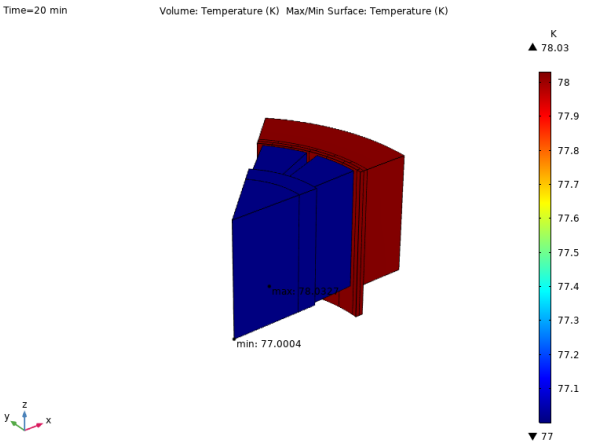

Figure 90. T(K) distribution. Sector (t=20 min)

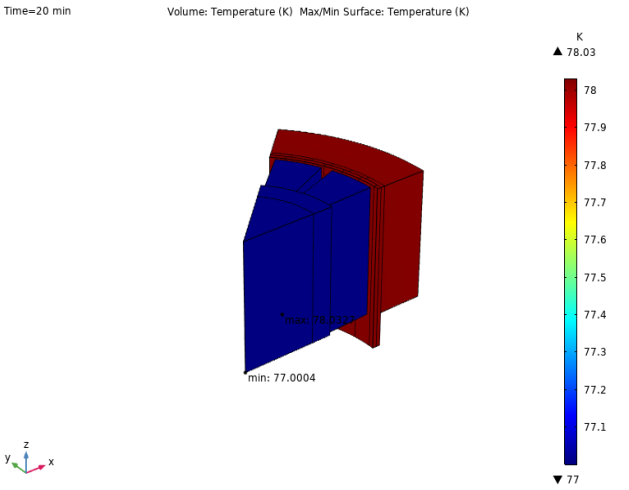

Figure 91. T(K) distribution. Sector (t=20 min)

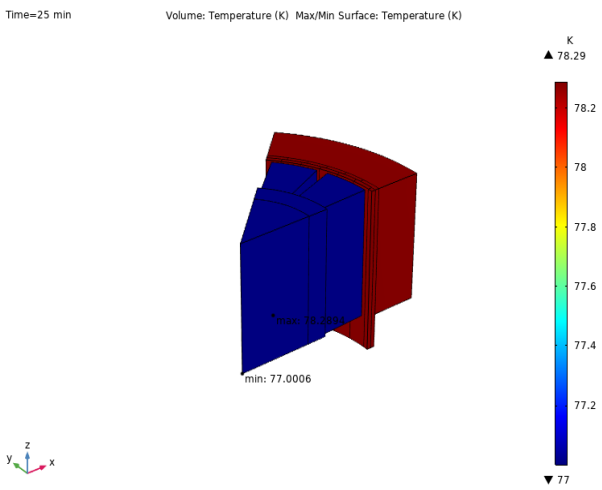

Figure 92. T(K) distribution. Sector (t=25 min)

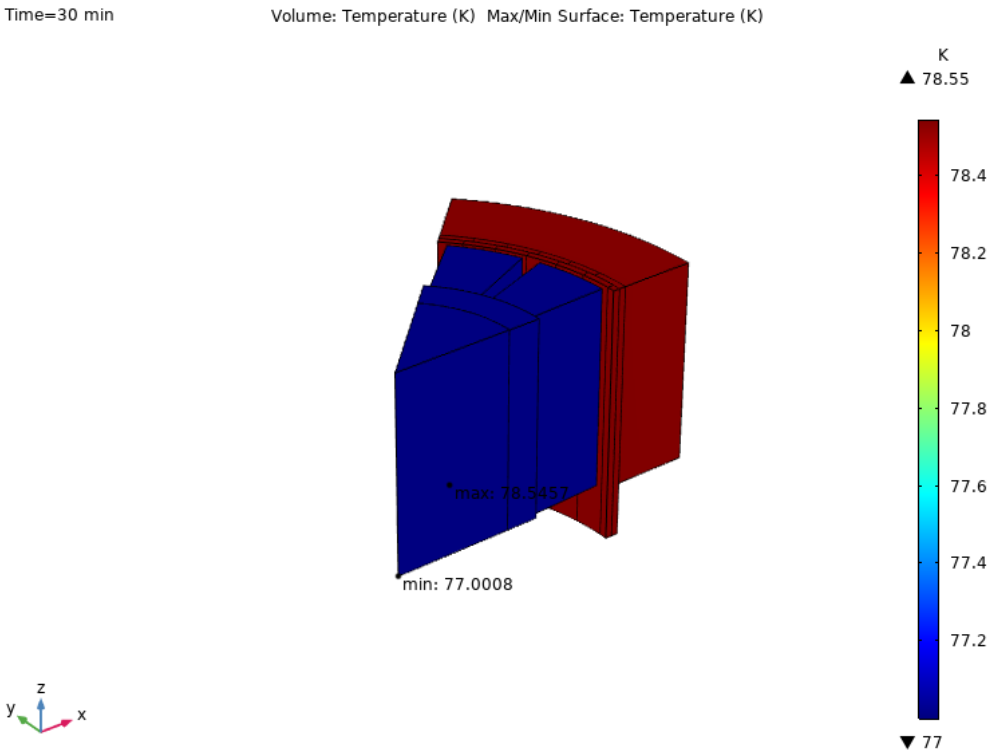

Figure 93. T(K) distribution. Rotor (t=30 min)

5.2.2.2.2 Winding

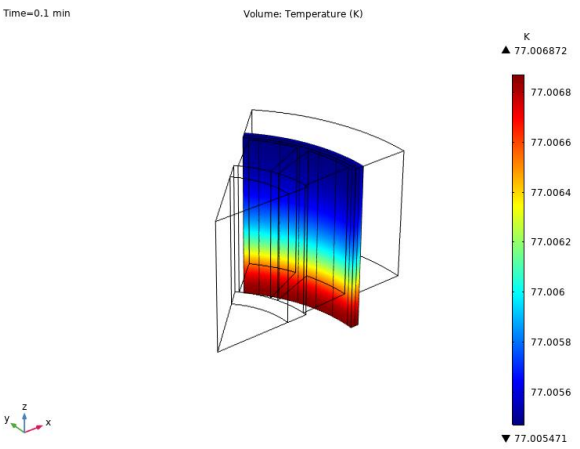

Figure 94. T(K) distribution. Winding (t=0.1 min)

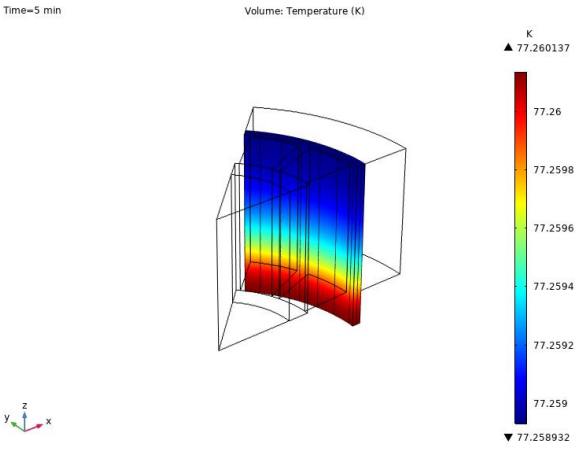

Figure 95. T(K) distribution. Winding (t=5 min)

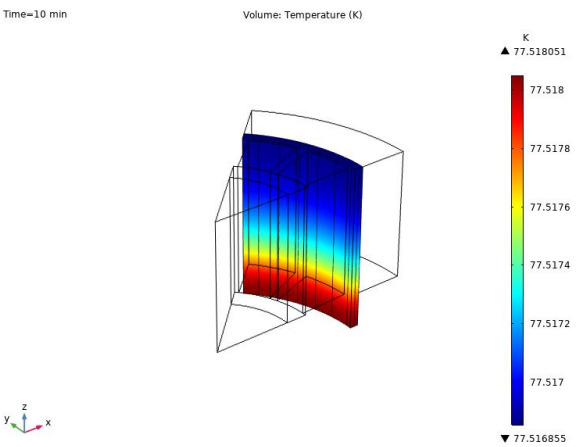

Figure 96. T(K) distribution. Winding (t=10 min)

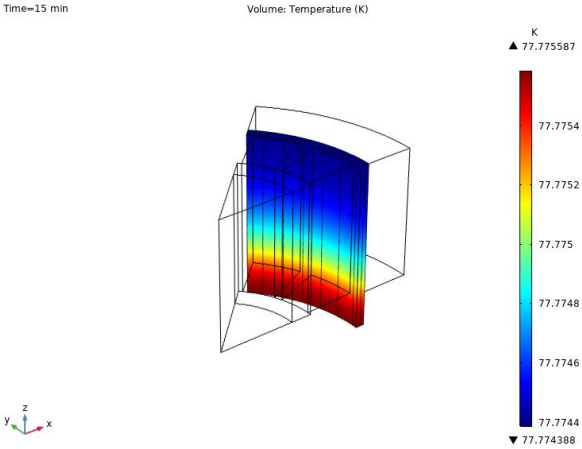

Figure 97. T(K) distribution. Winding (t=15 min)

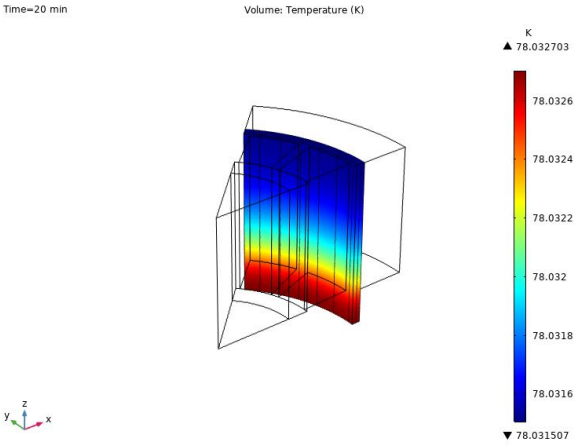

Figure 98. T(K) distribution. Winding (t=20 min)

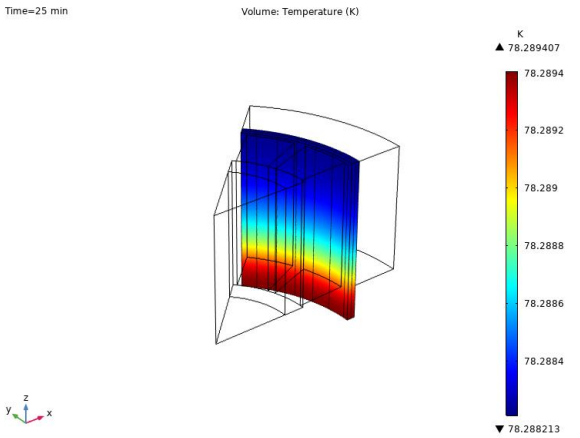

Figure 99. T(K) distribution. Winding (t=25 min)

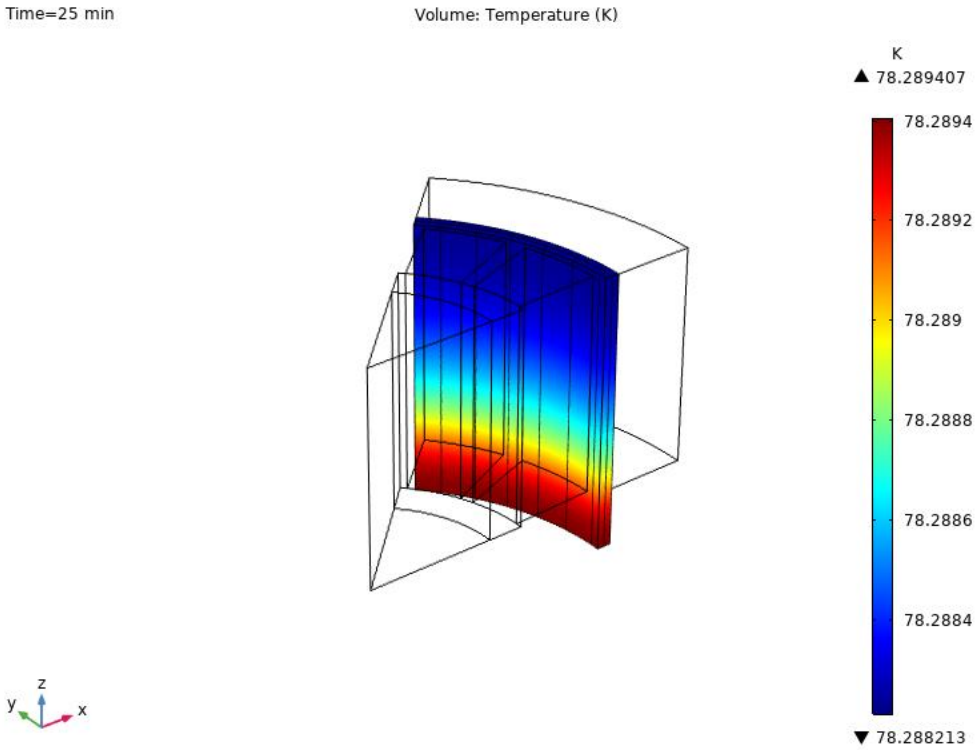

Figure 100. T(K) distribution. Winding (t=30 min)

5.2.2.2.3 Magnets

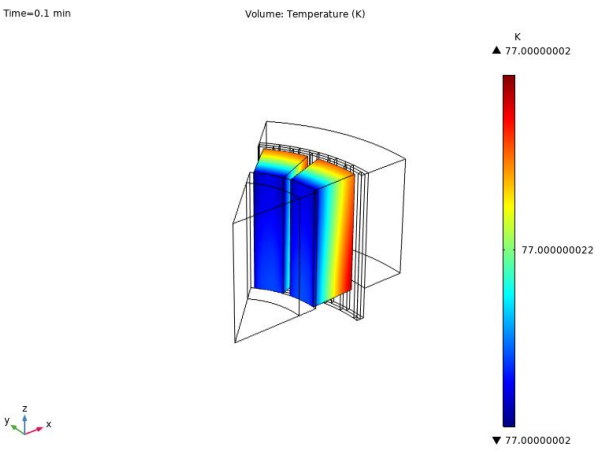

Figure 101. T(K) distribution. Magnets (t=0.1 min)

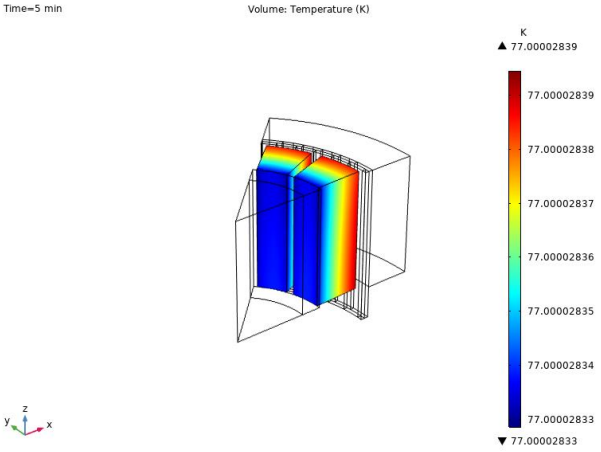

Figure 102. T(K) distribution. Magnets (t=5 min)

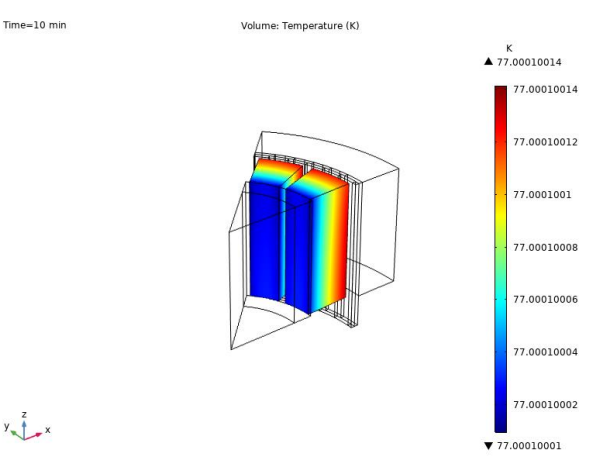

Figure 103. T(K) distribution. Magnets (t=10 min)

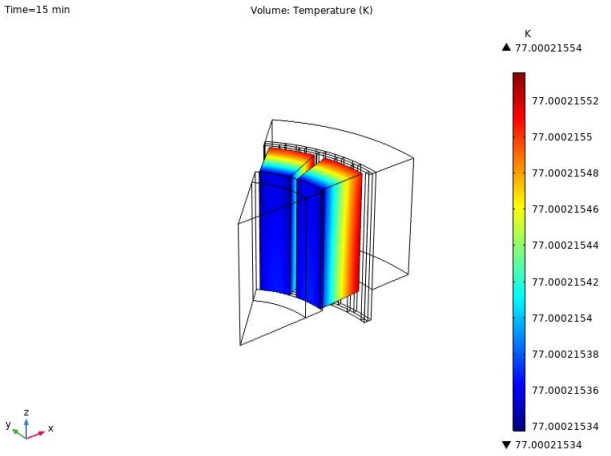

Figure 104. T(K) distribution. Magnets (t=15 min)

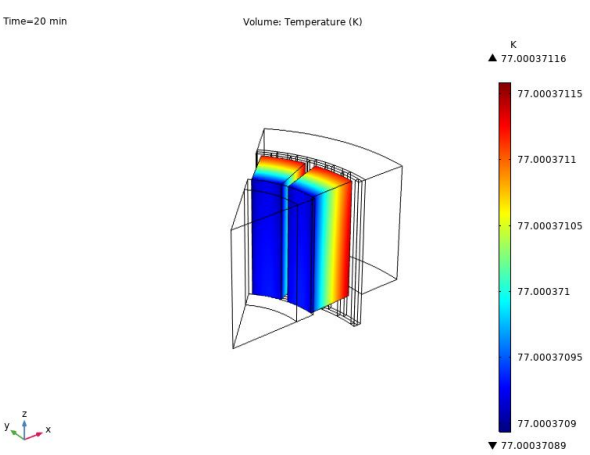

Figure 105. T(K) distribution. Magnets (t=20 min)

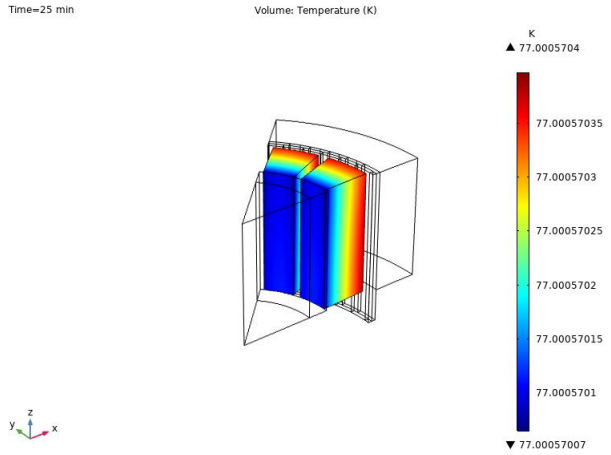

Figure 106. T(K) distribution. Magnets (t=25 min)

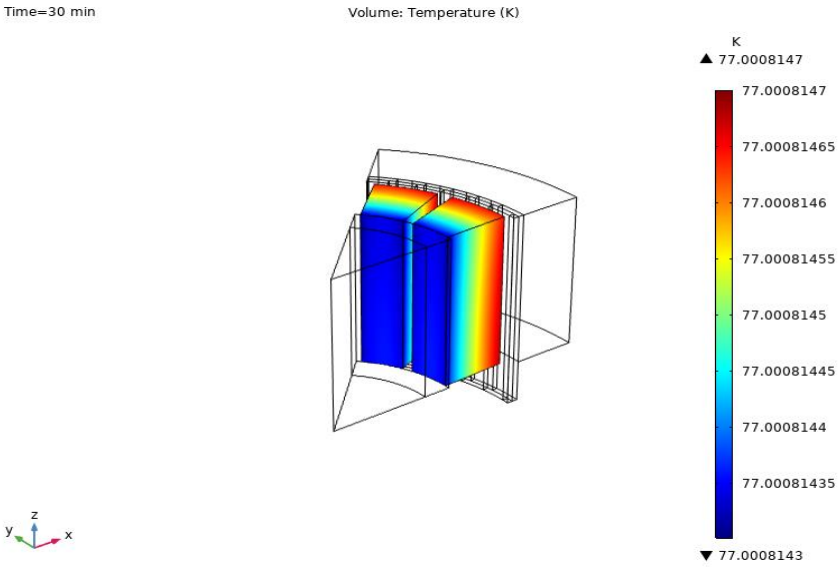

Figure 107. T(K) distribution. Magnets (t=30 min)

5.2.2.2.4 Rotor

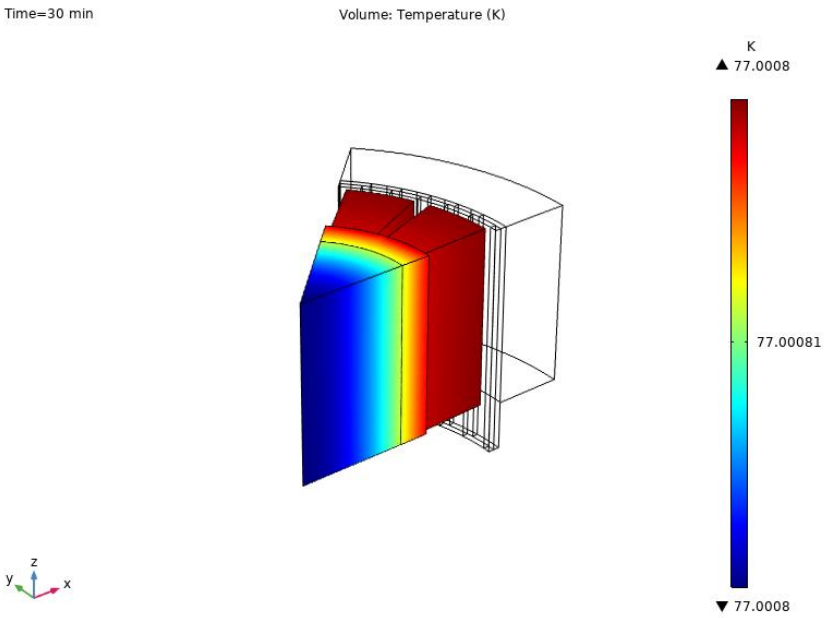

Figure 108. T(K) distribution. Rotor (t=30 min)

Table 5.2: Resume of maximum temperatures in the transitionary studies

Ambient conditions	Component	Time (s)	Maximum Temperature (K)
Normal ambient conditions (293.15 K)	Whole motor	**0.1**	293.2
		5	293.4
		10	293.5
		15	293.7
		20	293.8
		25	294
		30	294.1
	Winding	**0.1**	293.15681
		5	293.36812
		10	293.5297
		15	293.6872
		20	293.8327
		25	293.9719
		30	294.1050
	Magnets	**0.1**	293.15013
		5	293.2362
		10	293.3758
		15	293.5281
		20	293.6776
		25	293.8219

		30	293.9597
	Rotor	**0.1**	293.1508
		5	293.236
		10	293.375
		15	293.528
		20	293.677
		25	293.821
		30	293.959
Cryogenic ambient conditions without air gap (77 K)	**Whole motor**	**0.1**	77.01
		5	77.26
		10	77.52
		15	77.78
		20	78.03
		25	78.29
		30	78.55
	Winding	**0.1**	77.006
		5	77.26
		10	77.518
		15	77.775
		20	78.032
		25	78.2894
		30	78.55
	Magnets	**0.1**	77
		5	77
		10	77
		15	77
		20	77
		25	77
		30	77.00081
	Rotor	**0.1**	77
		5	77
		10	77
		15	77
		20	77
		25	77
		30	77.00081

The results in the resume table shows that there is hardly any variation in the maximum motor temperature from (0 to 30 min), for any of the different simulations performed. The maximum temperature reached by the motor under normal operating conditions at 30 minutes is 294.1 K, therefore it increases 0.95 K from its initial temperature. The maximum temperature reached by the motor under cryogenic operating conditions at 30 minutes is 78.55 K, thus it increases 1.55 K.

5.2.3 Stationary thermal simulations. Whole model

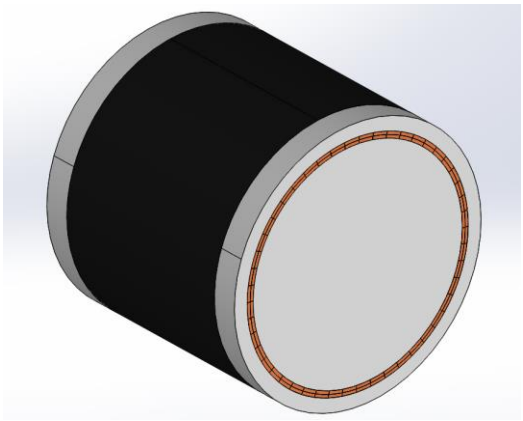

Figure 109. CAD motor design with air surrounding

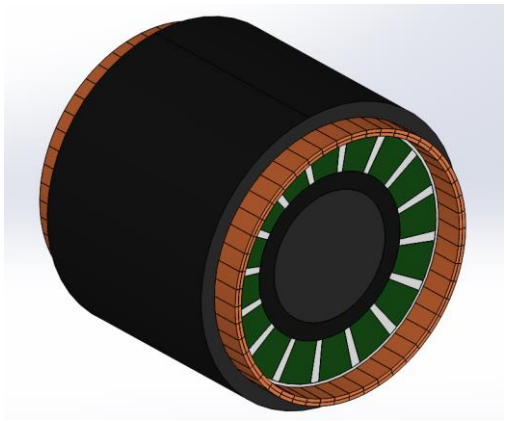

Figure 110. CAD motor design for simulation

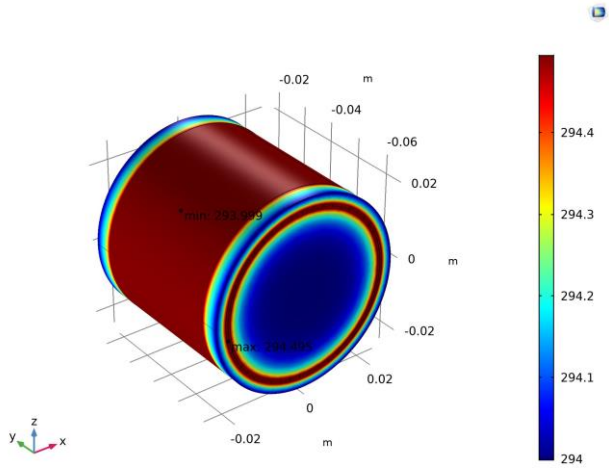

Figure 111. T(K) distribution. Motor (stationary)

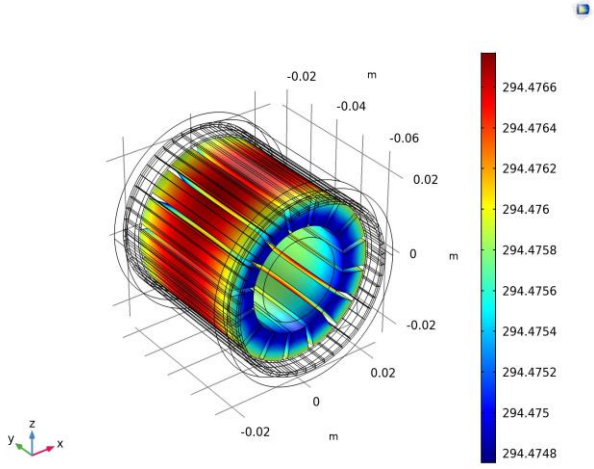

Figure 112. T(K) distribution. Magnets (stationary)

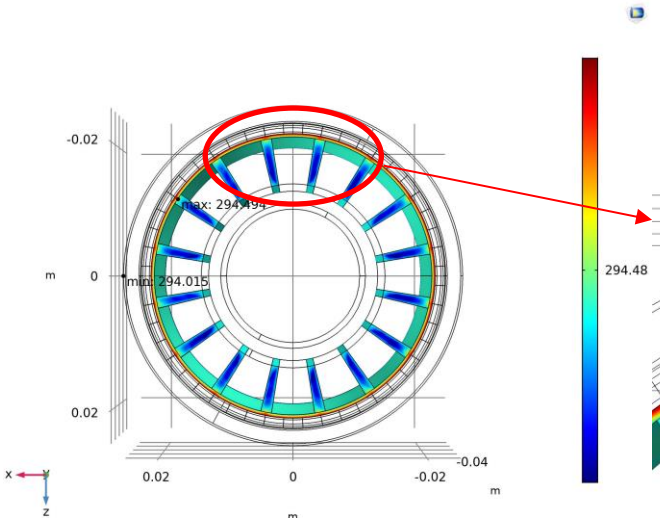

Figure 113. T(K) distribution in the air gap

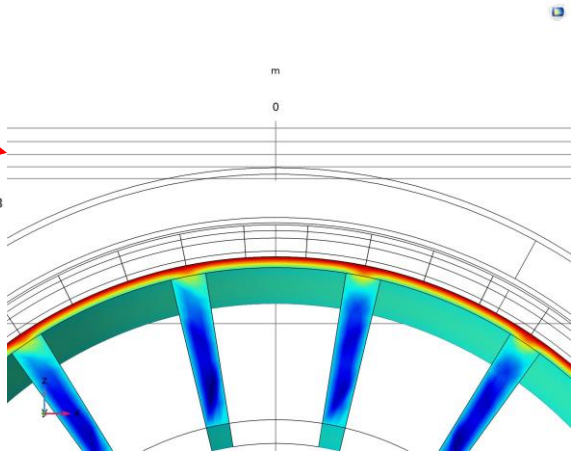

Figure 114. Zoom. T(K) distribution in the air gap

A simulation of the complete motor in steady state at normal temperature conditions was performed to verify that the results are similar to those of the simulations of the sector, the maximum temperatures differ around 2.4 K. It is preferable to trust the results of sector simulation, because the probability of error in the simulation modeling is much lower due to its less complexity. Furthermore, we must take into account that the convection coefficient selected have been different since the coefficient used in the complete model was the same as that used in the simulations of (Bratke, 2018) at the beginning of the development of this thesis, and it was not resimulated.
However, it is worth checking how the temperature is distributed in the design of the complete motor model, and how the distribution occurs in the air gap, where there is a great temperature jump due to the low conductivity of the air.

5.3 Motor losses simulation

The motor losses were obtained from the electromagnetic simulations to implement them in the thermal simulations as heat sources. It was decided that the results obtained should also be compared to obtain the grade of compatibility with the results of the analytical calculations.
The meaning of each of the motor losses was realized in chapter 3.

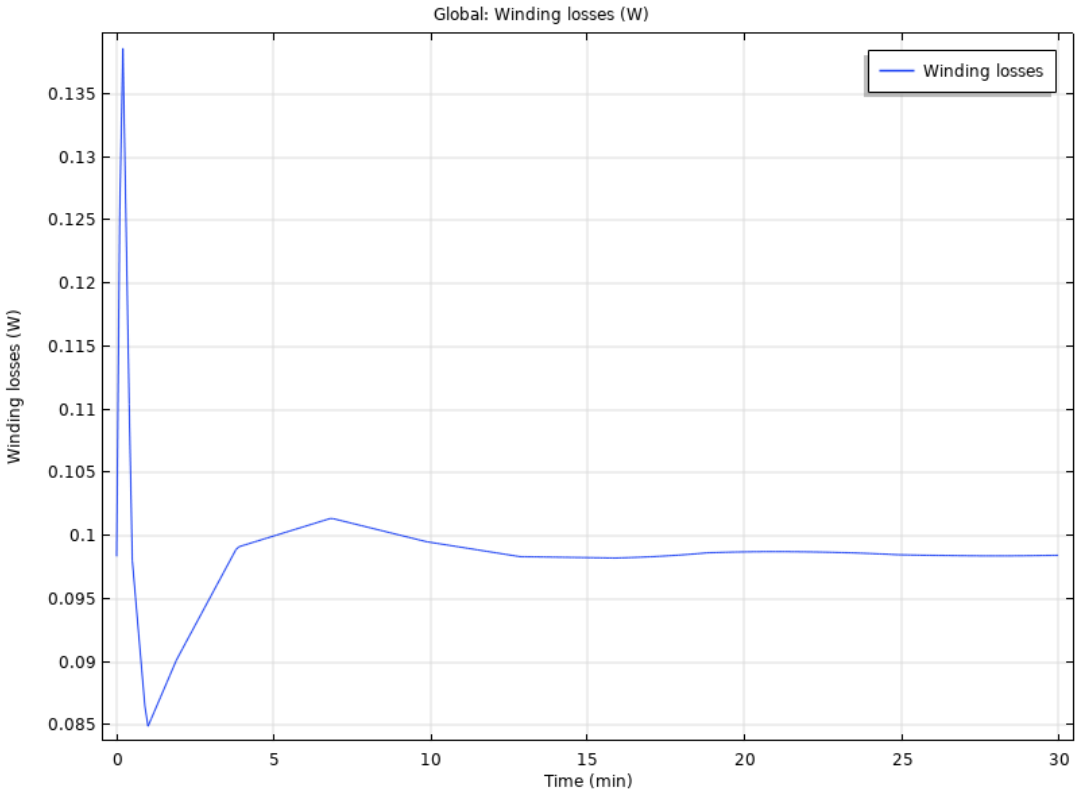

Figure 115. Winding losses. Simulation

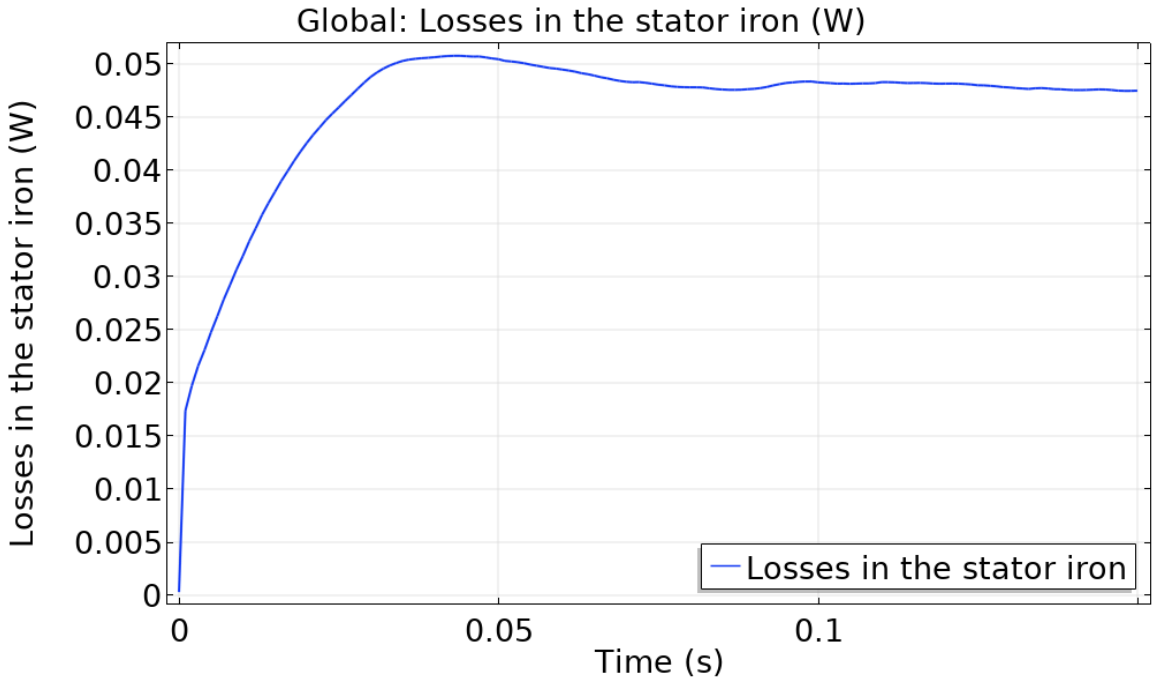

Figure 116. Stator losses. Simulation (Bratke, 2018)

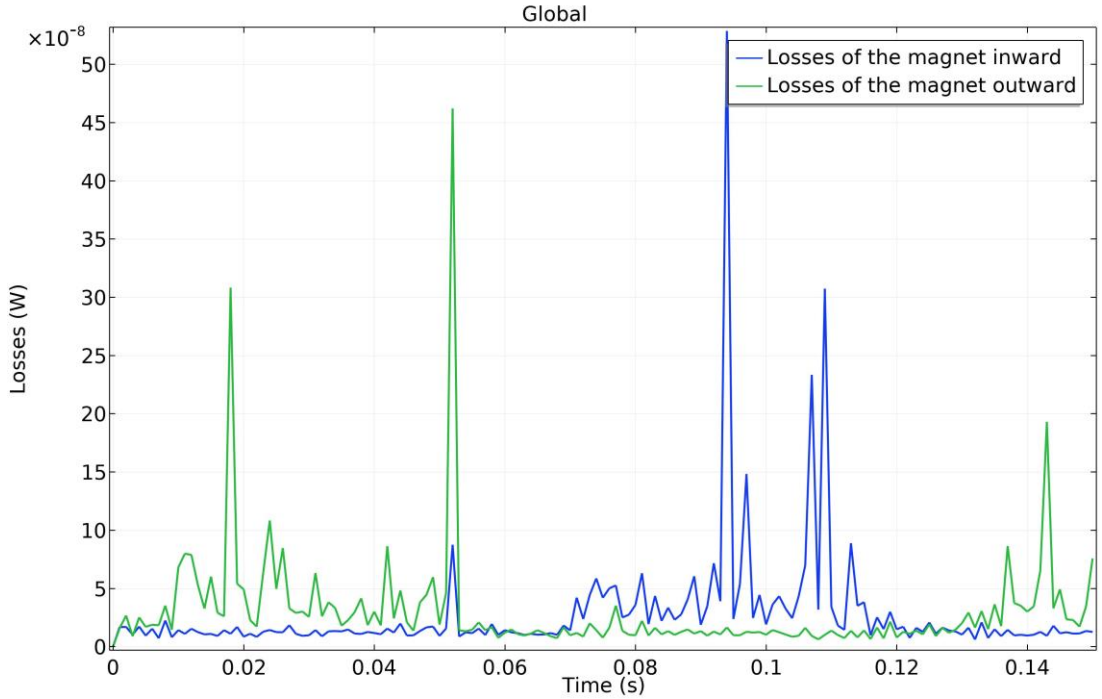

Figure 117. Magnet losses. Simulation (Bratke, 2018)

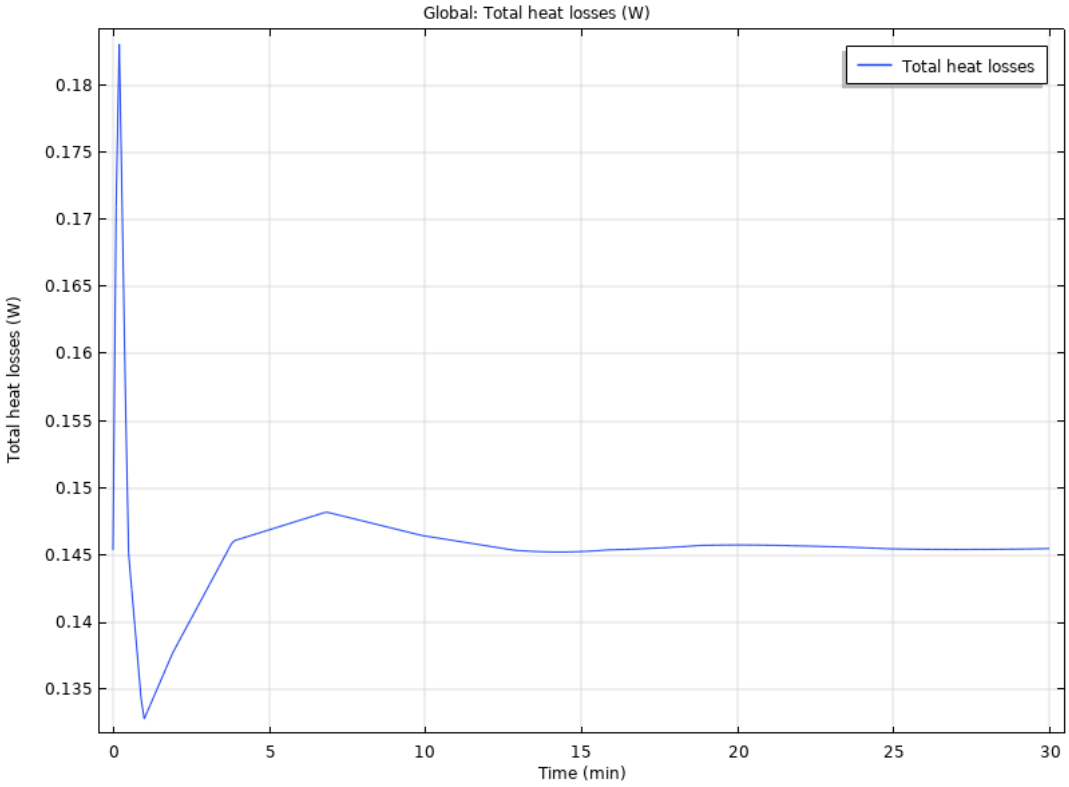

Figure 118. Total motor losses. Simulation

Table 5.3: Resume of losses results obtained from the simulations

Winding losses (W)	Stator losses (W)	Magnet losses (W)	Total losses (W)
0.098	0.047	10^{-8}	0.145

The winding losses due to the joule effect provoked by an electric current of I_{rms} were obtained in the thermal analysis

$$I = 0.5294\ (A);\ \ I_{rms} = {}^{I}/_{\sqrt{2}} = 0.37434\ (A) \tag{5.5}$$

The stator losses and the magnet losses were obtained by (Bratke, 2018) in the 3 D electromagnetic analysis. Finally, as the losses in the magnets can be neglected, the sum of total losses are the losses in the stator plus the losses in the winding.

6 Motor Test

In order to correlate results with simulations and analytical calculations, a prototype motor parameter measuring plan was carried out. For this, it was necessary to prepare the motor test setup, however, this development was not the objective of this thesis and it was necessary the help of third parties to develop it, so a brief scheme will be proposed with the components that compose it and a brief explanation of them. Nevertheless, for more information on the operation of the motor control and motor test setup, the theses (Babl, 2018) and (Grabichler, 2018) may be useful.

6.1 Motor Test Setup

The basic part of the control loop necessary to understand the motor test setup is shown in figure 3.1. Hereby the controller needs a Direct Current (DC)-supply, generates out of it a PWM (pulse width modulation) signal and provides it then as an (AC)-supply for the motor. The motor finally converts the input electrical power in output mechanical power. With the use of a resolver, which is located in the motor test bench, the controller gets specific information of the actual position status of the rotor. The control is a closed loop.

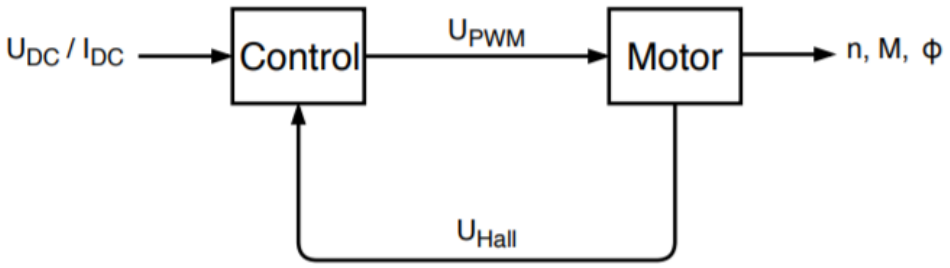

Figure 119. Schematic of the control loop (Grabichler, 2018)

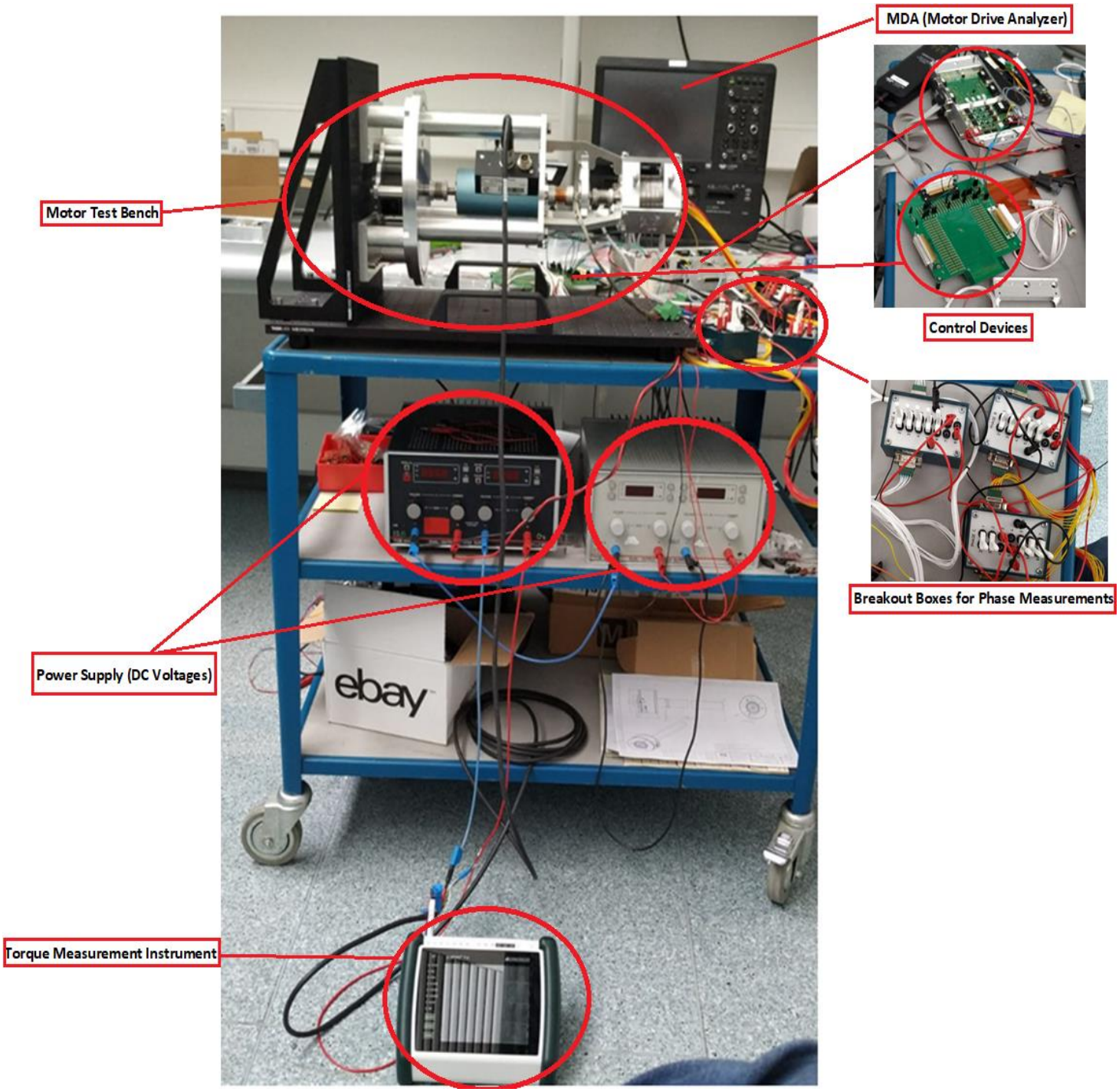

Figure 120. Structure of the motor test bench

In this image we can see the setup consisting on two power supplies providing 24V, 12V, 5V and 3.3V (DC voltages) to the control devices of the motor, the inverter converts DC into AC voltages provided to the motor. With the MDA, the AC three phase electrical current and voltage was measured. The breakout boxes have two sockets connecting the cables of the winding and they are used to provide different configurations of the winding for every phase (A, B, C).

The torque measurement device is connected to the torque sensor of the motor test bench. The torque sensor ejects voltages between −10 V and 10 V, which must be converted into torque by the ALMEMO. The calibration of the ALMEMO as well as more details of the setup can be seen in (Babl, 2018).
In the following picture the motor test bench can be seen more detailed.

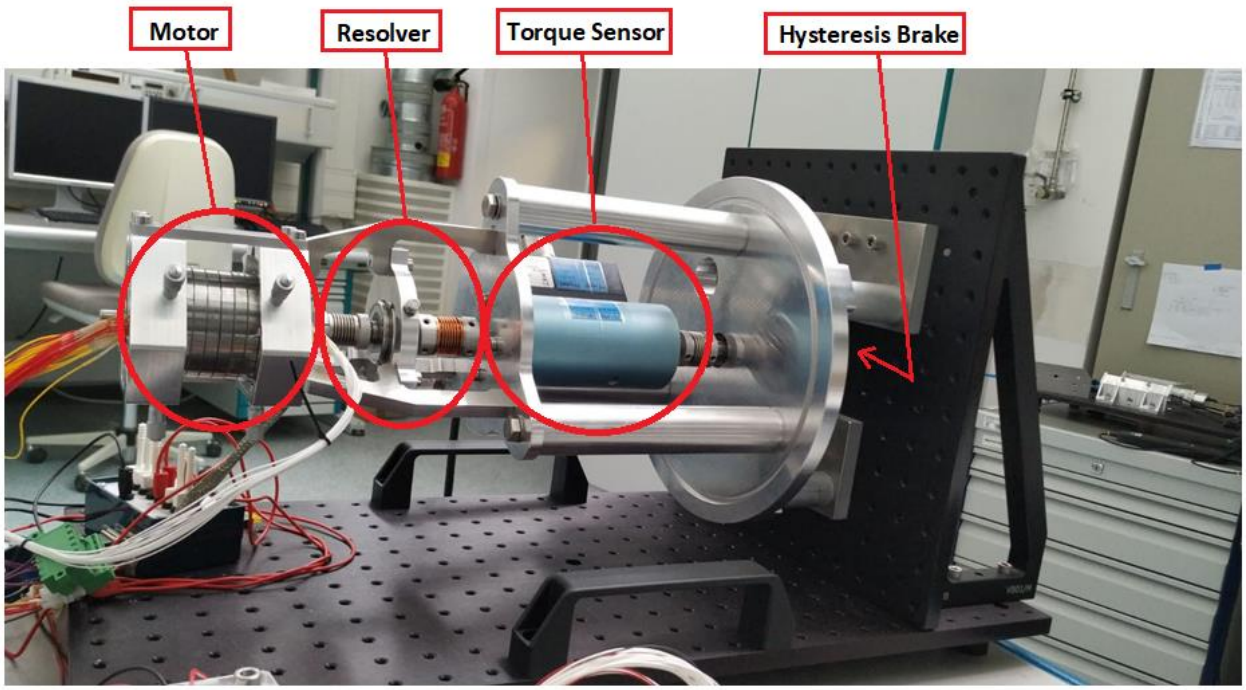

Figure 121. Structure of the motor test bench. Picture

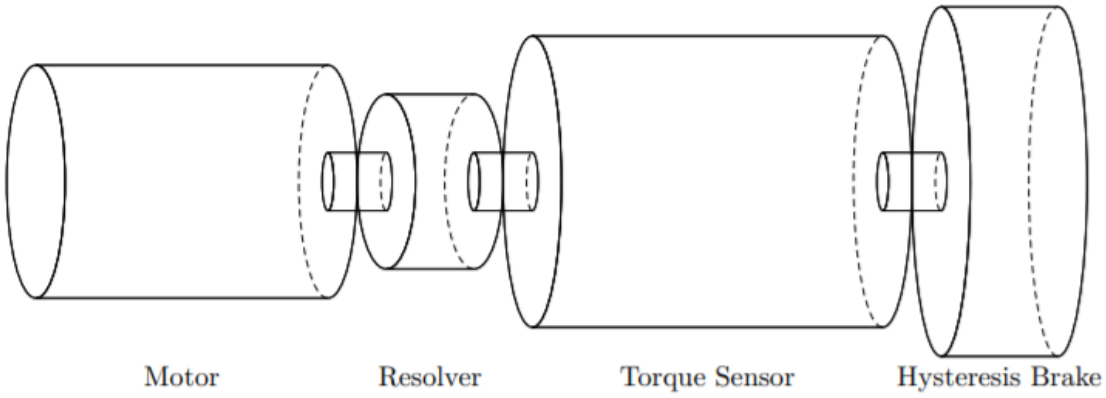

Figure 122. Structure of the motor test bench (Babl, 2018)

A schematic structure of the test bench can be seen in figure 122 The motor shaft is connected with a resolver, a torque sensor and a hysteresis brake. The resolver ejects the position of the rotor, the torque sensor measures the torque and the hysteresis brake is for the generating of a load, this hysteresis brake can be seen in the next picture.

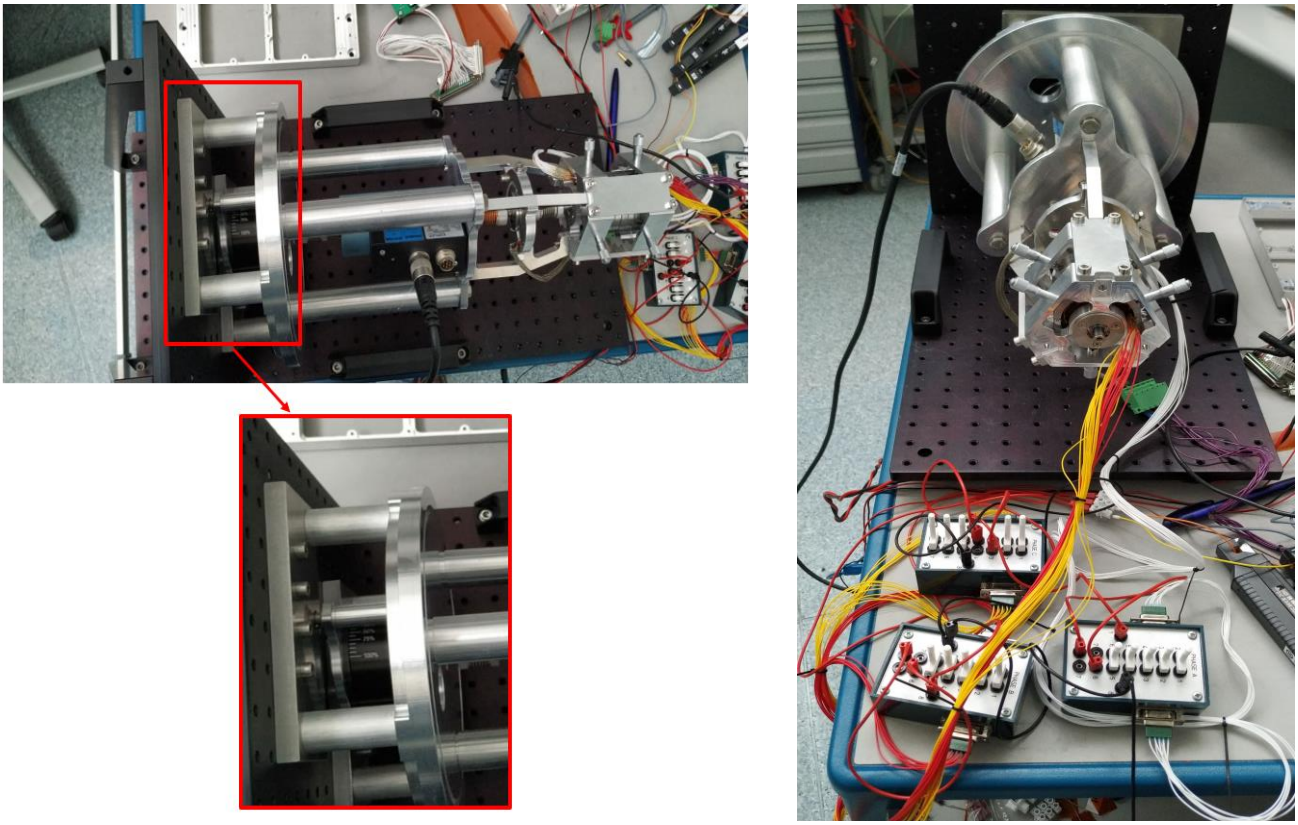

Figure 123 . Top side view with hysteresis brake zoom and front side view of the motor test bench

The pictures show us the top side view of the motor test bench and the front side view, it can be seen the hysteresis brake through the zoom image that was not seen in the previous schematic image of the motor test bench, the hysteresis brake range of values will be explained in the next chapter of the measuring plan. In the second image we can mainly appreciate the breakout boxes that connect the winding cables through the two sockets on each side of the boxes. Each box represents a phase, and they are also used as a measuring point of phase resistance and phase inductance.

6.2 Test measuring plan and results

A measurement plan has been designed to carry out measurements in an orderly way, following the same pattern. To do this, the three input parameters controlled were varied, increasing progressively (electrical frequency Fe(Hz), voltage (V) and mechanical load on the shaft (L)). In this way, the output parameters (the armature electric current Ia(mA) and the electromagnetic torque T(mN.m)) will be obtained and measured for each input parameter value. The tables with the data already measured and collected can be seen below and the order of variation of the parameters is as follows:
The frequency which is related with the rotational speed is varied three times (6.27 Hz, 12.5 Hz, 16.75 Hz), therefore three data tables are required. For each of them the phase voltage is varied three times (3.2 V, 4.5 V, 5.1 V), and finally for each voltage value the mechanical load in the shaft

is varied increasing progressively five times with (L1, L2, L3, L4, L5) values. The torque specification of the hysteresis brake is rated as: 0.014 - 0,52 Nm. This means the minimum torque brake (load) that we can apply is 0.014 at 0% and the maximum is 0.52 at 100%. L1(free) means no-load applied, and L5(max) is the maximum load that the motor is able to deal with before desynchronizing at that specific voltage and frequency situation. The loads presented have no values because their value is the same to the measured output torque T(mN.m) as was explained in the electromagnetic simulation section.

Table 6.1: Motor test measurements for a frequency (f = 6.27 Hz)

Fe1= 6.27 (Hz) → Ws=$\frac{120*Fe3}{p}*\frac{2\pi}{60}$ =4.92 (Rad/s)						
	V1=3.2(V)		V2=4.5(V)		V3=5.1(V)	
	Ia(mA)	T(mN.m)	Ia(mA)	T(mN.m)	Ia(mA)	T(mN.m)
L1(free)	664.5	0	928.5	0	1030	0
L2	653	30	922.3	31.5	1010	34
L3	647	35	906.9	36.2	996	40
L4	645	41	904	41	988	44
L5(max)	641	43	889.7	80	960	82.1

Maximum output torque

Table 6.2: Motor test measurements for a frequency (f = 12.5 Hz)

Fe2= 12.5(Hz) → Ws=$\frac{120*Fe3}{p}*\frac{2\pi}{60}$ =9.81 (Rad/s)						
	V1=3.2(V)		V2=4.5(V)		V3=5.1(V)	
	Ia(mA)	T(mN.m)	Ia(mA)	T(mN.m)	Ia(mA)	T(mN.m)
L1(free)	658.2	0	925	0	1015	0
L2	606.9	35	886	34	999.2	32
L3	602.8	40	879.3	39	990	40
L4	599	41.5	874.3	44	985	43
L5(max)	547	42	852	73.5	950	83

Maximum output torque

Table 6.3: Motor test measurements for a frequency (f = 16.75 Hz)

Fe3= 16.75(Hz)→ Ws=$\frac{120*Fe3}{p}*\frac{2\pi}{60}$=13.15(Rad/s)						
	V1=3.2(V)		V2=4.5(V)		V3=5.1(V)	
	Ia(mA)	T(mN.m)	Ia(mA)	T(mN.m)	Ia(mA)	T(mN.m)
L1(free)	639.7	0	917.7	0	1000	0
L2	581	35	870.4	34	989.6	35
L3	575	40	860.5	39	982.3	40.2
L4	573	41.5	853	44	978	44
L5(max)	550	42	825.7	73.5	946.5	83.5

Maximum output torque

The maximum output torque indicated in the tables will be compared with the calculations and the simulation, these values indicate the maximum load the motor is able to withstand for those given conditions of frequency and voltage. Below, these results are analyzed with graphs.

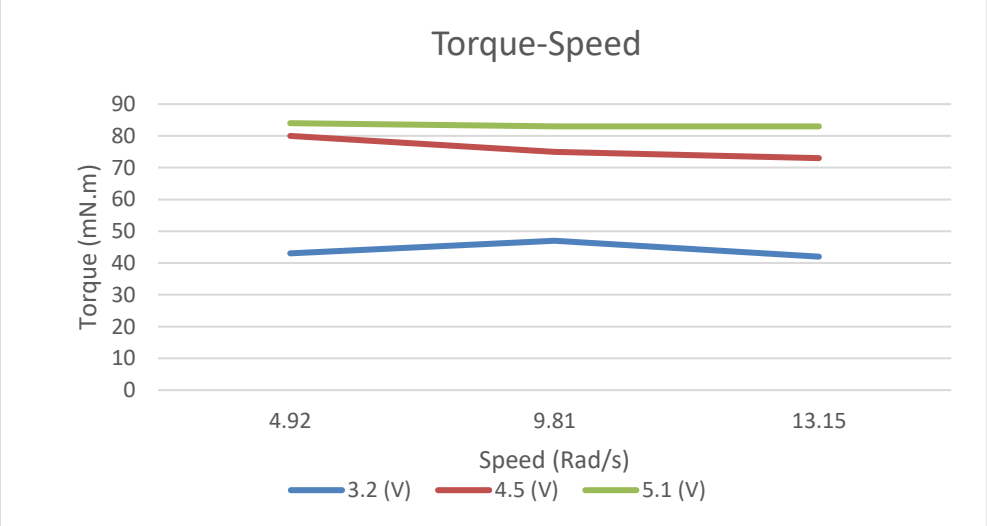

Graphic 6.1. Torque-Speed graphic

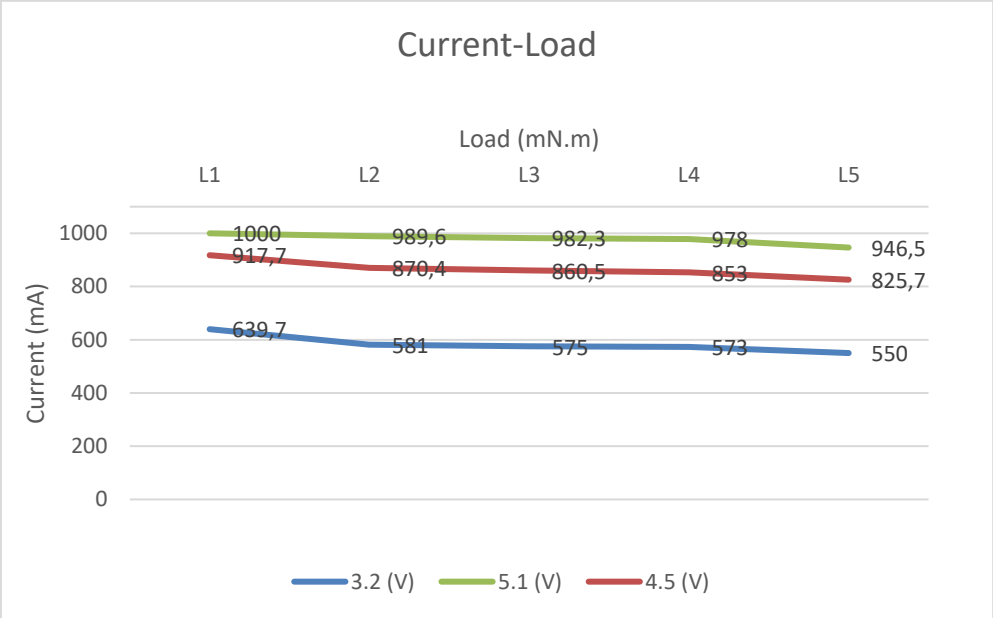

Graphic 6.2. Electric current-Load graphic

Graph 8 shows that as the voltage increases, the maximum electromagnetic torque increases and therefore the motor's operating range also increases, therefore for the same frequency (rotational speed) the motor will have a greater capacity to withstand the maximum load before going out of synchronism. In addition, the maximum torque hardly varies with frequency.

In Graph 9 we can check the case explained in section 2.5 about inconsistent results, since when increasing the load on the shaft, the phase electric current decreases progressively. This circumstance generates an important problem, because the current should increase by increasing the torque demanded by the load since we are demanding a higher input power to the motor, which is directly related to the current, and taking into account that the voltage is an input parameter kept constant, the only possibility to increase power and torque is by increasing the current in the winding, thus the results are unexpected. This is a big problem because the equations describing the motor obtained from the phasor diagram to obtain the parameters analytically are only valid for a case of normal motor behaviour under load.
Attempts have been made to find possible causes for this unexpected behavior of the motor, the author's proposal has to do with the resistance of the winding. The following is the input electric power equation:

$$P_{input} = 3V_a I_a cos(\Phi) + 3I_a^2 R_a \quad (6.1)$$

Taking into account that the power factor value $cos(\Phi)$ is close to 1 and it hardly varies when the load increases, and keeping the voltage constant V_a, the only way to increase the power is by increasing the current I_a, however, most synchronous motors found in the literature have an almost negligible resistance compared to the high reactance value, so that in their power equations they do not take into account the heat losses due to resistance. However in our motor

the opposite occurs, the resistance is much higher than the reactance (inductance) that was measured (40 microhenries), so it can be neglected and in this case if we must take into account the losses due to resistance, they are the second term of the equation. The behaviour of the motor proposed by the author is as follows:

By increasing the load, we would need more input power by increasing the current, however, taking into account the losses, the current would affect these more than the power itself, so the total power would decrease by increasing current through the winding. Due to this, the motor does just the opposite, it decreases the current because although the power $V_a I_a$ decreases, the losses $I_a^2 R_a$ decrease even more, so the overall power would be higher.

Although this explanation could not be verified through bibliographic research, it is the one that can make the most sense. In any case, as explained in previous chapters, we chose to look for an electromagnetic torque equation different from the one we wanted to create using the phasor diagram, in order to correlate the results with the other studies.

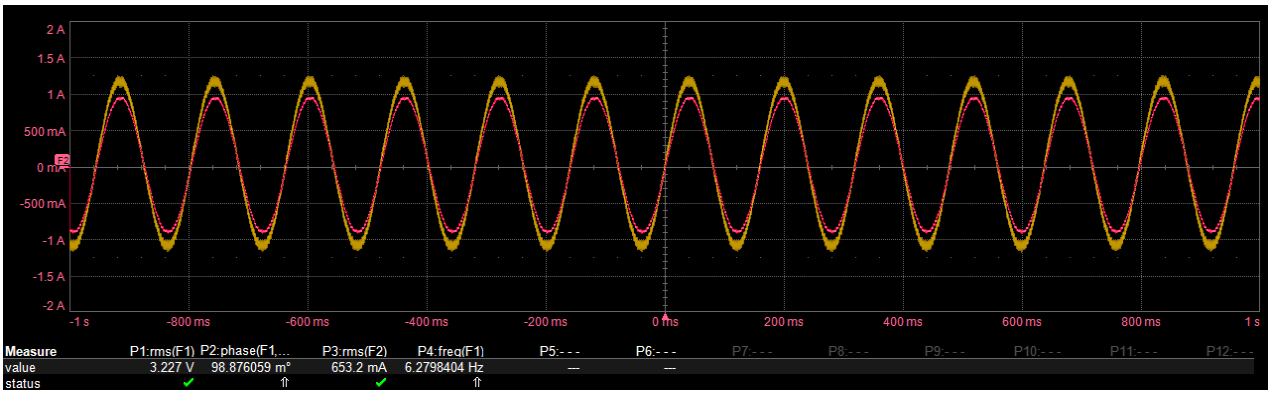

Figure 124. AC phase voltage (red waves) and AC phase current (yellow waves) for a frequency (f=6.27 Hz). Oscilloscope

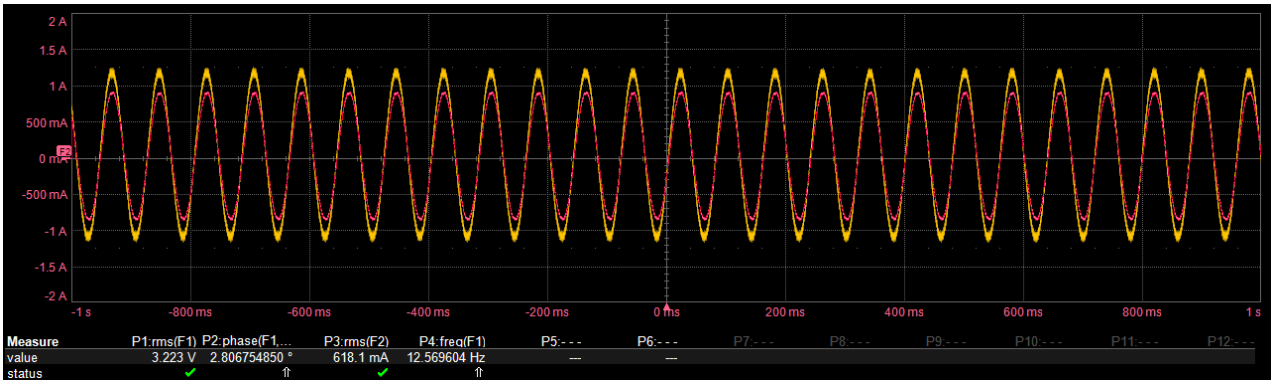

Figure 125. AC phase voltage (red waves) and AC phase current (yellow waves) for a frequency (f=12.56 Hz). Oscilloscope

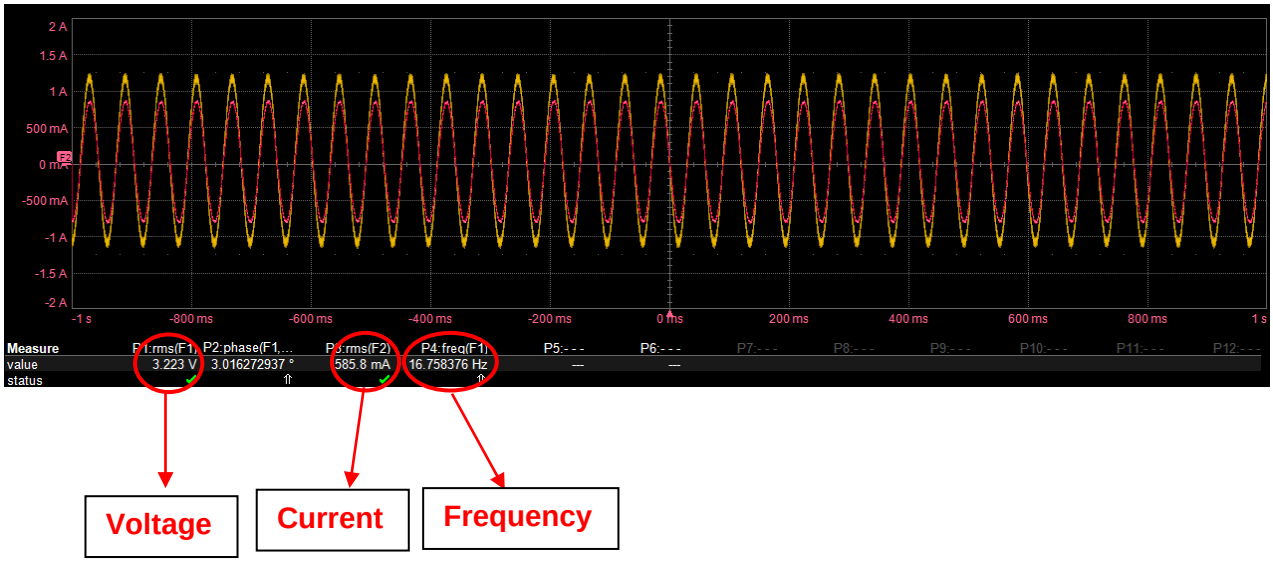

Figure 126. AC phase voltage (red waves) and AC phase current (yellow waves) for a frequency (f=16.75 Hz). Oscilloscope

In the three previous images the alternating current and voltage sine waves are shown on the oscilloscope screen, for three different frequencies keeping the load and voltage constant, we can check at the bottom of the images the RMS values of current and voltage obtained for the tables values.

7 Correlation of results

In this chapter the results are correlated to check the degree of compatibility between the three studies. First, the correlation of the electromagnetic torque results between calculations, measurements and simulations will be performed. The correlation of results of the temperature distribution between calculations and simulations, and the correlation of results of the motor losses obtained by calculations and by simulation.

7.1 Electromagnetic results correlation

The comparison has been made for seven different phase electric currents (from I1 to I7) maintaining the ambient temperature at 293.15 K. It should be noted that only a global electromagnetic simulation was performed, and this did not depend on the input current, but just on the applied load, so the output torque would always be equal to the load; in this case it was 80 mN.m. Next, the error percentage is obtained for each of the seven comparisons in order to determine the grade of compatibility.

Table 7.1: Correlation of results between test measured torque, analytical torque and simulated torque

T(N.m)	I_1 547(mA)	I_1 573(mA)	I_1 641(mA)	I_1 825.7(mA)	I_1 852(mA)	I_1 889.7(mA)	I_1 946.5(mA)	T(K)
Measured	42	41.5	43	73.5	74.2	80	83.5	**293.15**
Calculated	48.42	50.73	56.79	73.27	75.62	79	84.08	
Simulated							80	

$$\% \, error = \frac{|Measured - Calculated|}{Calculated} \times 100 \tag{7.1}$$

Table 7.2: Error percentage of electromagnetic torque correlation

% error						
I_1 547(mA)	I_1 573(mA)	I_1 641(mA)	I_1 825.7(mA)	I_1 852(mA)	I_1 889.7(mA)	I_1 946.5(mA)
13.25 %	18.19 %	24.28 %	0.31 %	1.87 %	1.26 %	0.69 %

Error

The highest error percentage has been obtained in the first three comparisons, where the phase current and therefore the applied voltage were lower. It is probable that this was due to problems in the measurements since the maximum torque values have remained constant, even increasing the current.

7.2 Thermal results correlation

7.2.1 Thermal results correlation at normal conditions

The temperature distribution correlation for room temperature of 293.15 K has been made between the simulations in stationary regime and the analytical calculations that can be verified in the annex of the Matlab code. Subsequently, the error percentage is calculated to ascertain the grade of compatibility between both studies.
The temperature T5 corresponds to the temperature of the outer surface of the stator, and T1 to that of the rotor shaft.

Table 7.3: Correlation of results between analytical and simulated temperature distribution at normal ambient conditions

Motor temperature distribution at normal ambient conditions (293.15K)							
	T5(K)	**T4(K)**	**T3(K)**	**T3f(K)**	**T2f(K)**	**T2(K)**	**T1(K)**
Simulation	296.8	296.891	296.85	296.6	296.6	296.6	296.6
Analytical	296.7739K	296.7793	296.7792	296.5916	295.995	295.8809	295.7667

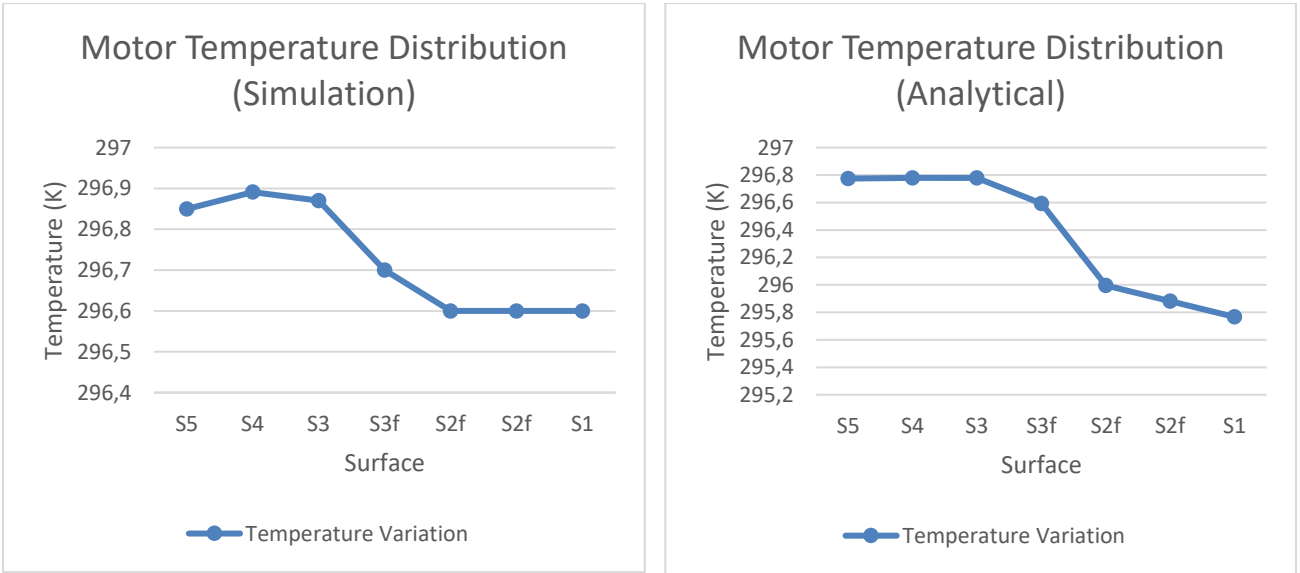

Graphic 7.1. Motor temperature distribution at normal ambient conditions. Graph comparison

$$\% \, error = \frac{|Calculated - Simulated|}{Simulated} \times 100 \tag{7.2}$$

Table 7.4: Error percentage of temperature distribution correlation at normal conditions

% *error*						
T5(K)	**T4(K)**	**T3(K)**	**T3f(K)**	**T2f(K)**	**T2(K)**	**T1(K)**
0.0087 %	0.037 %	0.023 %	0.0028 %	1.87 %	0.203 %	0.281 %

For the calculation of error in this case, the simulation has been taken as a safe value, so the roles of the formula have been reversed with respect to the percentage of error in the electromagnetic torque and in this case the percentage of error will correspond to the error produced by the calculations with respect to the simulation. We can check from the graphs that a temperature jump occurs in the air gap of the motor due to the low conductivity of the air, while the temperatures on the stator surfaces (T5, T4, T3) and the rotor (T2, T1) remain constant due to the high conductivity of the materials.

Finally, although the temperatures on the surface of the rotor (T2f, T2, T1) have a higher percentage of error, possibly due to mistakes in the equations of heat transfer in the air gap, we can conclude that the results obtained are satisfactory because of the high grade of compatibility between the simulations and the calculations.

7.2.2 Thermal results correlation at cryogenic conditions

The temperature distribution correlation for cryogenic ambient temperature (77 K) has been made between the simulations in stationary regime and the analytical calculations that can be verified in the annex of the Matlab code. Subsequently, the error percentage is calculated to ascertain the grade of compatibility between both studies. However, as we can see in the table, it was not possible to obtain the results of the theoretical calculations in the rotor surfaces because the results were complex numbers, possibly due to mistakes in the equations of heat transfer in the air gap, so it has only been possible to compare the distribution of temperatures on the stator surfaces. In order to draw the graph from the analytical results, the data of the rotor temperatures in the simulations were taken.

Table 7.5: Correlation of results between analytical and simulated temperature distribution at cryogenic ambient conditions

Motor temperature distribution at cryogenic ambient conditions (77K)					
	T5(K)	**T4(K)**	**T3(K)**	**T2(K)**	**T1(K)**
Simulation	134.6	134.668	134.6	85.5275	85.5275
Analytical	135.0619	135.0673	135.0672	x	x

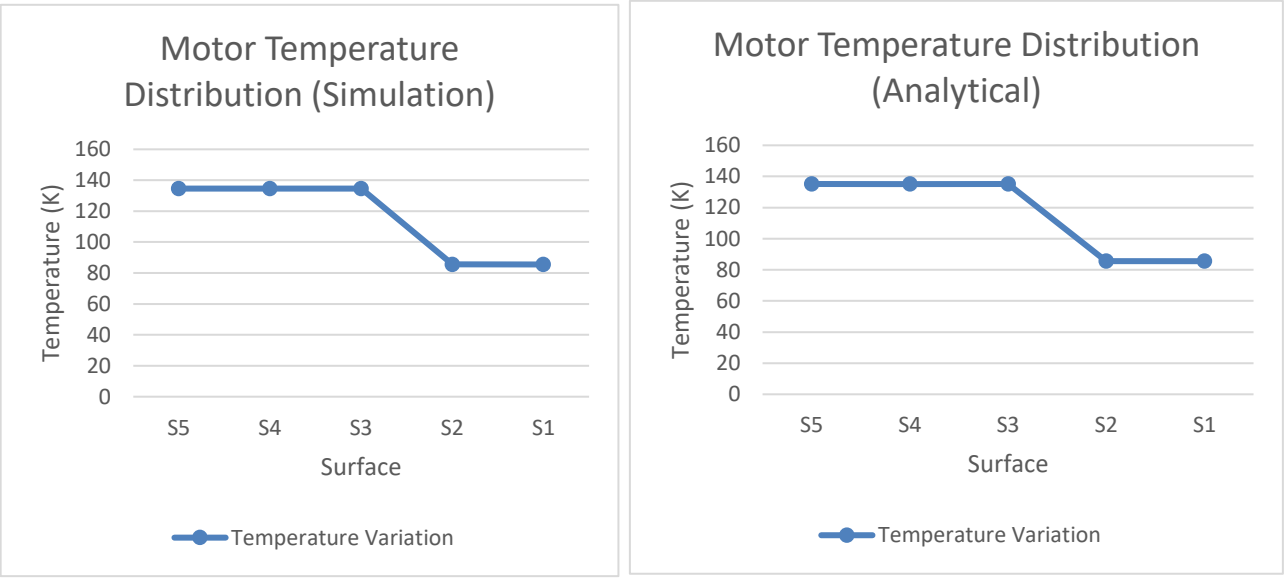

Graphic 7.2. Motor temperature distribution at cryogenic ambient conditions. Graph comparison

$$\% \, error = \frac{|Calculated - Simulated|}{Simulated} \times 100 \tag{7.3}$$

Table 7.6: Error percentage of temperature distribution correlation at cryogenic conditions

% error				
T5(K)	**T4(K)**	**T3(K)**	**T2(K)**	**T1(K)**
0.343 %	0.296 %	0.347 %	x	x

In this case, the graphs show a much higher temperature jump than the one produced for normal ambient conditions because there is no air gap between the stator and the rotor. Therefore, the only heat transfer produced is by means of radiation, since the convection and air conduction are eliminated.

7.3 Motor losses results correlation

The correlation of motor losses has been made between electromagnetic and thermal simulations and theoretical calculations. Again, the losses obtained through simulation will be reliable, so the error percentage of the calculations with respect to the simulations is obtained.

Table 7.7: Resume of losses results obtained from the simulations

	Winding losses (W)	Stator losses (W)	Magnet losses (W)	Total losses (W)
Simulation	0.098	0.047	10^{-8}	0.145
Analyrical	0.07	0.054	10^{-4}	0.125

$$\% \, \boldsymbol{error} = \frac{|\boldsymbol{Calculated} - \boldsymbol{Simulated}|}{\boldsymbol{Simulated}} \times \mathbf{100} \tag{7.4}$$

Table 7.8: Error percentage of motor losses correlation

$\% \, \boldsymbol{error}$			
Winding losses (W)	**Stator losses (W)**	**Magnet losses (W)**	**Total losses (W)**
28.57 %	12.96%	x	13.79 %

The grade of compatibility is good in general terms despite the important error rate of 13.5% in the global motor losses. But the magnet losses correlation must be revised and improved in subsequent studies, because although in both studies these losses can be neglected due to its low value compared to the rest of the losses, it is much lower in the simulation than in the calculations.

8 Conclusion and outlook

In this thesis, an electromagnetic analysis of a PMSM is performed to calculate the maximum induced electromagnetic torque under different operating conditions, the results are obtained from simulations, analytical calculations and test measurements. A thermal analysis is performed to obtain the temperature distribution of the PMSM under different operating conditions, the results are obtained from simulations and analytical calculations. An analysis of motor losses is also executed, the results are obtained from simulations and analytical calculations. The analytical calculation for the three studies is accomplished with MATLAB software implementing the corresponding equations. The simulations has been realized with COMSOL Multiphysics software. The results obtained and summarized in chapter 7 are satisfactory despite some errors in calculations and measurements, which lead to the impossibility of obtaining reliable results. The error percentage that determines the degree of compatibility of the comparisons is calculated to assess the correlation. In addition to the main objective of the thesis, which is the correlation of results to obtain the degree of compatibility between simulations, analytical calculations and test measurements, some research studies have been included, complementing the whole thesis. In the Analytical Calculations chapter 4.1.3, two studies are carried out, related to the capacity of the permanent magnets of the motor to induce electromagnetic torque for different operating temperature states, and for two different magnet materials (NdFeB and SmCo17). Finally, the NdFeB is verified as the optimal permanent magnet to achieve a higher maximum torque, supporting greater loads on the shaft, and that its capacity decreases by increasing temperature. In chapter 5.2 of Thermal Simulations, in addition to the results in stationary regimen to perform the correlation of results, a great multitude of simulations have been carried out in transient regimen for cryogenic conditions and vacuum pressure (77 K, 10^{-8}atm), and for normal conditions of temperature and pressure (293.15 K, 1 atm). A significant amount of data of the motor temperature distribution is collected for different periods of time, from 0 to 30 min. This study is made with the objective of determining a more realistic maximum motor temperature since it will not be operated infinitely in the reality. This is essential in order to not jeopardize, for example, the resistance of the winding, which can be impaired by large temperature rises.

In the future it would be appropriate to carry out the electromagnetic correlation with more parameters apart from the maximum torque, to achieve greater security in the verification of electromagnetic results. Besides, thermal measurements with temperature sensors on the motor should be carried out in future studies to complete the verification triangle in the thermal and loss analysis.

Bibliography

- Babl, A. (2018). *Pre-Tests for the Development of a Permanent Magnet Synchronous Machine.* Munich: Department of Electrical and Computer Engineering Technical University of Munich.

- Bratke, C. (2018). *MultiphysicalSimulationofaPermanent Magnet Synchronous Motor.* Munich.

- Deeb, R. (2011). *Calculation of Eddy Current Losses in Permanent Magnets of Servo Motor.* Brno: Department of Power Electrical and Electronic Engineering, Faculty of Electrical Engineering and Communication.

- Douglas, A. (s.f.). *Synchronous Motors When a synchronous machine is used as a motor, it is not self-starting. If the rotor field poles are excited by the field current and.* Obtenido de https://www.google.com/url?sa=i&url=https%3A%2F%2Fslideplayer.com%2Fslide%2F5927012%2F&psig=AOvVaw2jpR6lE5bSDMWUkbAE8725&ust=1585010673435000&source=images&cd=vfe&ved=0CAIQjRxqFwoTCOil-4Wvr-gCFQAAAAAdAAAAABAE

- *Electricalbaba.* (16 de June de 2018). Obtenido de https://electricalbaba.com/permanent-magnet-synchronous-motor-pmsm-construction-working-principle/

- *Electricalexams 2018-20.* (2020). Obtenido de https://www.electricalexams.co/why-three-phase-synchronous-motor-is-not-self-starting/unidirectional-torque-synch/

- ESA. (s.f.). *http://www.cosmos.esa.int/web/bepicolombo/mixs*.

- Faizan, A. (s.f.). *Synchronous Motor Generator: Efficiency & Losses*. Obtenido de https://electricalacademia.com/synchronous-machines/synchronous-motor-generator-efficiency-losses/

- Fraser, C. J. (1994). En *Mechanical Engineer's Reference Book (Twelfth Edition).*

- Garcia, J. R. (s.f.). *Transmisión del calor.* Cartagena: Universidad Politécnica de Cartagena.

- Grabichler, J. (2018). *Design and Development of an Electrical Drive Train operated in Cryogenic and Space Environment.* Munich: Technical University of Munich.

- Karnehm, V. (2017). *Design of an Electrical Actuator for Cryostatic Applications.* Munich.

- Krishnan, R. (2009). *Permanent Magnet Synchronous and Brushless DC Motor Drives.* CRC Press.

- KWON, B.-I. (2013). Permanent Magnet Machines Cahpter 5. Seoul: Hanyang University · Department of Electronics and Computer Engineering.
- *Magnetic properties YXG32.* (s.f.). Obtenido de https://magnetsim.com/grades/YXG32
- Max-Planck-Gesellschaft. (2020). Obtenido de https://www.mpe.mpg.de/576082/overview
- Max-Planck-Gesellschaft. (2020). Obtenido de http://www.mpe.mpg.de/ir/gravity
- Paudel, N. (18 de July de 2016). *How to Analyze an Induction Motor: A TEAM Benchmark Model.* Obtenido de https://www.comsol.com/blogs/how-to-analyze-an-induction-motor-a-team-benchmark-model/
- *Permanent Magnet Synchronous Motor (PMSM) – Construction and Working Principle*. (2018). Obtenido de https://electricalbaba.com/permanent-magnet-synchronous-motor-pmsm-construction-working-principle/#comments
- *Properties of air at 1 atm.* (s.f.). Obtenido de https://www.me.psu.edu/cimbala/me433/Links/Table_A_9_CC_Properties_of_Air.pdf
- Radoslaw Jez, A. P. (2014). Influence of air-gap length and cross-section on magnetic circuit parameters . *COMSOL*.
- Ramón Bargalló Perpiñà, J. M. (s.f.). *Programa de Análisis Térmico de Máquinas Eléctricas Rotativas.* Barcelona: Departamento de Ingeniería Eléctrica EUETIB, Universidad Politécnica de Catalunya .
- Rodríguez Pozueta, M. Á. (2018). *Máquinas Eléctricas II.* Cantabria: Universidad de Cantabria.
- Ruiz, J. Á. (2014). *Metodología de cálculo térmico y criterios de diseño para máquinas eléctricas con sistemas de refrigeración abierto.* Donostia, San Sebastián: Universidad de Navarra.
- *Samarium Cobalt Magnets, SmCo Magnets Datasheet.* (s.f.). Obtenido de https://www.eclipsemagnetics.com/media/wysiwyg/datasheets/magnet_materials_and_assemblies/samarium_cobalt_magnets_datasheet.pdf
- Schoch, S. (2019). *Design of a Modular Electric Motor Prototype.* Munich.
- *Sintered Neodymium-Iron-Boron Magnets.* (s.f.). Obtenido de https://www.arnoldmagnetics.com/wp-content/uploads/2017/11/N45SH-151021.pdf

- *Starting a Synchronous Motor*. (2020). Obtenido de https://instrumentationtools.com/starting-a-synchronous-motor/
- Tapia Olvera, R. (s.f.). Obtenido de https://www.milenio.com/opinion/varios-autores/universidad-politecnica-de-tulancingo/importancia-de-los-motores-electricos-en-la-sociedad
- *Vacuumschmelze. Cobalt Iron properties.* (s.f.). Obtenido de https://vacuumschmelze.com/Assets/Cobalt-Iron%20Alloys.pdf

List of figures

1. CAD model PMSM 2
2. CAD model PMSM with components 5
3. Dimension values of the motor components (Schoch, 2019) 6
4. Vibration due to not self-starting (Douglas, s.f.) 9
5. Synchronous motor configurations 11
6. Torque-Load angle curve of a synchronous motor (Fraser, 1994) 12
7. Load/torque angle (Starting a Synchronous Motor, 2020) 14
8. Phasor diagram and synchronous motor electrical circuit 15
9. Phasor diagram synchronous motor proposed by the author of the thesis for the case of the MPE synchronous motor under different loads 15
10. Phasor diagram without resistance 16
11. Magnetic circuit simplification of a PMSM (Krishnan, 2009) 17
12. Flux lines distribution in magnetic cores; without air-gap and with air-gap (fringing flux can be observed) (Radoslaw Jez, 2014) 23

13. Eddy currents in magnet 25

14. Cylinder model for heat transfer, basic mechanisms description 33

15. Design by CAD solidworks, of the simplified motor; the sources of heat and the directions of the heat flow towards the interior and exterior of the motor 34

16. Cylinder model for heat transfer 40

17. Conduction heat transfer stator 41

18. Conduction heat transfer winding 43

19. Taylor vortex in the concentric two-cylinder hollow with rotation. 43

20. Conduction heat transfer air gap 45

21. Conduction heat transfer magnet 46

22. Rotor shaft temperature 46

23. Radiation heat transfer vacuum gap 47

24. Imperfect contact between surfaces 48

25. Implementing the differential equations for rotor angular velocity and angle using the Global ODEs and DAEs interface. (Paudel, 2016) 50

26. No-load output torque 53

27. Loaded output torque 53

28. Rotational speed of the motor (10 rad/s) 53

29. Loaded at 0 (s) output torque 54

30. 3D simulation. Output torque (Arkkio and force calculation methods) Parametric sweep 54

31. 3D simulation. Output torque (Arkkio and force calculation methods) Time dependent 54

32. No-load output torque 54

33. Loaded output torque 55

34. 3D simulation. Output torque (Arkkio and force calculation methods) Time dependent..... 55

35. 3D simulation. Output torque (Arkkio and force calculation methods) Time dependent..... 56

36. AC Voltage and current of the 2D motor simulation 56

37. Mesh model 57

38. Winding heat source 59

39. Temperature distribution. Motor sector..... 59

40. Temperature distribution. Winding 59

41. Temperature distribution. Magnets 59

42. Temperature distribution. Rotor..... 59

43. Temperature distribution. Whole model (normal conditions)-Stationary-..... 59

44. Temperature distribution. Motor sector..... 60

45. Temperature distribution. Winding 60

46. Temperature distribution. Magnets 60

47. Temperature distribution. Rotor..... 60

48. Temperature distribution. Whole model (cryogenic conditions with air gap) -stationary- 60

49. Temperature distribution. Motor sector..... 61

50. Temperature distribution. Winding 61

51. Temperature distribution. Magnets..... 61

52. Temperature distribution. Rotor..... 62

53. Temperature distribution. Whole model (cryogenic conditions without air gap) stationary- 62

54. Temperature distribution. Sector (t=0 min) 62

55. Temperature distribution. Sector (t=0.1 min) 63

56. Temperature distribution. Sector (t=2.5 min) 63

57. Temperature distribution. Sector (t=5 min) 64

58. Temperature distribution. Sector (t=10 min) 64

59. Temperature distribution sector (t=15 min) 64

60. Temperature distribution.Sector (t=20 min) 64

61. Temperature distribution. Sector (t=25 min) 64

62. Temperature distribution. Sector (t=30 min) 64

63. T(K) distribution. Winding (t=0.1 min) 65

64. T(K) distribution.Winding (t=5 min) 65

65. T(K) distribution. Winding (t=10 min) 65

66. T(K) distribution. Winding (t=15 min) 66

67. T(K) distribution. Winding (t=20 min) 66

68. T(K) distribution. Winding (t=25 min) 66

69. T(K) distribution. Winding (t=30 min) 66

70. T(K) distribution. Magnets (t=0.1 min) 66

71. T(K) distribution. Magnets (t=5 min) 67

72. T(K) distribution. Magnets (t=10 min) 67

73. T(K) distribution. Magnets (t=15 min) 67

74. T(K) distribution. Magnets (t=20 min) 67

75. T(K) distribution. Magnets (t=25 min) 67

76. T(K) distribution. Magnets (t=30 min) 67

77. T(K) distribution. Rotor (t=0.1 min) 68

78. T(K) distribution. Rotor (t=5 min) 68

79. T(K) distribution. Rotor (t=10 min) 68

80. T(K) distribution. Rotor (t=15 min) 69

81. T(K) distribution. Rotor (t=20 min) 69

82. T(K) distribution. Rotor (t=25 min) 69

83. T(K) distribution. Rotor (t=30 min) 69

84. T(K) distribution. Sector (t=0 min) 69

85. T(K) distribution. Sector (t=0.1 min) 70

86. T(K) distribution. Sector (t=5 min) 70

87. T(K) distribution. Sector (t=10 min) 70

88. T(K) distribution. Sector (t=15 min) 70

89. T(K) distribution. Sector (t=20 min) 70

90. T(K) distribution. Sector (t=20 min) 70

91. T(K) distribution. Sector (t=25 min) 71

92. T(K) distribution. Rotor (t=30 min) 71

93. T(K) distribution. Winding (t=0.1 min) 71

94. T(K) distribution. Winding (t=5 min) 72

95. T(K) distribution. Winding (t=10 min) 72

96. T(K) distribution. Winding (t=15 min) 72

97. T(K) distribution. Winding (t=20 min) 72

98. T(K) distribution. Winding (t=25 min) 72

100. T(K) distribution. Winding (t=30 min) 73

101. T(K) distribution. Magnets (t=0.1 min) 73

102. T(K) distribution. Magnets (t=5 min) 73

103. T(K) distribution. Magnets (t=10 min) 74

104. T(K) distribution. Magnets (t=15 min) 74

105. T(K) distribution. Magnets (t=20 min) 74

106. T(K) distribution. Magnets (t=25 min) 74

107. T(K) distribution. Magnets (t=30 min) 74

108. T(K) distribution. Rotor (t=30 min) 75

109. CAD motor design with air surrounding 77

110. CAD motor design for simulation 77

111. T(K) distribution. Motor (stationary) 77

112. T(K) distribution. Magnets (stationary) 77

113. T(K) distribution in the air gap 77

114. Zoom. T(K) distribution in the air 77

115. Winding losses. Simulation 78

116. Stator losses. Simulation 79

117. Magnet losses. Simulation 79

118. Total motor losses. Simulation 80

119. Schematic of the control loop (Grabichler, 2018) 81

120. Structure of the motor test bench 82

121. Structure of the motor test bench. Picture.....83

122. Structure of the motor test bench (Babl, 2018).....83

123. Top side view with hysteresis brake zoom and front side view of the motor test bench 84

124. AC phase voltage (red waves) and AC phase current (yellow waves) for a frequency (f=6.27 Hz). Oscilloscope.....88

125. AC phase voltage (red waves) and AC phase current (yellow waves) for a frequency f=12.56Hz). Oscilloscope.....88

126. AC phase voltage (red waves) and AC phase current (yellow waves) for a frequency f=16.75 Hz). Oscilloscope.....89

127. Model Builder Tree of COMSOL Multiphysics.....59

128. Selection and description of the motor materials (winding, rotor-stator, magnets, air) 60

129. Convection heat transfer and stator heat source descriptions 60

List of tables

2.1 Material properties 6

2.2 Dimension values of motor components 9

4.1 Magnet magnetic flux density and maximum electromagnetic torque values for NDFEB magnets depending on the electric current and at ambient normal conditions.....26

4.2 Magnet flux density values dependent on current and ambient temperature for NdFeB magnets 27

4.3 Maximum torque values dependent on current and ambient temperature for NdFeB magnet 28

4.4 Maximum torque depending on the magnet material at normal conditions 30

4.5 Node-surface assignment 39

4.6 Thermal resistance assignment 39

4.7 Air properties at T_{af} 41

4.8 Temperature distribution at normal conditions.....47

4.9 Temperature distribution at cryogenic conditions 49

5.1 Resume of maximum temperatures in the stationary studies 63

5.2 Resume of maximum temperatures in the transitionary studies 75

5.3 Resume of losses results obtained from the simulations 80

6.1 Motor test measurements for a frequency (f = 6.27 Hz).....85

6.2. Motor test measurements for a frequency (f = 12.5 Hz).....85

6.3. Motor test measurements for a frequency (f = 16.75 Hz).....86

7.1. Correlation of results between test measured torque, analytical torque and simulated torque 90

7.2. Error percentage of electromagnetic torque correlation..... 90

7.3. Correlation of results between analytical and simulated temperature distribution at normal ambient conditions 91

7.4. Error percentage of temperature distribution correlation at normal conditions 92

7.5. Correlation of results between analytical and simulated temperature distribution at cryogenic ambient conditions 92

7.6. Error percentage of temperature distribution correlation at cryogenic conditions 92

7.7. Resume of losses results obtained from the simulations 93

7.8. Error percentage of motor losses correlation 93

List of graphics

4.1. Magnet flux-Temperature-Electric current graphic for NdFeB magnets 28

4.2. Max torque-Temperature graphic for NdFeB magnets 29

4.3. Max torque-Temperature-Electric current graphic for NdFeB magnets 29

4.4. Maximum torque depending on the magnet material at normal conditions.....30

4.5. Motor temperature distribution at normal ambient conditions 47

4.6. Shape factor graphics for two concentric cylinders 49

4.7. Motor temperature distribution at cryogenic ambient conditions.....50

6.1. Torque-Load graphic 86

6.2. Electric current-Load graphic 87

7.1. Motor temperature distribution at normal ambient conditions. Graph comparison 91

7.2. Motor temperature distribution at cryogenic ambient conditions. Graph comparison 93

APPENDIX 1 : Matlab code. Calculations

1. Torque calculation xii
2. Losses calculation xv
3. Thermal analysis xvii
4. Parameter calculation of the motor prototype xix

1. Torque calculation

1.1 NDFEB Grade 45SH properties:

(https://www.arnoldmagnetics.com/wpcontent/uploads/2017/11/N45SH-151021.pdf)

```
%At 373K (100°C)
Br1=1.23 %(Tesla)
HcB1=850e3 % (A/m3)
my0=pi*4e-7  %%Vacuum magnetic permeability
myPM1=Br1/(my0*HcB1) %% Magnet magnetic relative permeability
%At 293.15K(20°C)
Br2=1.35 %(Tesla)
HcB2=1015e3 % (A/m3)
my0=pi*4e-7  %%Vacuum magnetic permeability
myPM2=Br2/(my0*HcB2) %% Magnet magnetic relative permeability
%At 233.15 K(-40°C)
Br3=1.45 %(Tesla)
HcB3=1115e3 % (A/m3)
my0=pi*4e-7  %%Vacuum magnetic permeability
myPM3=Br3/(my0*HcB3) %% Magnet magnetic relative permeability
%At 77 K(-196.15°C)---Obtained from: Vacodym(NOT 45SH)--https://vacuumschmelze.de/Assets-
Web/Vacodym_131_en.pdf
Br4=1.58 %(Tesla)
HcB4=1230e3 % (A/m3)
my0=pi*4e-7  %%Vacuum magnetic permeability
myPM4=Br4/(my0*HcB4) %% Magnet magnetic relative permeability
```

1.2 Sm2Co17 Grade YXG32 properties:

(YXG32file:///C:/Users/MPE/Downloads/International%20Magnaproducts,%20Inc.-Grade-YXG32.pdf
http://www.smcomagnets.de/DE-Mag-SmCo.pdf)

```
%At 293.15K(20°C)
Br5=1.1
```

```
HcB5=812e3
my0=pi*4e-7  %%Vacuum magnetic permeability
myPM5=Br5/(my0*HcB5) %% Magnet magnetic relative permeability
```

1.3 Heights and sizing

```
l = 0.037; % Length of Stator in m
D = 0.0448; % Inner diamter of  Stator in m
hpm = 0.007; % height PM
rw = 0.003 ; % Radius of shaft in m
hcu = 0.0012; % height of coil
hst = 0.0026; % height of stator
si = 5e-4 % air gap = 0,5 mm (Stefan design value)
k=1.15 % Scattering factor of leakage flux (Estimation 15%)
```

1.4 Geometrical radious

```
rst = D/2 + hst;
rWI = D/2;
rsi = D/2 - hcu;
rPM = D/2 - hcu - si;
rRot = D/2 - hcu - si - hpm;

Am=(pi/10)*rPM*16*l %Cross section flux density area of magnet
Ag=(pi/10)*rPM*16*l %Cross section flux density area of air gap
WPM =(pi/10)*rPM  % Width PM
```

1.5 Winding parameters

```
Tph=192/3  %% Number of winding turns per phase
I=0.9465  %% Phase current (A)
Im=I*sqrt(2) %% Line current (A)
alpha=(pi/2) %% Load angle(Rad)
```

1.6 Magnet flux densities and torques for different ambient temperatures

```
% %% NDFEB Grade 45SH at 373K (100°C)
Bm1=(1/(1+(myPM1*(si/hpm)*(Am/Ag)*(1/k))))*(Br1+(my0*myPM1*((Tph*I)/hpm)))  % Magnet flux density
Bg1=(Bm1*Am)/(k*Ag)    % Air gap flux density
Bym1=(WPM/(2*hst))*Bg1 % Stator flux density
T1 = (3/2)*D*l*Bm1*sin(pi/10)*Tph*Im*sin(alpha)  %% Output torque

% NDFEB Grade 45SH at 293.15K(20°C)
Bm2=(1/(1+(myPM2*(si/hpm)*(Am/Ag)*(1/k))))*(Br2+(my0*myPM2*((Tph*I)/hpm)))  %% Magnet flux density
Bg2=(Bm2*Am)/(k*Ag)    % Air gap flux density
Bym2=(WPM/(2*hst))*Bg2 % Stator flux density
T2 = (3/2)*D*l*Bm2*sin(pi/10)*Tph*Im*sin(alpha)  %% Output torque

% NDFEB Grade 45SH at 233.15 K(-40°C)
Bm3=(1/(1+(myPM3*(si/hpm)*(Am/Ag)*(1/k))))*(Br3+(my0*myPM3*((Tph*I)/hpm)))  %% Magnet flux density
Bg3=(Bm3*Am)/(k*Ag)    % Air gap flux density
```

```
Bym3=(WPM/(2*hst))*Bg3 % Stator flux density
T3 = (3/2)*D*l*Bm3*sin(pi/10)*Tph*Im*sin(alpha)  %% Output torque

% NDFEB Grade 45SH at 77 K(-196.15ºC)
Bm4=(1/(1+(myPM4*(si/hpm)*(Am/Ag)*(1/k))))*(Br4+(myO*myPM4*((Tph*I)/hpm)))  %% Magnet flux density
Bg4=(Bm4*Am)/(k*Ag)     % Air gap flux density
Bym4=(WPM/(2*hst))*Bg4  % Stator flux density
T4 = (3/2)*D*l*Bm4*sin(pi/10)*Tph*Im*sin(alpha)  %% Output torque

% Sm2Co17 Grade YXG32 at 293.15K(20ºC)
Bm5=(1/(1+(myPM5*(si/hpm)*(Am/Ag)*(1/k))))*(Br5+(myO*myPM5*((Tph*I)/hpm)))  %% Magnet flux density
Bg5=(Bm5*Am)/(k*Ag)     % Air gap flux density
Bym5=(WPM/(2*hst))*Bg5  % Stator flux density
T5 = (3/2)*D*l*Bm5*sin(pi/10)*Tph*Im*sin(alpha)  %% Output torque

X1 = sprintf('Torque NDFEB at 373 K:%s/Magnet flux density:%d/Air gap flux density:%e/Stator flux
density:%f  ',T1,Bm1,Bg1,Bym1);
disp(X1)

X2 = sprintf('Torque NDFEB at 293.15 K:%s/Magnet flux density:%d/Air gap flux density:%e/Stator
flux density:%f  ',T2,Bm2,Bg2,Bym2);
disp(X2)

X3 = sprintf('Torque NDFEB at 233.15 K:%s/Magnet flux density:%d/Air gap flux density:%e/Stator
flux density:%f  ',T3,Bm3,Bg3,Bym3);
disp(X3)

X4 = sprintf('Torque NDFEB at 77 K:%s/Magnet flux density:%d/Air gap flux density:%e/Stator flux
density:%f  ',T4,Bm4,Bg4,Bym4);
disp(X4)

X5 = sprintf('Torque Sm2Co17 at 293.15K :%s/Magnet flux density:%d/Air gap flux density:%e/Stator
flux density:%f  ',T5,Bm5,Bg5,Bym5);
disp(X5)
```

Results

```
Torque NDFEB at 373 K:7.632580e-02 / Magnet flux density:1.159585e+00 / Air gap flux
density:1.008334e+00 / Stator flux density:1.261019


Torque NDFEB at 293.15 K:8.408884e-02 / Magnet flux density:1.277525e+00 / Air gap flux
density:1.110891e+00 / Stator flux density:1.389276


Torque NDFEB at 233.15 K:9.037323e-02 / Magnet flux density:1.373001e+00 / Air gap flux
density:1.193914e+00 / Stator flux density:1.493103


Torque NDFEB at 77 K:9.847745e-02 / Magnet flux density:1.496125e+00 / Air gap flux
density:1.300978e+00 / Stator flux density:1.626997
```

```
Torque Sm2Co17 at 293.15K :6.858329e-02 / Magnet flux density:1.041956e+00 / Air gap flux density:9.060487e-01 / Stator flux density:1.133100
```

Published with MATLAB® R2020a

2 Losses calculation

2.1 Heights and sizing(data)

```
l = 0.037; % Length of Stator in m
D = 0.0448; % Inner diamter of  Stator in m
hpm = 0.007; % height PM
rw = 0.003 ; % Radius of shaft in m
hcu = 0.0012; % height of coil
hst = 0.0026; % height of stator
si = 5e-4 % air gap = 0,5 mm (Stefan design value)
k=1.15 % Scattering factor of leakage flux (Estimation 15%)
```

2.2 Geometrical radious

```
rst = D/2 + hst;
rWI = D/2;
rsi = D/2 - hcu;
rPM = D/2 - hcu - si;
rRot = D/2 - hcu - si - hpm;
```

2.3 Geometrical cross section areas

```
Al = pi*(0.0005/2)^2;% Area of conductor(Round conductor, only Cu, no insulation)
Am=(pi/10)*rPM*l*16 %Cross section flux density area of magnet
Ag=2*pi*rPM*l %Cross section flux density area of air gap
```

2.4 Data material properties

```
%1-Magnets(NDFEB)At 293.15K(20°C)
bm = (pi/10)*rPM  % Width PM
VolPM = (bm*hpm)*l; % Volume PM in m^3
Br=1.35 %(Tesla)
HcB=1015e3 % (A/m3)
my0=pi*4e-7  %%Vacuum magnetic permeability
myPM=Br/(my0*HcB) %% Magnet magnetic relative permeability
rhoPM = 1.5e-6 % PM resistivity Ohm.m

%2-Stator(vacoflux)
Hc = 100 % A/m
rhoVacDensity = 8120 % kg/m3 vacoflux density
bst = 0.0005 % thickness stator(lamination) (m)
rhoVac = 0.4e-6 % Vacoflux resistivity Ohm.m
```

```
mst=0.150 %Mass stator(kg)

%3-Copper winding
rho2 = 1.72e-8;% electrical resistivity Copper at 293 K
rho1 = 0.215e-8;% rho from CRC Handbook of Chemistry p. 1988(electrical resistivity Copper at 80 K
rho11=0.0039*rho2*77; % rho electrical resistivity copper at 77 from COMSOL material property
lw = 0.1 % end winding factor
```

2.5 Flux densities

```
Bm=(1/(1+(myPM*(si/hpm)*(Am/Ag)*(1/k))))*(Br+(myO*myPM*((Tph*I)/hpm)))  % Magnet flux density
Bg=(Bm*Am)/(k*Ag) % Air gap flux density
Bst=(bm/(2*hst))*Bg % Stator flux density
```

2.6 Losses

Comment: The losses calculated here will be compared with the simulation losses so every input parameter has been taken from the inputs of the simulation (not from the motor tests).

```
% Winding losses
R1=(rho11*(l+0.01))/Al;  % One conductor resistance COMSOL model
R = (R1*192*2) % Total resistance COMSOL model
IaCOMSOL=0.37434 % Electric current COMSOL[A]
Pcu = IaCOMSOL^2*R; %Copper losses

% Stator losses
f=8 %Frequecy(Hz)
Ped = (pi^2*bst^2*Bg^2*f^2)/(6*rhoVacDensity*rhoVac); % Eddy current losses vacoflux(W/kg) -
Valentin thesis
Physt = (4*Hc*Bg*f)/rhoVacDensity; % Hysteresis losses vacoflux(W/kg) - Valentin thesis
Ptotal = Ped+Physt; % Total vacoflux losses(W/Kg)
Ptotalw=Ptotal*mst % Total vacoflux losses(W)

% Eddy current losses PM

Pm = (VolPM * bm^2 * Bg^2 * f^2)/(12*rhoPM); % Eddy current losses PM(W) - Bibliog:Calculation of
Eddy Current Losses in Permanent Magnets of Servo Motor R. Deeb


% Total motor losses in W
P=Ptotalw+Pcu+Pm


X1 = sprintf('Winding losses(Pcu):%s (W)  /   Stator losses(Ptotalw):%d (W)  /   Permanent magnet
losses(Pm):%e (W)  /   Total losses(P):%f (W)  ',Pcu,Ptotalw,Pm,P);
disp(X1)
```

Results

```
Winding losses(Pcu):6.652968e-02 (W)  /   Stator losses(Ptotalw):5.417510e-02 (W)  /   Permanent
magnet losses(Pm):2.050564e-04 (W)  /   Total losses(P):0.120910 (W)
```

Published with MATLAB® R2020a

3 Thermal analysis

3.1 Heights and sizing(data)

```
l = 0.037; % Length of Stator in m
D = 0.0448; % Inner diamter of  Stator in m
hpm = 0.007; % height PM
rw = 0.003 ; % Radius of shaft in m
hcu = 0.0012; % height of coil
hst = 0.0066; % height of stator
si = 5e-4 % air gap = 0,5 mm (Stefan design value)
k=1.15 % Scattering factor of leakage flux (Estimation 15%)
```

3.2 Geometrical radious

```
rst = D/2 + hst;
rWI = D/2;
rsi = D/2 - hcu;
rPM = D/2 - hcu - si;
rRot = D/2 - hcu - si - hpm;
```

3.3 Thermal analysis at normal conditions (convection)

```
% Thermal properties
k45=30  %Thermal conductivity vacoflux 50[W/m*k]
k34=400 %Thermal conductivity copper[W/m*k]
k12=7.6 %Thermal conductivity vacodym[W/m*k]


g=9.81      %Gravitational acceleration [m/s2]
Ts=296.7739 % Surface temperature (K). Due to the process to obtain the surface temperature is
iterative, we will first assume a temperature of 298 K, We will compute, and the result obtained
in T5 will be replaced here again, until the temperature of T5 is equal to Ts, finally this will
be the external surface temperature
Tf = 293.15 % Ambient temperature normal conditions (K)
Tv=77       % Vaccum temperature (K)

% Air properties at 20°C
k1=0.02514 %% Thermal conductivity[W/m*k]
v=1.516e-5 %% Kinematic viscosity [m2/s]
U=1.825e-5 %% Dynamic viscosity [Kg/m*s]
B=3.43e-3  %% Thermal expansion coeff [1/K]

% Convection heat transfer ambient
Pr=0.7309  %% Prandlt number
Gr =(g*B*(Ts-Tf)*D^3)/U^2 %% Grashof number
C=0.48 % Constant obtained from the product GrPr horizontal cylinder
m=0.25 % Constant obtained from the product GrPr horizontal cylinder
Nu = C*(Gr*Pr)^m  % Nusselt number
```

```
Nu1=(0.6+((0.387*(Gr*Pr)^(1/6)))/(1+(0.559/Pr)^(9/16))^(8/27))^2
h = (Nu*k1)/D  % Convection heat transfer coefficient

% Air gap heat transfer
Re=((pi*60*0.0005*rPM*2)/60)/v  %Reynolds number
Ta=(pi*60*sqrt(0.0005^3*rPM))/(30*v)
Nu2=2  %Ta<41
h2=(Nu2*k1)/0.0005 % Convection heat transfer coefficient in the air gap

%Temperature distribution
q=0.0992+0.047                              % heat losses
T5 = Tf+q*(1/((2*pi*rst*l+2*pi*rst^2)*h))   %external stator surface temperature
T4= T5+q*(log(rst/rWI)/(2*pi*l*k45))        %internal stator surface temperature=external winding
surface temperature
T3= T4-q*(log(rWI/rsi)/(2*pi*l*k34))        %internal winding surface temperature
T3f= T3-q*(1/((2*pi*rsi*l+2*pi*rsi^2)*h2))  %external airgap surface temperature
T2f=T3f-q*(log(rsi/rPM)/(2*pi*l*k1))        %internal airgap surface temperature
T2= T2f-q*(1/((2*pi*rPM*l+2*pi*rPM^2)*h2))  %external magnets surface temperature
T1=T2-q*(log(rPM/rRot)/(2*pi*l*k12))        %internal magnets surface temperature=rotor shaft
temperature
```

3.4 Thermal analysis at cryogenic conditions (radiation)

```
%Thermal constants
b=5.6697e-8          %Stefan Boltzmann constant(W/m2.K4)
e1=0.9               % Stator emissivity
e2=0.1               % winding emissivity
e3=0.9               % Magnet emissivity
e4=0.9               % rotor shaft emissivity
emix = 0.7           % emissivity used in the calculation as a mix of the emissivity components
for the radiation to the exterior calculation

%Areas
Alwk = (pi/4)*rWI*0.01*2 % Total end winding area (above and below)
Aax=pi*rst^2*2  % Axial surfaces area
Ast=2*pi*rst*l  % Lateral stator area
Atotal= Alwk+Aax+Ast  % Total radiaton area

%Temperature distribution
T5rad=((q/(b*emix*Atotal)+Tv^4))^(1/4)  %external stator surface
T4rad= T5rad+q*(log(rst/rWI)/(2*pi*l*k45))%internal stator surface temperature=external winding
surface temperature
T3rad= T4rad-q*(log(rWI/rsi)/(2*pi*l*k34))%internal winding surface temperature
T2rad=(T3rad^4-((q/b)*((1-0.9)/(2*pi*rPM*l*0.9)+1/(2*pi*rPM*l)+(1-0.1)/(2*pi*rsi*l*0.1))))^(1/4)
%external magnets surface temperature
T1rad=T2rad-q*(log(rPM/rRot)/(2*pi*l*k12))%internal magnets surface temperature=rotor shaft
temperature


X1 = sprintf('T5 (K):%s / T4 (K):%d / T3 (K):%e / T3f (K):%f / T2f (K):%g / T2 (K):%h / T1 (K):%i
',T5,T4,T3,T3f,T2f,T2,T1);
disp(X1)
```

```
X2 = sprintf('T5rad (K):%s / T4rad (K):%d / T3rad (K):%e / T2rad (K):%h / T1rad (K):%i
',T5rad,T4rad,T3rad,T2rad,T1rad);
disp(X2)
```

Results

```
h (convection coefficient):3.3547
T5 (K):2.967739e+02 / T4 (K):2.967793e+02 / T3 (K):2.967792e+02 / T3f (K):296.591645 / T2f
(K):295.995 / T2 (K):295.8009 / T1 (K):295.7667


T5rad (K):1.350619e+02 / T4rad (K):1.350673e+02 / T3rad (K):1.350672e+02 / T2rad (K): 1.8776e+02 +
1.8776e+02i / T1rad (K): 1.8773e+02 + 1.8776e+02i
```

Published with MATLAB® R2020a

4. Parameter calculation of the motor prototype

Comment: The following code shows the calculation of the prototype motor parameters. The objective of this code was to analytically represent the behaviour of the real motor, by representing its electrical circuit and finally calculating the electromagnetic torque. However due to some problems in the test measurement result of the electrical current explained in the inconsistent values section, the electrical parameters obtained analytically here cannot be compared, and so verified with the measurements. And this is a problem because the electrical current, which is also related with other electrical parameters may be wrong, or even the complete electrical circuit presented may be wrong.
In other words, in order to obtain the result of the torque analytically to compare it with the measurement results, which was the primary objective of this code, it is also necessary to calculate a multitude of electrical parameters of the motor, the electrical current is between of them and some others such as electrical resistance or inductance, therefore a single failure of one of these parameters would cause a final wrong torque result. Thus, given the complexity that this code represented, it was preferred to look for an alternative for the calculation of the electromagnetic torque. This alternative was presented in the previous 1. Torque Calculation code, where the electric current is considered as an input parameter, in this way the odds of error decrease. Even so, this code is also presented in this thesis, and its development, optimization and improvement is recommended for future studies.

```
% Heights and sizing
l = 0.037; % Length of Stator in m
D = 0.0448; % Inner diamter of  Stator in m
hpm = 0.007; % height PM
rw = 0.003 ; % Radius of shaft in m
hcu = 0.0012; % height of coil
hst = 0.0026; % height of stator
```

```
si = 5e-4 % air gap = 0,5 mm (Stefan thesis design value)

% Geometrical radious

rst = D/2 + hst;
rWI = D/2;
rsi = D/2 - hcu;
rPM = D/2 - hcu - si;
rRot = D/2 - hcu - si - hpm;

% Values from data sheet Vacodym 131 DTP

Br = 1.58; % T
HcB = -1230000; % A/m
my0 = 1.256637e-6;

% Helping parameters

p = 8; % pole pair number
W =8; % Chording ratio W/t
t = 12;
m = 3;  % No of phases
z1 = 4; % zone number 1
z2 = 4; % zone number 2
q = (z1+z2)/2; % N° slots per pole and strand
tp = D * pi / (2 * p);  %pole pitch
Us = pi * D; % circumference of stator inner side

% rho from CRC Handbook of Chemistry p. 1988(electrical resistivity Copper
% at 80 K
rho1 = 0.215e-8;
% electrical resistivity Copper at 293 K
rho2 = 1.7e-8;

% Input electrical parameters

Uphase = 4.5;  % supply phase voltage V
Ulineline=sqrt(3)*Uphase; % line voltage V
f = 8;  % frequency Hz
p = 8; % pole pair number
phin = 0.5; % slot fill factor (estimation)
phiFe = 0.8; % iron fill factor (estimation)
Bvac = 2,35; % Saturation flux Data sheet Vacoflux 50
alphae = 0.8; % pole coverage factor
cosphi = 0.98; % estimation power factor

% kt measurement
fe=23.57;                   % elecrical frequency
Upkpk = 2.1921;             % peak to peak voltage mesurement in volts
we=2*pi*fe;                 % electrical speed
kt = Upkpk/(2*we);          %  Back EMF constant = torque constant

% Current calculation
```

```
lwk = 0.5;  % Ratio of winding head to conductor length (estimation)
N = 192*2;  % N°slots * 2 layers
Al = pi*(0.0005/2)^2;% Area of conductor(Round conductor, only Cu, no insulation)
lw = 2; % lenght of the end wires getting into the phase boxes, Unit (m)

R1=(rho2*l)/Al;  % One conductor resistance COMSOL model
R = (R1*192*2) % Total resistance COMSOL model
IaCOMSOL=0.591 % Electric current COMSOL[A]
Pcu = IaCOMSOL^2*R; %Copper losses
Lh = 0.00004;  % Phase measured inductance[Henries]
Rm=4;  % Phase measured resistance [Ohms]

% Circuit equation parameters

% The parameters will be calculated considering a maximum electrical load angle (90°) for a
% specific supply voltage of 3.2 V and a frequency of 6.27 Hz.

Ws = ((120*f)/(2*p))*((2*pi)/60);  % synchronous speed rad/s
Wsrpm = (120*f)/(2*p)  % synchronous speed rpm
Delta = pi/6;               %Electrical load angle
Deltam = Delta/p;        %Mechanical load angle
Ea = kt*2*pi*f; %Back EMF
Xs = 2*pi*f*Lh;           %reactance
Zs = complex(R,Xs);       %impedance

Er=complex(Uphase-Ea*cos(Delta),Ea*sin(Delta));
Ia=Er/Rm; % Armature current
IaM=abs(Ia); % Armature current module
Phi=angle(Ia); % Phase angle current-voltage
S = IaM / Al; % Current density

% Magnetic circle calculation
mypm = -Br/HcB % Permeability PM (Estimation based on NdFeB)
sf = 1.15 % Scattering factor of leakage flux (Estimation 15%)
% nut height = 2 * sqrt(conductor area) due to round conductor
% and two-layer winding

Bsi = Br / ((sf / alphae) + (mypm * (si + hcu) / (my0 * hpm))) % Air gap magnetic flux

% losses in the stator
Hc = 100 % A/m
rhoVacDensity = 8120 % kg/m3 vacoflux density
bst = 0.0005 % thickness stator(lamination)
rhoVac = 0.4e-6 % Vacoflux resistivity Ohm.m
Bst = Bsi % considering the magnetic flux density in the air gap equal to the one of the stator
Pst = (pi^2*bst^2*Bst^2*f^2)/(6*rhoVacDensity*rhoVac); % Eddy current losses vacoflux(W/kg) -
Valentin thesis
Physt = (4*Hc*Bst*f)/rhoVacDensity; % Hysteresis losses vacoflux(W/kg) - Valentin thesis
Ptotal = Pst+Physt; % Total vacoflux losses
% Eddy current losses PM
VolPM = ((pi*(rPM^2 - rRot^2))/18)*l; % Volume PM in m^3
bm = (pi/10)*(rRot+((rPM^2 - rRot^2)/2)); % magnet width
rhoPM = 1.5e-6 % PM resistivity Ohm.m
Pm = (VolPM * bm^2 * Bsi^2 * f^2)/(12*rhoPM); % Eddy current losses PM(W) - Bibliog:Calculation of
```

```
Eddy Current Losses in Permanent Magnets of Servo Motor R. Deeb

% Power and torque

P1 = 3*((Uphase^2-Uphase*Ea*cos(Delta))/Zs); % Output mechanical power
Torque = P1/Ws; % Induced electrical power 1°method (W)
P2 = Uphase*IaM*cos(Phi) % Input electrical power
Pmech = P1-Pm-Ptotal; %I Mechanical power (W)
Eff = Pmech/P1; % Power efficiency
Torque = P1/Ws % Output torque induced (N.m)
```

Published with MATLAB® R2020a